ORNL/TM-12781

Chemical Technology Division

FLUID DYNAMIC STUDIES FOR A SIMULATED MELTON VALLEY STORAGE TANK SLURRY

T. D. Hylton
E. L. Youngblood
R. L. Cummins

Date of Issue: July 1994

Prepared for the
Waste Management and Remedial Action Division
(EW 31 20 04 5)

Prepared by the
OAK RIDGE NATIONAL LABORATORY
Oak Ridge, Tennessee 37831-6285
managed by
MARTIN MARIETTA ENERGY SYSTEMS, INC.
for the
U.S. DEPARTMENT OF ENERGY
under contract DE-AC05-84OR21400

DISCLAIMER

DISCLAIMER

Portions of this document may be illegible in electronic image products. Images are produced from the best available original document.

CONTENTS

FIGURES

TABLES

SYMBOLS AND ABBREVIATIONS

Symbols

D	Diameter of pipe or tube
f	Fanning friction factor
g	Acceleration of gravity
g_c	Newton's-law proportionality factor
h_f	Friction loss between points a and b
h_{fs}	Friction loss (skin) between points a and b
K	Consistency factor (Power Law model parameter)
K'	Flow consistency index
L	Length of pipe or tube
n	Flow behavior index (Power Law model parameter)
N_{He}	Hedström number
N_{Re}	Reynolds number (Newtonian)
$N_{Re,BP}$	Reynolds number (Bingham plastic)
$N_{Re,Gen}$	Reynolds number (Generalized)
$N_{Re,PL}$	Reynolds number (Power Law)
P_a	Pressure at point a
P_b	Pressure at point b
ΔP_f	Pressure drop (due to friction) across length (L) of pipe = $P_a - P_b$
ΔP_{fs}	Pressure drop (due to skin friction) across length (L) of pipe
Q	Volumetric flow rate
r_w	Radius of pipe (at the wall)

$\dot{S}$	Shear rate
$\dot{S}_w$	Shear rate at the pipe wall
u	Linear velocity
$\bar{V}_a$	Average velocity at a = volumetric flow rate/cross-sectional area at point a
$\bar{V}_b$	Average velocity at b = volumetric flow rate/cross-sectional area at point b
V_s	Wall slip velocity
W_p	Pump work per unit mass of fluid
x	Ratio of yield stress to shear stress at the wall = τ_y/τ_w
x_c	Critical value of the τ_y/τ_w ratio
Z_a	Height above datum plane at point a
Z_b	Height above datum plane at point b
α	Kinetic energy correction factor
η	Plastic viscosity (Bingham plastic model parameter)
η_p	Overall efficiency of pump
μ	Newtonian viscosity
ρ	Fluid density
τ	Shear stress
τ_w	Shear stress at the pipe wall
τ_y	Yield stress (Bingham plastic model parameter)

Units of measure

atm	atmosphere
°C	degrees Celsius
cm	centimeter
cP	centipoise
dyn	dyne
ft	foot
g	gram
h	hour
in.	inch
kPa	kilopascal
L	liter
m	meter
μm	micrometer
min	minute
mL	milliliter
mm	millimeter
mPa	millipascal
Pa	pascal
s	second
wt %	weight percent

Acronyms

MVSTs	Melton Valley Storage Tanks
ORNL	Oak Ridge National Laboratory
RCRA	Resource Conservation and Recovery Act
WIPP	Waste Isolation Pilot Plant
YPLPIPE	Yield Power Law Pipeline Design Program

Chemical formulas

$Al(NO_3)_3$	Aluminum nitrate
$Al(OH)_3$	Aluminum hydroxide
$Ca(NO_3)_2$	Calcium nitrate
$Ca(OH)_2$	Calcium hydroxide
$Fe(NO_3)_3$	Iron(III) nitrate
$Fe(OH)_3$	Iron(III) hydroxide
NaOH	Sodium hydroxide

PREFACE

The International System of Units (SI) was the standard of measurement units for this report. However, English units were maintained for standard pieces of equipment and materials. For example, English units are used to describe the piping used to construct the pipeline viscometers. Standard piping is typically designated with English units (e.g., 1-in. Schedule 40 stainless steel pipe).

FLUID DYNAMIC STUDIES FOR A SIMULATED MELTON VALLEY STORAGE TANK SLURRY

T. D. Hylton, E. L. Youngblood, R. L. Cummins

ABSTRACT

The Melton Valley Storage Tanks (MVSTs), which are located at the Oak Ridge National Laboratory, are used for the collection and storage of remote-handled radioactive liquid wastes. These wastes, which were typically acidic when generated, were neutralized with the addition of sodium hydroxide to protect the storage tanks from corrosion, but this caused the transuranic and heavy metals to precipitate. These wastes will eventually need to be removed from the tanks for ultimate disposal. The objective of the research activities discussed in this report is to support the design of a pipeline transport system between the MVSTs and a treatment facility. Since the wastes in the MVSTs are highly radioactive, a surrogate slurry was developed for this study. Rheological properties of the simulated slurry were determined in a test loop in which the slurry was circulated through three pipeline viscometers of different diameters. Pressure drop data at varying flow rates were used to obtain shear stress and shear rate data.

Twelve runs were made with the test loop using MVST surrogates that contained suspended solids concentrations ranging from ≈23 to 34 wt %. The experiments were divided into four categories. The first three categories explored two variables: (1) concentration of dissolved and suspended solids and (2) temperature of the slurry. The objective of the fourth category was to determine the minimum transport velocity for the slurry.

The runs were successfully completed with few difficulties. The data were analyzed, and the slurry rheological properties were analyzed by the Power Law model and the Bingham plastic model. The surrogate slurry developed for this study worked well. The plastic viscosity and yield stress data obtained from the rheological tests were used as inputs for a piping design software package, and the pressure drops predicted by the software compared well with the pressure drop data obtained from the test loop.

The minimum transport velocity was determined for the slurry by adding known nominal sizes of glass spheres to the slurry. The density of the glass spheres was similar to the density of the suspended solids, but the size of the glass spheres was selected to be conservatively large to predict the minimum transport velocity. However, it was shown that the surrogate slurry exhibited hindered settling, which may substantially decrease the minimum transport velocity. Therefore, it may be desired to perform additional tests with a surrogate that does not undergo hindered settling (i.e., a surrogate with a lower concentration of suspended solids) to determine the minimum transport velocity.

1. INTRODUCTION

The Melton Valley Storage Tanks (MVSTs), which are located at the Oak Ridge National Laboratory (ORNL), are used for the collection and storage of remote-handled radioactive liquid wastes. The wastes in the MVSTs were generated from a variety of facilities including reactors, radioactive fuel and target processing areas, radioisotope processing areas, decontamination operations, hot cells, and radiochemical laboratories. These wastes, which were typically acidic when generated, were neutralized with the addition of sodium hydroxide to protect the storage tanks from corrosion, but this action caused the transuranic and heavy metals to precipitate [Sears, 1990]. The precipitate settled and formed a layer of sludge ≈0.6 to 1.2 m (≈2 to 4 ft) deep in the bottom of the MVSTs; therefore, the wastes consist of two phases.

The long-range plan is to remove the wastes from the MVSTs and process them for ultimate disposal at the Waste Isolation Pilot Plant (WIPP) in Carlsbad, New Mexico. A treatment facility is proposed for construction at ORNL to process the wastes by evaporation to a dry salt cake for disposal at the WIPP. To expedite the removal of the two-phase waste material from the MVSTs, the solid and liquid phases will be mixed to create a slurry; the slurry will then be pumped to the treatment facility.

The objective of this study was to study the rheology of a slurry similar to that which will be generated in the MVSTs for contributions to the design of the slurry transportation system from the MVSTs to the treatment facility. Since the wastes in the MVSTs are highly radioactive, a surrogate slurry was developed for this study.

Mathematical models have been developed for non-Newtonian fluids to describe their rheological behavior. These models can be used to specify the parameters for designing a slurry

transport system. The model can be used for predicting the expected pressure drop for the transfer system so that a pump and the pipeline can be appropriately specified. For example, the pipeline should be sized to minimize the pressure drop so that the pump size (and usually the cost) may be minimized. For a given fluid and flow rate, the pressure drop that exists because of friction decreases as the pipe diameter increases. One may, therefore, be tempted to specify a large pipe diameter to minimize the pressure drop. However, one must also consider the cost of the larger-size piping, and in the case of pumping a slurry, one must consider the velocity at which the slurry will be pumped. In general, a high velocity (turbulent flow) will help keep the solid particles suspended during transport of the slurry. For a given fluid and flow rate, the velocity will be higher through a small-diameter pipe than through a large-diameter pipe. Therefore, the criteria of pressure drop, velocity, and cost must all be considered for a properly designed transport system.

2. RHEOLOGICAL MODELS AND DATA ANALYSIS

2.1 RHEOLOGICAL MODELS

The science of determining the functional dependence of stress versus strain rate for fluid and semifluid materials is known as rheology. Fluid behavior is categorized as Newtonian or non-Newtonian. Newtonian fluids are identified by the independent relationship between viscosity and shear rate, whereas the viscosity of non-Newtonian fluids is dependent on the shear rate applied to the fluid. Consequently, it is important to know whether a fluid or slurry behaves as a Newtonian or non-Newtonian fluid.

Slurries typically behave as non-Newtonian fluids. The most prevalent non-Newtonian models for representing fluid dynamic behavior for slurries are the (1) Bingham plastic, (2) Power Law, and (3) Yield Power Law. These models and the Newtonian model are compared with regard to the functional dependence of shear stress to shear rate in Figure 1. The rheological behavior of many slurries is usually described by one of these models. The Newtonian model and these three non-Newtonian models are discussed in more detail below.

2.1.1 Newtonian

As shown in Figure 1, the Newtonian model is a straight line that intercepts the shear stress axis at the origin. The slope of this line is known as the viscosity of the fluid. Water and sucrose solutions are typical Newtonian fluids. The behavior of a Newtonian fluid is represented as shown in the following equation:

where τ = shear stress,
μ = viscosity,
$\dot{S}$ = shear rate.

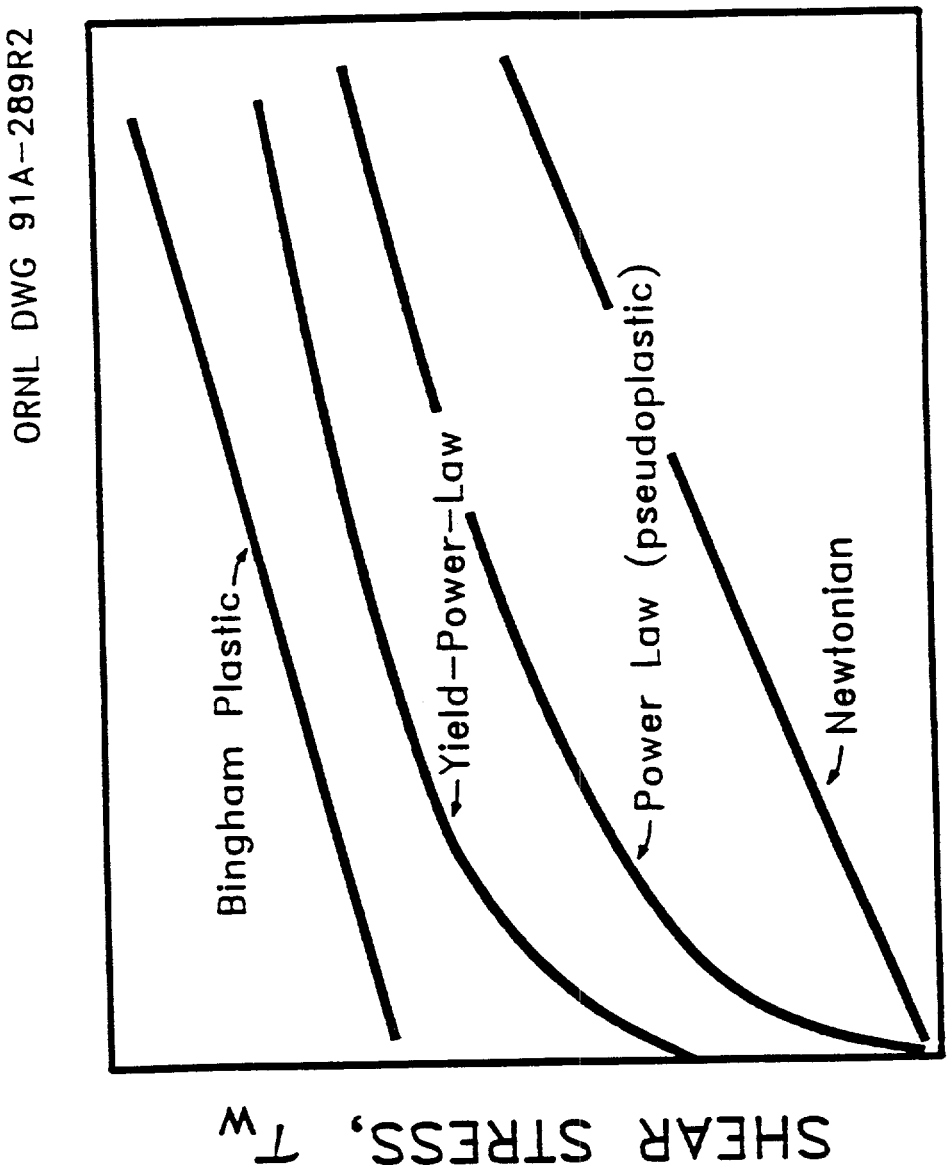

Figure 1. Typical shear stress – shear rate curves for Newtonian and non-Newtonian fluids

2.1.2 Bingham Plastic

The Bingham plastic model is also represented by a straight line as shown in Figure 1. Although it appears similar to the Newtonian model, the line crosses the shear stress axis above the shear stress origin. The point where the line crosses the shear stress axis is designated as the yield stress. The yield stress is generally defined as the amount of stress required just to start fluid movement. However, the yield stress corresponds in the mathematical formulation to a minimum threshold in which the material behaves as a solid below the threshold and a liquid above the threshold [Hanks, 1986, p. 225]. The slope of the Bingham plastic model is known as the plastic viscosity. Plastic viscosity differs from the Newtonian viscosity because a correction factor has been applied to determine the shear rate. The mathematical model for the Bingham plastic is

$$\tau = \eta \dot{S} + \tau_y , \tag{2}$$

where η = plastic viscosity,
τ_y = yield stress.

2.1.3 Power Law Model

The Power Law model is an alternate method for modeling fluid flow behavior for pseudoplastic and dilatant materials. It provides a nonlinear mathematical relationship between the shear stress and the shear rate. This model is defined as follows:

$$\tau = K\dot{S}^n , \tag{3}$$

where K = consistency factor,
n = flow behavior index.

If $n < 1$, the apparent viscosity decreases with increasing shear rate, and these fluids are referred to as pseudoplastic fluids. Conversely, if $n > 1$, the apparent viscosity increases with the shear

rate, and these fluids are known as dilatants. In the special case that n = 1, then K is equivalent to the Newtonian viscosity [Dodge and Metzner, 1959]. The Power Law is favored because of its mathematical simplicity; however, it can be safely used only for interpolation between existing measured values of shear rate, not for extrapolation to higher values.

2.1.4 Yield Power Law Model

The Yield Power Law model combines the yield stress from the Bingham plastic model with the Power Law model to describe the fluid behavior (see Figure 1). This model is represented by equation 4:

$$\tau = \tau_y + K\dot{S}^n . \qquad (4)$$

The Yield Power Law model is mathematically more difficult to use than the Bingham plastic or Power Law models. Since the Yield Power Law model is a combination and refinement of the Bingham plastic and Power Law models, a decision was made to not investigate the Yield Power Law model further unless the Bingham plastic and Power Law models were inadequate to represent the rheology of the slurries.

2.2 DATA ANALYSIS

The rheology of a fluid or slurry is typically determined by instruments known as viscometers. Many types of viscometers are available (e.g., Couette, Cone-Plate), but these instruments are typically capable of measuring the viscosity only at low shear rates, or the instrument is not useful for slurries because of tiny clearances which will not admit solid particles well. Theoretically, a pipeline viscometer can be used to measure the viscosity at any shear rate provided that the flow remains laminar. Any device used to measure the viscosity of a fluid must be instrumented to measure parameters that can be related functionally to the

shear stress and the shear rate. In the case of a pipeline viscometer, the measured variables are pressure drop across a known length of pipe with a known diameter and flow rate. The raw data obtained from this device must be converted into shear stress and shear rate data before the rheological behavior of the fluid can be determined. For a Newtonian fluid, the shear rate is easily determined. For a non-Newtonian fluid, the determination is not straightforward, and the Rabinowitsch-Mooney equation provides the method for this determining the shear rate as described in Section 2.2.2.

2.2.1 Shear Stress

Figure 2 shows a cylindrical slug of slurry in a pipe. A force balance performed on the slug of fluid in the direction of the flow velocity yields the following equation:

$$\tau_w \pi DL = \Delta P_f \frac{\pi D^2}{4}, \tag{5}$$

where τ_w = shear stress at the wall,
D = pipe or tube diameter,
L = length,
ΔP_f = pressure differential due to friction across the slug ($P_b - P_a$).

Equation 5 can be rearranged to more conveniently determine the shear stress at the wall, as shown in equation 6:

$$\tau_w = \frac{D\Delta P_f}{4L}. \tag{6}$$

2.2.2 Shear Rate

The shear rate for a Newtonian fluid is independent of the shear stress, and the shear rate is equivalent to $8\bar{V}/D$, where $\bar{V}$ = average velocity. The shear stress of a non-Newtonian fluid is dependent on the shear stress, and a correction factor must be applied.

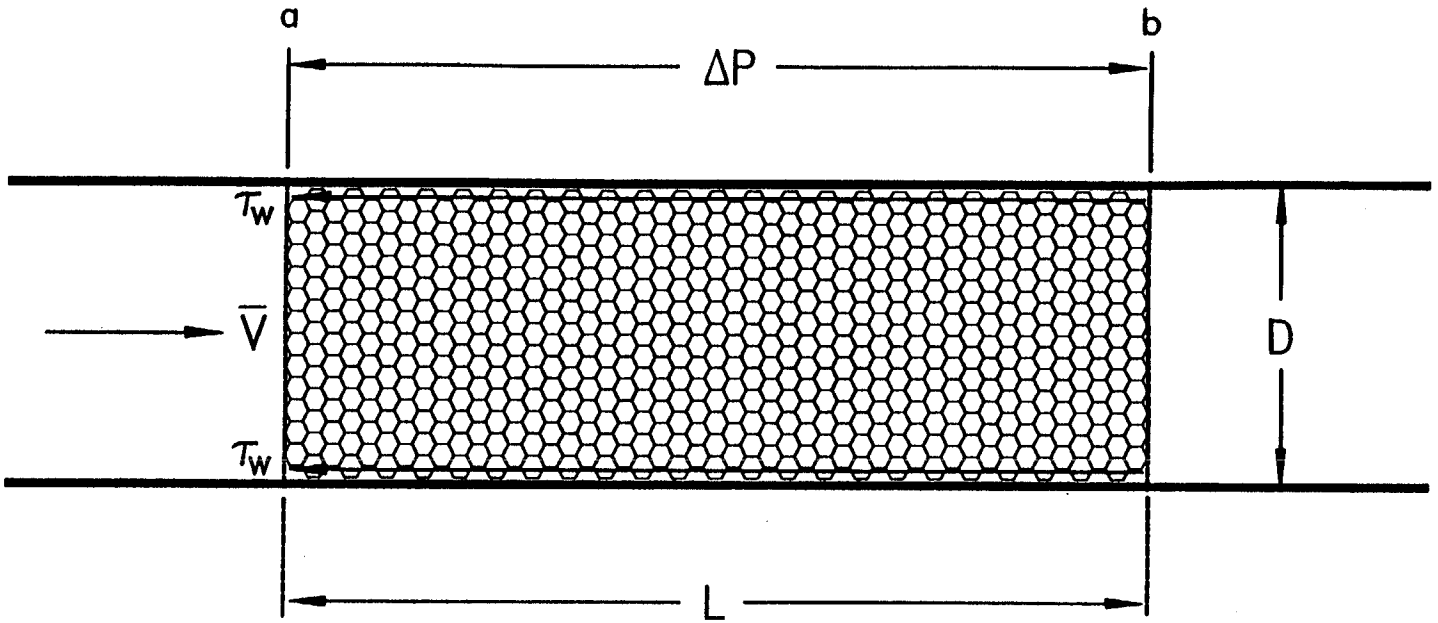

Figure 2. Force balance on a cylindrical slug of fluid.

Adapted with permission from N. I. Heywood, "Rheological Characterisation of Non-settling Slurries," Chapter 4 in N. P. Brown and N. I. Heywood (eds.), *Slurry Handling Design of Solid-Liquid Systems*. Elsevier Science Publishers, Essex, England, 1991.

The Rabinowitsch-Mooney equation is used to determine the shear rate at the wall when the fluid is non-Newtonian, the flow is steady, the fluid is time-independent, the flow is laminar, and there is no slip at the wall. As shown by Metzner and Reed [1955], the Rabinowitsch-Mooney equation can be represented as

$$3\left(\frac{8Q}{\pi D^3}\right) + \frac{D\Delta P_f}{4L}\frac{d(8Q/\pi D^3)}{d(D\Delta P_f/4L)} = \left(-\frac{du}{dr}\right)_w = \dot{S}_w \,, \tag{7}$$

where Q = volumetric flow rate,
u = linear velocity,
$\dot{S}_w$ = shear rate at the wall.

Equation 7 may be rearranged into the form shown in equation 8:

$$\dot{S}_w = \left(\frac{8\overline{V}}{D}\right)\left(\frac{3n' + 1}{4n'}\right) , \tag{8}$$

where n' is defined by

$$n' = \frac{d\ \ln(D\Delta P/4L)}{d\ \ln(8\overline{V}/D)} . \tag{9}$$

When the viscosity is independent of the shear rate (i.e., when the fluid is Newtonian), the value of n' is equal to one. Therefore, it can be easily seen that equation 8 reduces to $\dot{S}_w = 8\overline{V}/D$ for Newtonian fluids, which agrees with the earlier statement about shear rate for Newtonian fluids. For non-Newtonian fluids, the value of n' will vary with position on plots of $\ln(D\Delta P/4L)$ versus $\ln(8V/D)$, unless the fluid can be modeled as a Power Law fluid. Therefore, the shear rate must be determined at each corresponding data point.

Figure 3 demonstrates the method for determining the value of n'. In general, the value of n' should be determined at each value of $8\overline{V}/D$. However, if the fluid can be represented by the Power Law model, the curve appears as a straight line and the value of n' is constant and

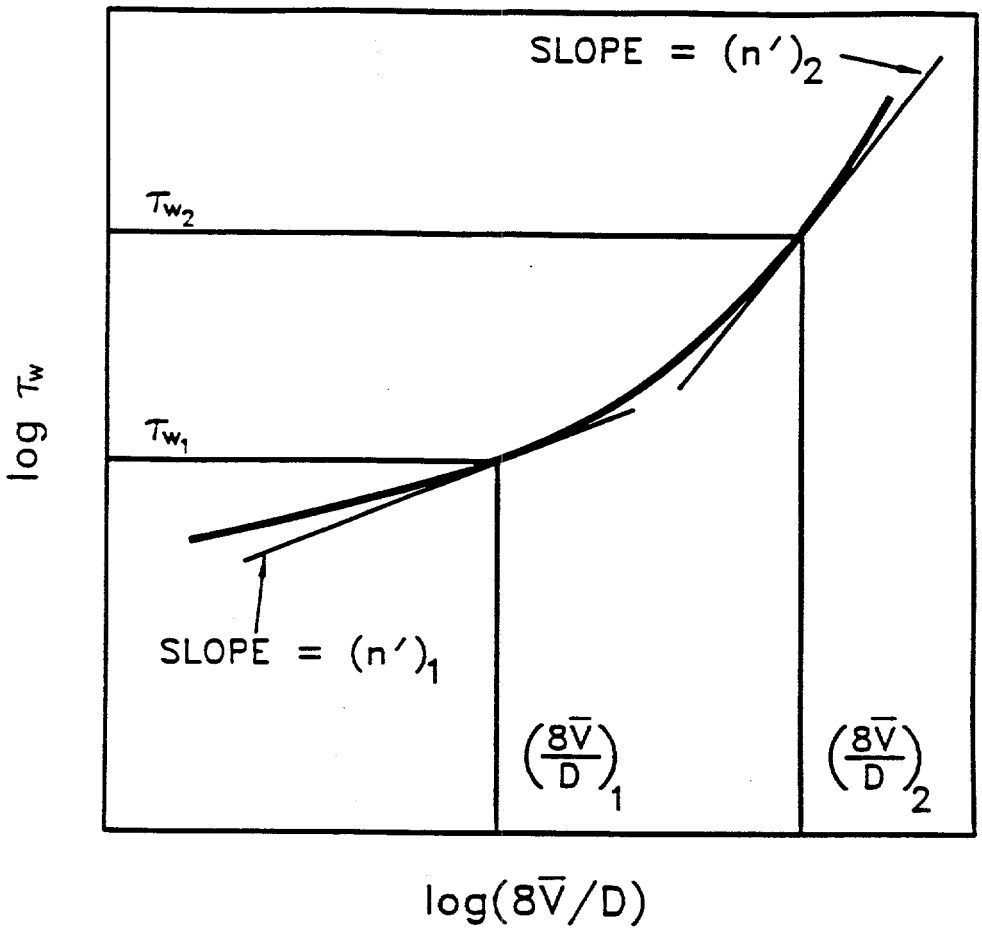

Figure 3. Method for determining values of n′.

Adapted with permission from N. I. Heywood, "Rheological Characterisation of Non-settling Slurries," Chapter 4 in N. P. Brown and N. I. Heywood (eds.), *Slurry Handling Design of Solid-Liquid Systems*. Elsevier Science Publishers, Essex, England, 1991.

is equivalent to the Power Law index, n. The intercept point on the y-axis when ln(8V/D) = 1 determines the value of K', the consistency index.

2.2.3 Friction

Bernoulli's mechanical energy balance, which can be used for problems dealing with the flow of incompressible fluids, is shown below [McCabe and Smith, 1976]:

$$\frac{P_a}{\rho} + \frac{g Z_a}{g_c} + \frac{\alpha_a \nabla_a^2}{2 g_c} + \eta_p W_p = \frac{P_b}{\rho} + \frac{g Z_b}{g_c} + \frac{\alpha_b \nabla_b^2}{2 g_c} + h_f , \qquad \textbf{(10)}$$

where P_a = pressure at point a,
P_b = pressure at point b,
V_a = average velocity at a = volumetric flow rate/cross-sectional area at point a,
V_b = average velocity at b = volumetric flow rate/cross-sectional area at point b,
Z_a = height above datum plane at point a,
Z_b = height above datum plane at point b,
g = acceleration of gravity,
g_c = Newton's-law proportionality factor,
h_f = friction loss between points a and b,
W_p = pump work per unit mass of fluid,
α = kinetic energy correction factor,
ρ = fluid density,
η_p = overall efficiency of pump.

Equation 10 can be modified to neglect the terms that have little or no effect on the system. Using Figure 2 as a reference for a pipeline, one can assume that $\bar{V}_a$ and $\bar{V}_b$ are equivalent if the flow rate and diameter are constant. One can also eliminate the height above datum plane factors since the pipe is horizontal (i.e., $Z_a = Z_b$). The pump work term may also be eliminated since there is not a pump between points a and b. The friction loss can then be expressed by equation 11 with these assumptions:

$$h_f = \frac{(P_a - P_b)}{\rho} = \frac{\Delta P}{\rho} . \qquad \textbf{(11)}$$

For the case where there is a difference in the heights above the datum plane (e.g., a vertical pipe), the friction loss due to friction between points a and b may be determined from equation 12 (with all other assumptions for equation 11 still intact):

$$h_f = \frac{(P_a - P_b)}{\rho} + \frac{g}{g_c}(Z_a - Z_b) \; . \qquad \textbf{(12)}$$

The friction measured with pipeline viscometers is due to skin friction between the wall and the fluid stream; therefore, a subscript s is added to the h_f and ΔP terms to differentiate from other types of friction loss. Four quantities are commonly used to determine the friction loss in pipes: (1) skin friction, (2) pressure drop, (3) shear stress at the wall, and (4) Fanning friction factor. These terms are related as shown by the following equation [McCabe and Smith, 1976, p. 86]:

$$h_{fs} = \frac{4\tau_w L}{\rho D} = \frac{\Delta P_s}{\rho} = 2f\frac{L\nabla^2}{Dg_c} \; , \qquad \textbf{(13)}$$

where h_{fs} = friction loss (skin),
ΔP_s = pressure drop due to skin friction,
f = Fanning friction factor.

Equation 14 can be obtained by rearrangement of equation 13 to determine the Fanning friction factor:

$$f = \frac{\Delta P_s g_c D}{2L\rho\nabla^2} \; . \qquad \textbf{(14)}$$

Equations 13 and 14 are valid for both laminar and turbulent flow if the fluid is incompressible and the flow is steady and fully developed [McCabe and Smith, 1976, p. 87]. The determination of whether a flow is laminar or turbulent is determined from the Reynolds number. The transition point between laminar and turbulent flow is known as the critical

Reynolds number. The Reynolds number for non-Newtonian fluids may differ from that for Newtonian fluids because the viscosity is dependent on the shear rate for non-Newtonian fluids.

2.2.3.1 Newtonian fluids

For Newtonian fluids, the Reynolds number is defined as

$$N_{Re} = \frac{\rho \nabla D}{\mu} , \tag{15}$$

where N_{Re} = Newtonian Reynolds number.

The friction factor for laminar flow of a Newtonian fluid, which has been shown to be derived from the Hagen-Poiseuille equation [McCabe and Smith, 1976, p. 89], is shown in equation 16:

$$f = \frac{16\mu}{D\nabla\rho} = \frac{16}{N_{Re}} . \tag{16}$$

2.2.3.2 Power Law fluids

Ostwald-de Waele [McCabe and Smith, p. 90] found that the pressure difference for the laminar flow of a Power Law fluid may be expressed as

$$\Delta P_s = \frac{2K'}{g_c} \left[\frac{3n' + 1}{n'}\right]^{n'} \frac{\nabla^{n'}}{r_w^{n'+1}} L , \tag{17}$$

where K' = flow consistency index,
r_w = radius of pipe.

The value of K' may be determined from the intercept of the straight line drawn tangent to the curve of $\ln \tau_w$ versus $\ln(8V/D)$. The relationship between K' in equation 17 and K in equation 3 is shown in equation 18. Basically, the difference between K and K' is the

correction for the shear rate. One should recall that n′ = n for a Power Law fluid [Dodge and Metzner, 1959]:

$$K' = K\left[\frac{3n + 1}{4n}\right]^n . \tag{18}$$

The following equation for the Fanning friction factor can be determined for laminar flow by substituting equation 17 into equation 14:

$$f = \frac{2^{n'+1}K'}{D^{n'}\rho\nabla^{2-n'}}\left[3 + \frac{1}{n'}\right]^{n'} . \tag{19}$$

A Reynolds number for Power Law fluids can be defined as follows:

$$N_{Re,PL} = 2^{3-n'}\left(\frac{n'}{3n' + 1}\right)\frac{D^{n'}\rho\nabla^{2-n'}}{K'} , \tag{20}$$

where $N_{Re,PL}$ = Reynolds number for Power Law fluids.

Equation 20 is based on the assumption that the Fanning friction factor can be defined for Power Law fluids as shown in equation 21:

$$f = \frac{16}{N_{Re,PL}} . \tag{21}$$

Metzner and Reed developed a generalized method of expressing the Reynolds number that would allow an equation similar to equation 21 to be applied to all fluids. The generalized Reynolds number expression developed by Metzner and Reed [1955] is shown as

$$N_{Re,Gen} = \frac{D^{n'}\nabla^{2-n'}\rho}{8^{n'-1}K'} , \tag{22}$$

where $N_{Re,Gen}$ = generalized Reynolds number.

The Reynolds number for Power Law fluids is generally defined such that laminar flow exists at $N_{Re,Gen} < 2100$. The Fanning friction factor is then defined as follows:

$$f = \frac{16}{N_{Re,Gen}} . \quad (23)$$

It should be emphasized that the previous equations for the friction factor for the Power Law apply only to the laminar region. Metzner and Reed [1955] proposed an empirical formula for modeling the friction factor in the turbulent region. This model is shown in equation 24:

$$f = 0.00140 + \frac{0.125}{(N_{Re,Gen})^{0.32}} . \quad (24)$$

2.2.3.3 Bingham plastic fluids

The Bingham plastic model redefines the Reynolds number by substituting the plastic viscosity (η) for the viscosity in the Newtonian Reynolds number formula. The formula for calculating the Bingham plastic Reynolds number is shown below:

$$N_{Re,BP} = \frac{\rho \nabla D}{\eta} . \quad (25)$$

The Bingham plastic model defines the friction factor as a function of the Reynolds number and the Hedström number. The Hedström number is defined as follows:

$$N_{He} = \frac{D^2 \tau_y \rho}{\eta^2} . \quad (26)$$

Buckingham published the following relation in 1921 for the friction factor in the laminar flow region [Heywood, 1991, p.134]:

$$\frac{1}{N_{Re,BP}} = \frac{f}{16} - \frac{N_{He}}{6(N_{Re,BP})^2} + \frac{(N_{He})^4}{3f^3(N_{Re,BP})^8} .$$

The equation may also be expressed as the following:

$$f = \frac{16}{N_{Re,BP}} \left(\frac{1}{1 - 4x/3 + x^4/3} \right) , \qquad \textbf{(28)}$$

where $x = \tau_y/\tau_w$.

The critical Reynolds number for a Bingham plastic cannot be defined with a single value as it can for the Newtonian and Power Law models. Hanks and Pratt [1967] found that the critical Reynolds number can be determined from

$$(N_{Re,BP})_c = \frac{N_{He}}{8\, x_c} \left(1 - \frac{4}{3} x_c + \frac{1}{3} x_c^4\right) , \qquad \textbf{(29)}$$

where x_c = critical value of the τ_y/τ_w ratio.

The value of x_c may be determined from the following equation and then inserted into equation 29 to determine the critical Reynolds number:

$$\frac{x_c}{(1 - x_c)^3} = \frac{N_{He}}{16800} . \qquad \textbf{(30)}$$

3. SURROGATE SLURRY DEVELOPMENT AND PREPARATION

3.1 BASIS OF FORMULATION

Six of the MVSTs and two storage tanks at the evaporator service facility were sampled in late 1989 and early 1990 to determine the characteristics of the liquid wastes and sludges. Analytical results [Sears et al., 1990] and physical measurement data [Ceo et al., 1990] for these samples were published. It should be observed that the samples obtained from each tank were collected from only one location in the tank due to the inaccessibility of the tank and the radioactive nature of the wastes; therefore, the samples are not likely to be truly representative of the material in the tank. However, these data are the best analyses available, and they were the basis for developing a surrogate slurry for this study. The Ceo report focused on measuring the physical properties from four tanks: two MVSTs tanks (W-26 and W-28) and the two tanks at the evaporator service facility. More data were available for tank W-28; therefore, it was selected as the focus for preparing the surrogate slurry.

3.1.1 Chemical Analysis of MVST Samples

The samples of the MVSTs supernatant and sludges were analyzed for major constituents, radionuclides, total organic carbon, metals, and general waste characteristics. These data were used to identify possible chemical constituents in the MVST liquid and sludge waste. As previously mentioned, it was desired to formulate a surrogate without radioactive components. The analytical data from the MVSTs indicated that the Resource Conservation and Recovery Act (RCRA) metals were present in insignificant quantities compared with the non-RCRA metals; therefore, the RCRA metals were also neglected in the surrogate formulation.

Sears described the supernatant liquid wastes as high-pH sodium/potassium nitrate salt solutions. The principal anions found in the supernatant were nitrate, carbonate, and chloride. The nitrate concentration averaged about 4 *M*, and the chloride concentration was about 0.08 *M*. Sears also reported that the principal metals in the sludges were sodium, potassium, calcium, magnesium, uranium, and thorium. It was determined that the combined sodium and potassium accounted for ≈40 to 60 wt %, the combined calcium and magnesium accounted for 30 to 40 wt %, and the uranium plus thorium accounted for 4 to 20 wt % of the principal metals. Sears' study did not determine the anions present in the sludge phase. Uranium and thorium compounds were not used in the surrogate slurry because of the radioactive nature of these compounds. The concentrations of the other compounds were adjusted to account for the missing uranium and thorium compounds so that the proper concentration of solids was obtained.

3.1.2 Physical Measurement Data

Ceo performed physical measurements on the samples to determine the viscosity, particle size, density, sedimentation rate, and solids content. The data reported for the viscosity, density, and solids content were the criteria that were used in the development of the surrogate. These data are shown in Table 1.

3.2 SURROGATE SLURRY DEVELOPMENT

Several slurry recipes were prepared to simulate the MVST waste. Bench-scale testing was performed with these formulas to try to match a surrogate with the data reported by Ceo. The plastic viscosity and the yield stress of the surrogate slurries were determined with a Fann® Model 35 viscometer until a suitable surrogate was determined. The Fann viscometer, which

Table 1. Physical properties of MVST samples reported by Ceo et al. [1990]

Property	Analysis	W-26	W-28
Viscosity	Bulk liquid (cP)	1.67	2.22
	Neat sludge		
	Plastic viscosity (cP)	a	7700[b]
	Yield stress (dyn/cm^2)	a	22
	Sludge diluted 1:1		
	Plastic viscosity (cP)	70	130
	Yield stress (dyn/cm^2)	105	66
	Sludge diluted 1:3		
	Plastic viscosity (cP)	-	55
	Yield stress (dyn/cm^2)	-	20
Density	Bulk liquid (g/mL)	1.22	1.29
	Bulk sludge (g/mL)	1.36	1.40
	Interstitial liquid (g/mL)	1.23	1.29
	Undissolved solids (g/mL)	2.16	2.00
Sludge solids	Total solids (wt %)	46.0	51.4
	Dissolved solids (wt %)	23.6	29.4
	Undissolved solids (wt %)	22.4	22.0

[a]There was too much scatter in shear stress versus shear rate data to determine the plastic viscosity or yield stress.
[b]Coagulated during the test; not a true viscosity.

is a Couette coaxial cylinder rotational viscometer, was used because it covers a wide range of shear rates. The instrument was used to measure the shear stress at shear rates of 170, 340, 510 and 1020 s^{-1}. The fluid that is to be tested is contained in the annular space between an outer cylinder and the bob. Viscosity measurements are made when the outer cylinder rotates at a known velocity (i.e., shear rate) which creates a viscous drag to be exerted on the bob by the fluid. The drag causes a torque on the bob which is transmitted to a precision spring, where the deflection is measured and compared with the test conditions and the instrument constants [Baroid Drilling Fluids, Inc., 1989].

The formulation that showed the best comparison to Ceo's data formed a portion of the constituents by chemical reaction. The sludge compounds were formed by the chemical reaction of aluminum nitrate, calcium nitrate, and iron(III) nitrate with sodium hydroxide to form aluminum hydroxide, calcium hydroxide, iron(III) hydroxide, and sodium nitrate as shown in the following equations:

$$Al(NO_3)_3 + 3NaOH \rightarrow Al(OH)_3 + 3NaNO_3 , \quad \textbf{(31)}$$

$$Ca(NO_3)_2 + 2NaOH \rightarrow Ca(OH)_2 + 2NaNO_3 , \quad \textbf{(32)}$$

$$Fe(NO_3)_3 + 3NaOH \rightarrow Fe(OH)_3 + 3NaNO_3 . \quad \textbf{(33)}$$

These reactions may simulate the way that some of the sludges in the MVSTs were originally formed. The sodium nitrate formed from the reactions in equations 31 through 33 provided approximately 63% of the total sodium nitrate required for the recipe. The remaining sodium nitrate and the rest of the ingredients were added from commercially obtained chemicals.

After the bench-scale surrogate development work was completed, the recipe was modified to make up a 190-L (50-gal) batch of this slurry. Table 2 lists components of the slurry and the concentrations of the components. A procedure for preparing the 190-L batch is in Appendix A. Due to some anomalous reason, the plastic viscosity of the 190-L batch

Table 2. Components of the MVST surrogate slurry

Compound	Concentration (g/L)
Sodium nitrate	301
Sodium hydroxide	0.5
Sodium chloride	4.7
Sodium carbonate	21.1
Potassium nitrate	48.0
Calcium carbonate	196
Magnesium hydroxide	42.7
Silicic acid	8.4
Iron hydroxide[a]	1.7
Calcium hydroxide[b]	69.5
Aluminum hydroxide[c]	7.8

[a]This compound was formed by the reaction of iron nitrate and sodium hydroxide.
[b]This compound was formed by the reaction of calcium nitrate and sodium hydroxide.
[c]This compound was formed by the reaction of aluminum nitrate and sodium hydroxide.

did not match the viscosity of the 1-L batch even though the total solids content was determined to be approximately the same. The difference in plastic viscosity between the small batch and large batch is unknown, but it may be attributable to particle size or some other factor.

The consistency of the 190-L batch of surrogate slurry visually appeared to be reasonably similar to that of the MVST slurry after mixing for pipeline transport. Additional study may be needed to identify the factors that affect the rheology of the surrogate. Since one of the objectives of this study was to examine the effect of solids concentration, this batch of slurry was accepted for use in the slurry test loop. Prior to using the slurry for rheology studies, the slurry was heated to ≈60°C and recirculated through the test loop for a couple of hours. This step was intended to age the slurry to attempt to eliminate any changes (chemical or otherwise) that may affect the slurry during the various higher-temperature studies.

4. EXPERIMENTAL DESIGN AND PARAMETERS

4.1 DESCRIPTION OF EXPERIMENTAL SYSTEM

The surrogate slurry was recirculated through a loop to measure the parameters that would be converted to shear stress and shear rate, namely (1) pressure drop across pipes of known lengths and diameters and (2) flow rate. This loop is generally referred to as a slurry test loop. A piping and instrumentation diagram of the slurry test loop system is shown in Figure 4. The components of the system are described below.

4.1.1 Feed Tanks

The test loop included two feed tanks (F-100 and F-200), which were constructed from 55-gal stainless steel drums with conical sections added to the bottom of the drums. Although these tanks were constructed similarly, each feed tank had its own special features and duties.

F-100 was the main feed tank. The slurry was continually agitated in F-100 during operation periods by a vertically mounted air-operated agitator. The tank was outfitted with baffles to improve the mixing patterns. The slurry that was recycled to the tank was discharged through a tee nozzle positioned below the slurry level to disperse the slurry horizontally and bidirectionally to assist in keeping the solid particles suspended.

F-200 served as an auxiliary feed tank; however, F-200 was mounted on a weigh scale (Fairbanks® Model H90-3051) and used as a weighing tank for mass flow measurements. The mass flow rate was determined by temporarily diverting the recycle flow to F-200 and monitoring the increase in weight versus time. This measurement allowed verification of the volumetric flowmeter results. F-200 was also used to help homogenize the slurry after a settling period. To ensure that all of the solids were well mixed, the F-100 tank was allowed to pump

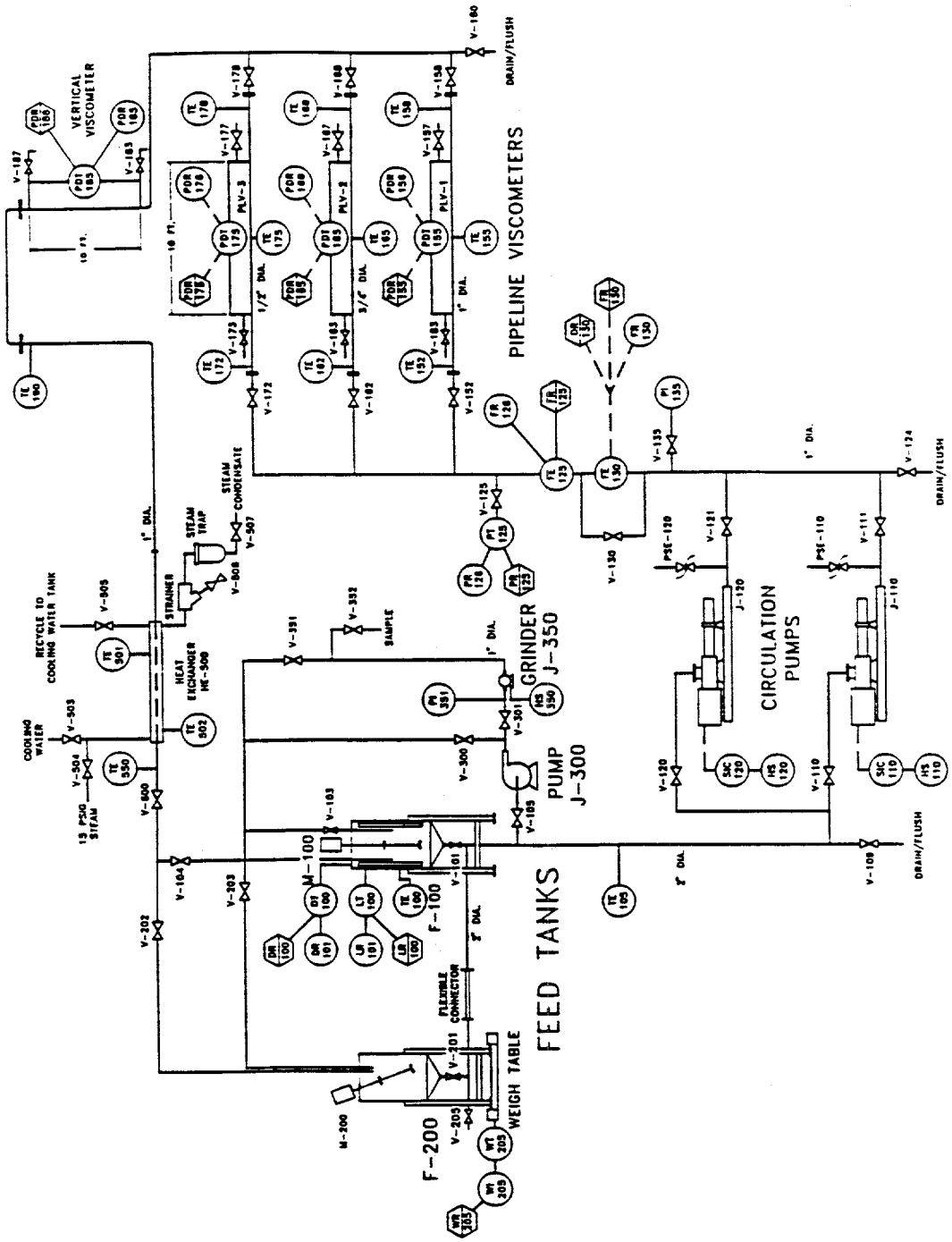

Figure 4. Schematic of experimental test system.

nearly empty while the slurry was being collected in F-200. Just before F-100 became empty, the recirculation stream was diverted from F-200 to F-100; the feed tanks were then reversed (F-200 was the feed tank and F-100 was the collection tank) until F-200 was nearly empty. This procedure was performed a couple of times before every run and intermittently during the run to help ensure that the slurry was remaining well mixed. F-200 was also equipped with an angle-mounted air-operated agitator, but it was not used very often since the tank was empty most of the time.

4.1.2 Recirculation Pumps

Two recirculation pumps were included in the system. Both pumps were Moyno® pumps (progressive cavity pumps) that were selected to provide a steady pumping rate. The small pump (J-110) had a pumping capacity ranging from 0 to ≈23 L/min (0 to 6 gal/min). The larger pump (J-120) had a pumping capacity of approximately 7.6 to 114 L/min (2 to 30 gal/min). The rotor shafts were sealed with water-pressurized graphite-impregnated Teflon packing. The rotors were fabricated of 316 stainless steel, and the stators were manufactured from EPDM (an elastomer of ethylene propylene copolymer and terpolymer).

4.1.3 Density Determination

As the slurry recirculated through the test loop, it passed through a Micro Motion® mass flowmeter (Model D25-D300). This instrument is a mass flowmeter and a density measurement instrument; however, it was used only to measure the slurry density in the test loop system. The instrument's principle of operation is based on the Coriolis force that causes the twisting of the flow tubes in the unit. Since this instrument could cause a high-pressure drop and limit the pumping capacity, a bypass was installed to allow fluid to flow around the instrument but

still permit fluid flowing through the instrument for continuous density measurement. This instrument is identified as FE 130 in Figure 4.

4.1.4 Volumetric Flow Measurement

The volumetric flow rate was measured by an Endress+Hauser® Variomag® magnetic flowmeter (identified as FE 125 in Figure 4). These flowmeters utilize the properties of a conductive liquid to generate an induced voltage as the liquid flows through a magnetic field to measure the volumetric flow rate [Rose, 1993]. The amplitude of the induced voltage is directly proportional to the liquid flow rate. The results obtained from this instrument compared very well with those obtained from mass flow measurements with the weigh tank.

4.1.5 Pressure Measurement

The system pressure was monitored by a Rosemount® remote sealed-diaphragm pressure transmitter (Model 1151GP). The instrument measures the process pressure by transmitting the pressure through an isolating diaphragm and oil fill fluid to a sensing diaphragm. The sensing diaphragm moves to a position which is proportional to the process pressure. This instrument is identified in Figure 4 as PT 125.

4.1.6 Differential Pressure Measurement

Three horizontal viscometers were arranged in parallel, but only one was used at a time for data collection. A vertical viscometer was installed in series with the horizontal viscometers. The purpose of the vertical viscometer was to show whether solid particles were settling in the horizontal pipes during the rheological measurements. If settling was occurring in the horizontal viscometers, the effective diameter of the pipe would be reduced and the

pressure drop would increase. The pressure drop across the vertical viscometer should not be affected by settling particles. The data obtained from the horizontal viscometers could be compared with the data from the vertical viscometer to determine whether settling occurred.

The horizontal viscometers were constructed from 1-, 0.75-, and 0.5-in. Schedule 40 stainless steel (304) pipe. The vertical viscometer was constructed from 1-in. Schedule 40 stainless steel pipe. The upstream pressure tap was positioned 120 pipe diameters downstream of the flanged connector on the horizontal viscometers; however, because of space limitations, the upstream pressure tap on the vertical viscometer was placed approximately 15 pipe diameters above a smooth bend. The distance between the pressure taps was 3.05 m (10 ft) on each viscometer. The downstream pressure tap was positioned approximately 20 pipe diameters upstream of the flanged pipe connector. A valve was provided on each end of the viscometers to isolate the flow through the desired viscometer.

A schematic diagram of a typical pipeline viscometer is shown in Figure 5. The pressure taps were installed by welding a 1.3-cm (0.5-in.) length of 0.5-in.-diameter bar stock on the pipe at the desired position. A 3-mm (1/8-in.) hole was drilled through the bar stock and pipe wall, and the drilled hole was deburred to removed any metal fragments. A 5-cm (2-in.) piece of 1/4-in. Schedule 40 pipe was welded onto the bar stock. Threads were provided on the pipe to permit connection to the remote sealed-diaphragm pressure sensors.

Two brands of pressure differential transmitters were used. A Rosemount® Smart Transmitter (Model 1151DP) was used for measuring the pressure drop across the 3.05-m section of the 1-in. horizontal viscometer. Honeywell® Smart Transmitters (Model ST3000) were used with the 0.75- and 0.5-in. horizontal viscometers and the 1-in. vertical viscometer. The principle of operation for these instruments is similar to that of the Model 1151GP pressure

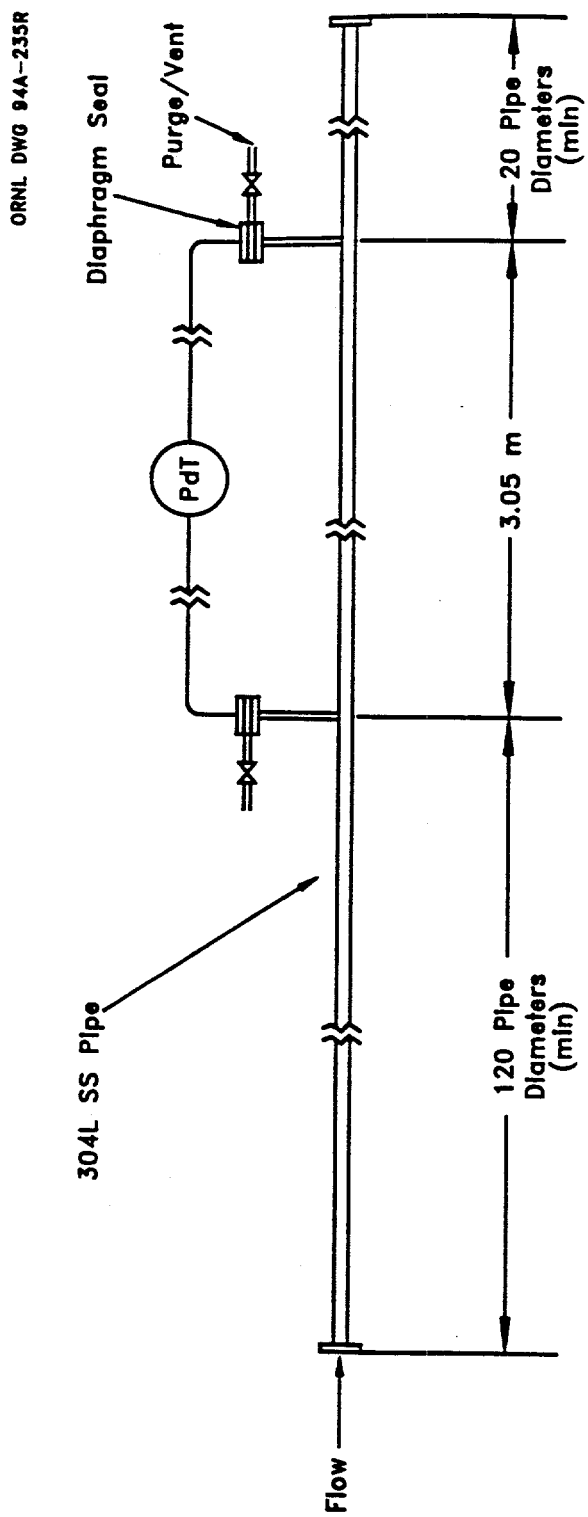

Figure 5. Schematic of a pipeline viscometer.

transmitter described above. The difference is that these instruments measure the pressure at two points and determine the difference in pressure between the two points.

4.1.7 Temperature Measurement

Type K thermocouples were strategically positioned throughout the system, but the most important area was the pipeline viscometers. Thermocouples were installed at the entrance and exit of each pipeline viscometer. The slurry temperature was determined by the arithmetic average of the output from these thermocouples; however, the outputs from the thermocouples were comparable.

4.1.8 Temperature Control

The temperature of the slurry was controlled by removing or adding heat, as required, through the in-line heat exchanger (HE 500), which was a single-tube shell and tube heat exchanger. Heat was supplied by 15-psig steam, and excess heat was removed by chilled water. The flow rate of steam and/or cooling water was controlled manually.

4.1.9 Data Acquisition

Data obtained during the operation of the loop were monitored and recorded by a data acquisition system. Genesis® software was used for this purpose. Recorded data were imported into LOTUS® 1-2-3® for calculations and analysis.

4.1.10 Other Equipment

Other equipment included in the test loop system include a pump (J-300) and an in-line grinder (J-350). These items were installed for use with another project, and they were not used in this project.

4.2 TEST LOOP OPERATION

After mixing the slurry to obtain a homogeneous mixture, data were collected at various flow rates ranging from 0 to ≈114 L/min (0 to ≈30 gal/min). At least 1 min was allowed for the slurry to reach steady state after adjusting the flow rates. Data were collected approximately every 5 s over a period of approximately 2 min at each selected flow rate. The temperature was monitored and adjusted as necessary to remain within the test parameters.

4.3 OTHER TESTS PERFORMED

Samples were collected from each of the runs performed. The settling rate of the suspended solids from selected runs was measured by pouring a well-mixed sample into a 1-L graduated cylinder and then recording the suspended solids interface versus elapsed time.

5. DATA AND RESULTS

5.1 SUCROSE CALIBRATION

Prior to using the test loop with slurries, it was demonstrated that the pipeline viscometers would work properly with a Newtonian fluid. Sucrose was selected as the Newtonian fluid, since there are some viscosity data for sucrose in literature. Data were collected for sucrose in the same manner as would be used for slurries. Two concentrations of sucrose (50 and 60 wt %) were analyzed by the test loop. Plots of pressure drop versus flow rate are shown for the two concentrations of sucrose in Figures 6 and 7. Diagrams of shear stress versus shear rate for the sucrose solutions are shown in Figures 8 and 9. The viscosity measured by each of the pipeline viscometers agreed well the others. The measured viscosity compared within 2% of literature values in the *International Critical Tables* [1929].

5.2 SURROGATE SLURRY TESTS

Twelve runs were made with the test loop using MVST surrogate slurries. The test conditions are shown in Table 3. An explanation is required for the two columns in Table 3 that are labeled "Total solids." The first column shows the results obtained in our laboratory. The second column shows the results obtained by the ORNL Analytical Chemistry Division when the surrogate slurry was analyzed by the method described by Ceo for determining the quantity of dissolved and undissolved solids. Ceo's method is included in Appendix A. The two analyses for total solids agreed within 10%.

The experiments were divided into four categories. The first three categories involved varying the concentration of dissolved and undissolved solids in the slurry by adding or removing supernatant and varying the slurry temperature. The objective of the fourth category,

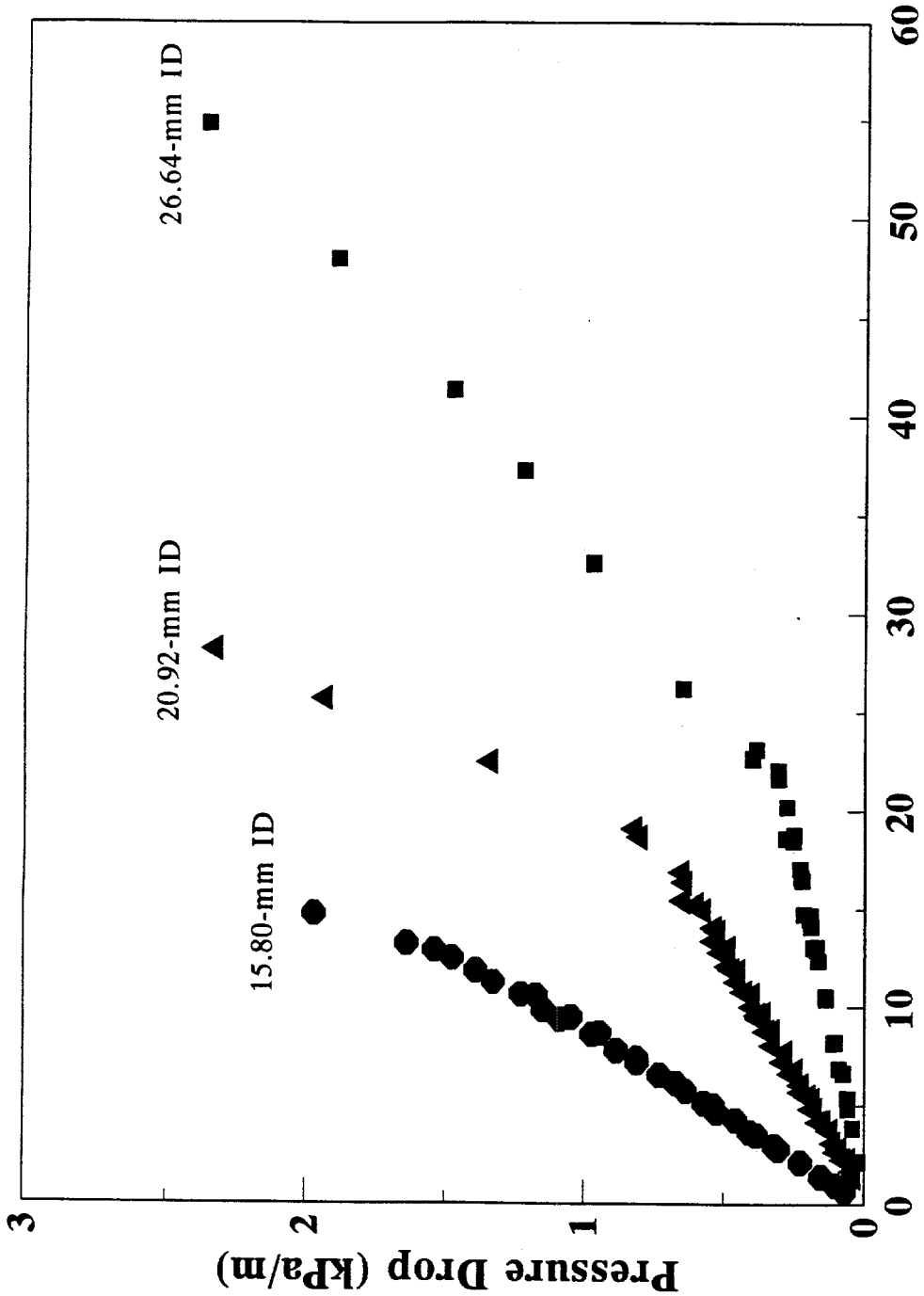

Figure 6. Pressure drop versus flow rate (sucrose 50 wt %).

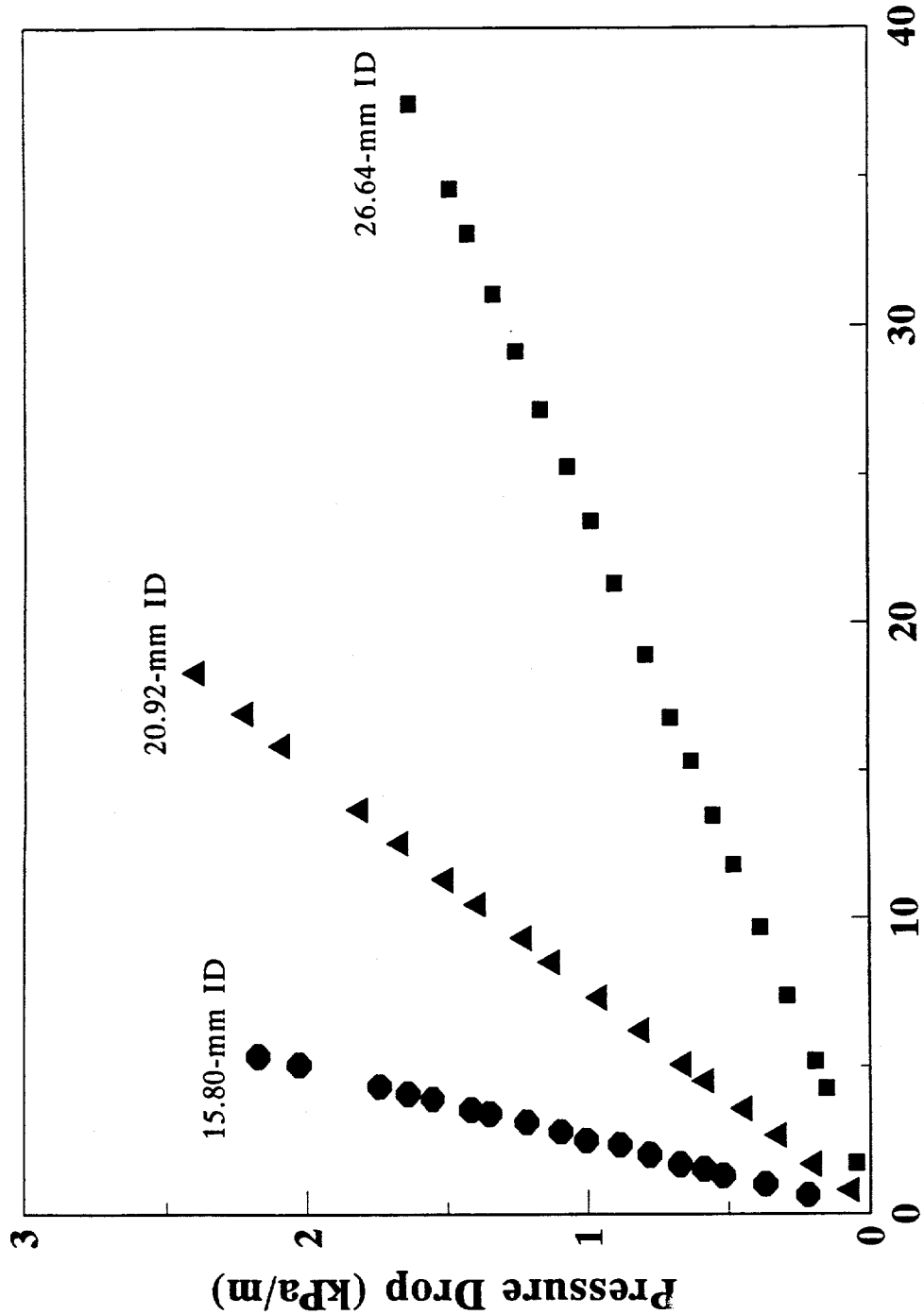

Figure 7. Pressure drop versus flow rate (sucrose 60 wt %).

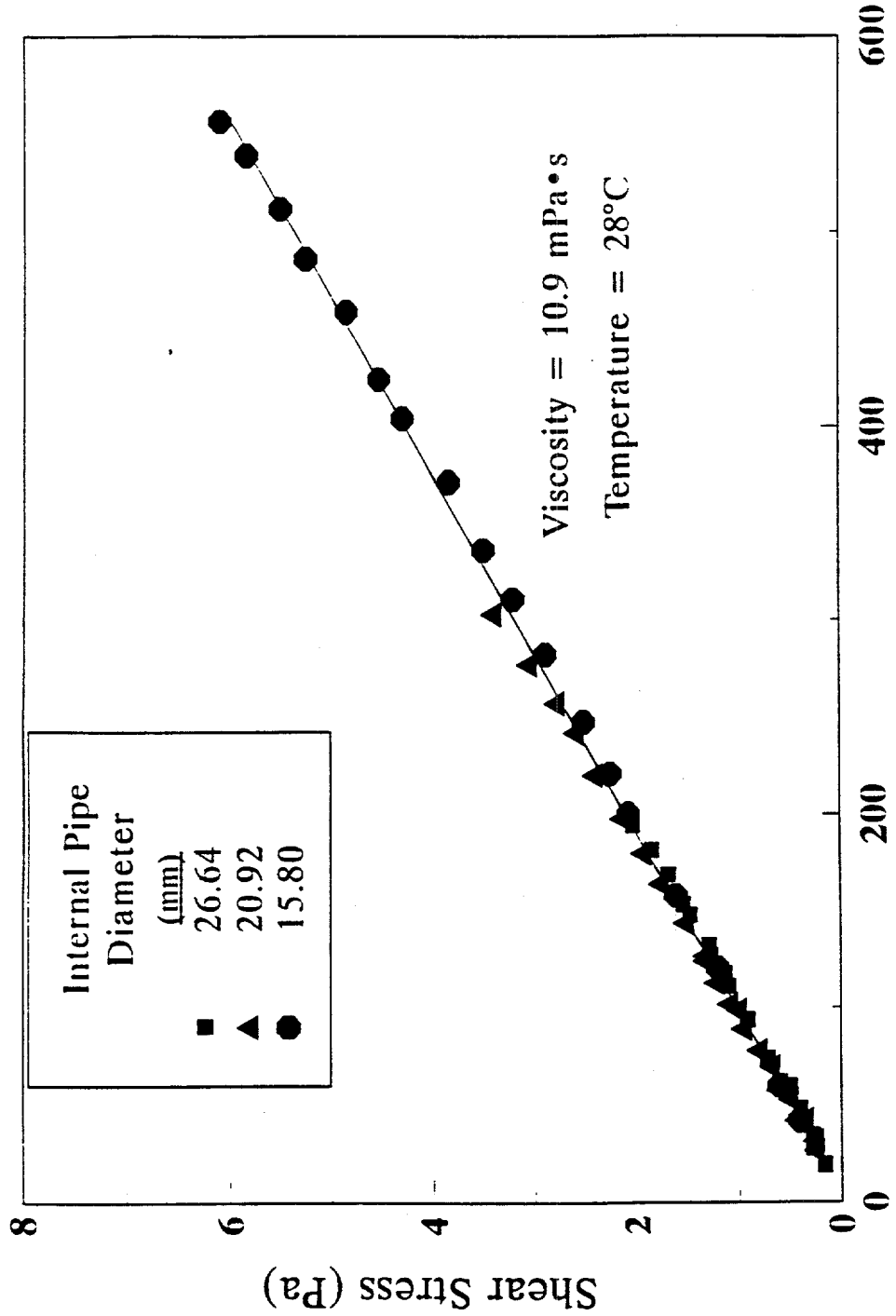

Figure 8. Shear stress versus shear rate (sucrose 50 wt %).

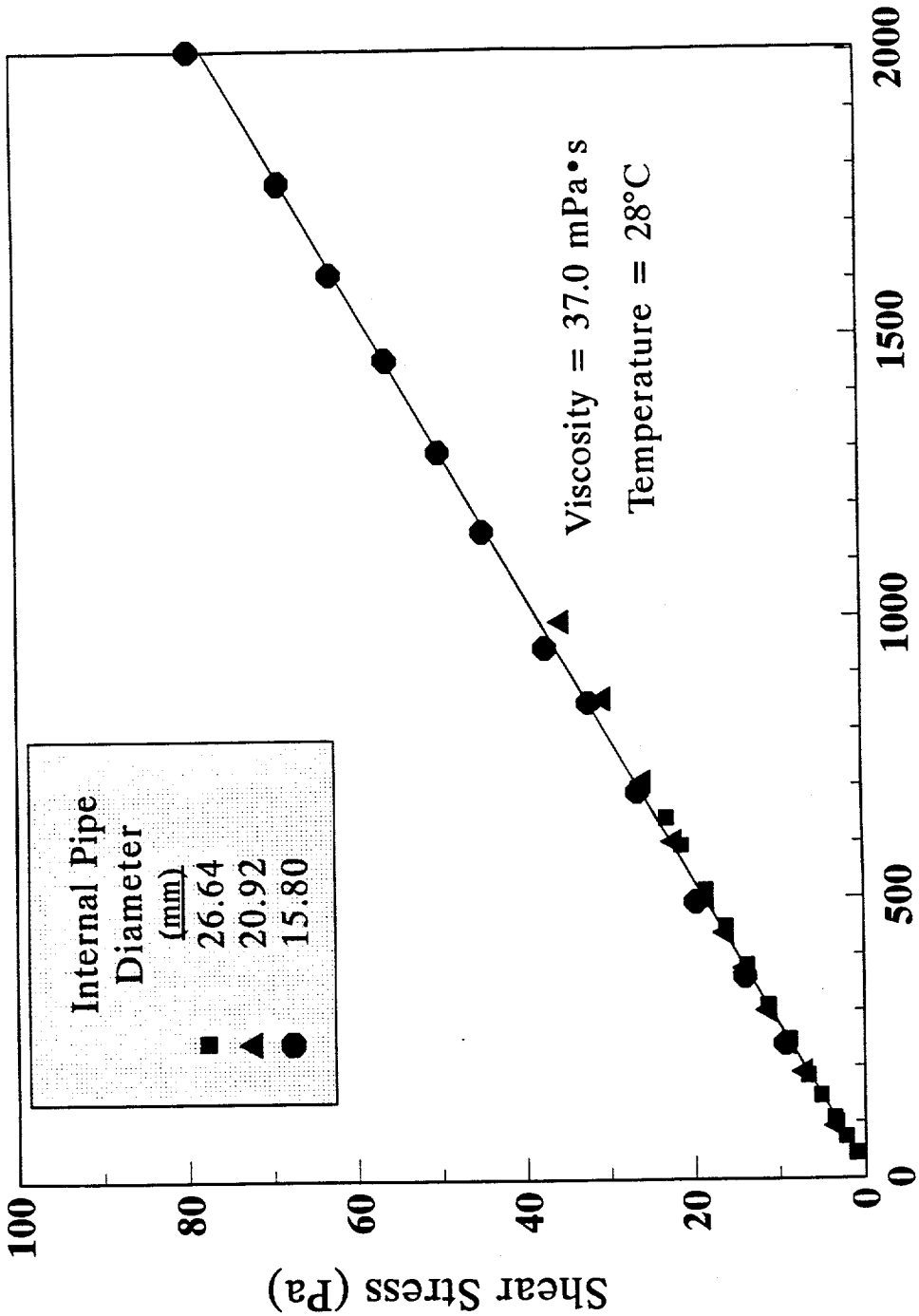

Figure 9. Shear stress versus shear rate (sucrose 60 wt %).

Table 3. Compilation of run conditions for the slurry test loop

Run number	Slurry temperature (°C)	Slurry density (g/mL)	Total solids (wt %)	Results from the Ceo method for solids		
				Undissolved solids (wt %)	Dissolved solids (wt %)	Total solids (wt %)
A-1	25	1.41	47.6	27.1	24.2	51.3
A-2	35	1.41	48.0			
A-3	45	1.42	49.2			
A-4	25	1.44	49.9			
B-1	25	1.48	52.9	33.9	24.0	57.9
B-2	35	1.47	52.9			
B-3	25	1.48	53.2			
C-1	25	1.41	47.3	25.8	26.3	52.1
C-2	35	1.40	47.2			
D-1[a]	25	1.44	49.2	27.9	24.6	52.5
D-2[b]	25	1.44	48.0	24.6	23.2	47.8
D-4[c,d]	25	1.44	44.5	23.3	21.8	45.1

[a]Glass spheres of nominal 90-μm diameter were added to the slurry following run C-2.
[b]Glass spheres of nominal 200-μm diameter were added to the slurry following run D-1.
[c]Glass spheres of nominal 500-μm diameter were added to the slurry following run D-2.
[d]Run D-3 was aborted when the inlet line to the Moyno pump plugged with solids.

which involved adding glass spheres of known nominal size to the slurry, was to determine the minimum transport velocity (also known as deposition velocity), which is defined as the velocity at which a particle bed begins to form. The minimum transport velocity represents the lower limit of safe operation in pipeline flow of slurries. It is directly related to the fall velocity of the particles and to the degree of turbulence in the system. The minimum transport velocity will increase as the particle size, particle density, and solids concentration increase, and it will also increase as the pipe diameter is increased [Wasp et al., 1979].

The glass spheres had a specific gravity of 2.55, which is in the range of densities for the insoluble components of the slurry. Nominal diameters of 90, 200, and 500 μm (see Appendix B for information sheets for the glass spheres) were used during these tests. These sizes were selected to be conservative in determining the minimum transport velocity. If the slurry velocity was not sufficient to keep the spheres suspended, the spheres settled in the horizontal pipelines, which reduced the diameter of the horizontal pipes and caused the pressure drop to increase. If settling does not occur, the pressure drop (due to friction) in the 1-in.-diameter horizontal viscometer and the 1-in.-diameter vertical viscometer should remain equivalent. Therefore, the minimum transport velocity could be determined from comparing the pressure drop versus velocity curves at the point that the pressure drop reached a minimum in the 1-in.-diameter horizontal viscometer.

5.3 RESULTS

5.3.1 Bingham Plastic Model Results

A diagram of the pressure drop versus flow rate for a typical run is shown in Figure 10. The techniques discussed in Section 2.2 were used to convert these data into shear stress and

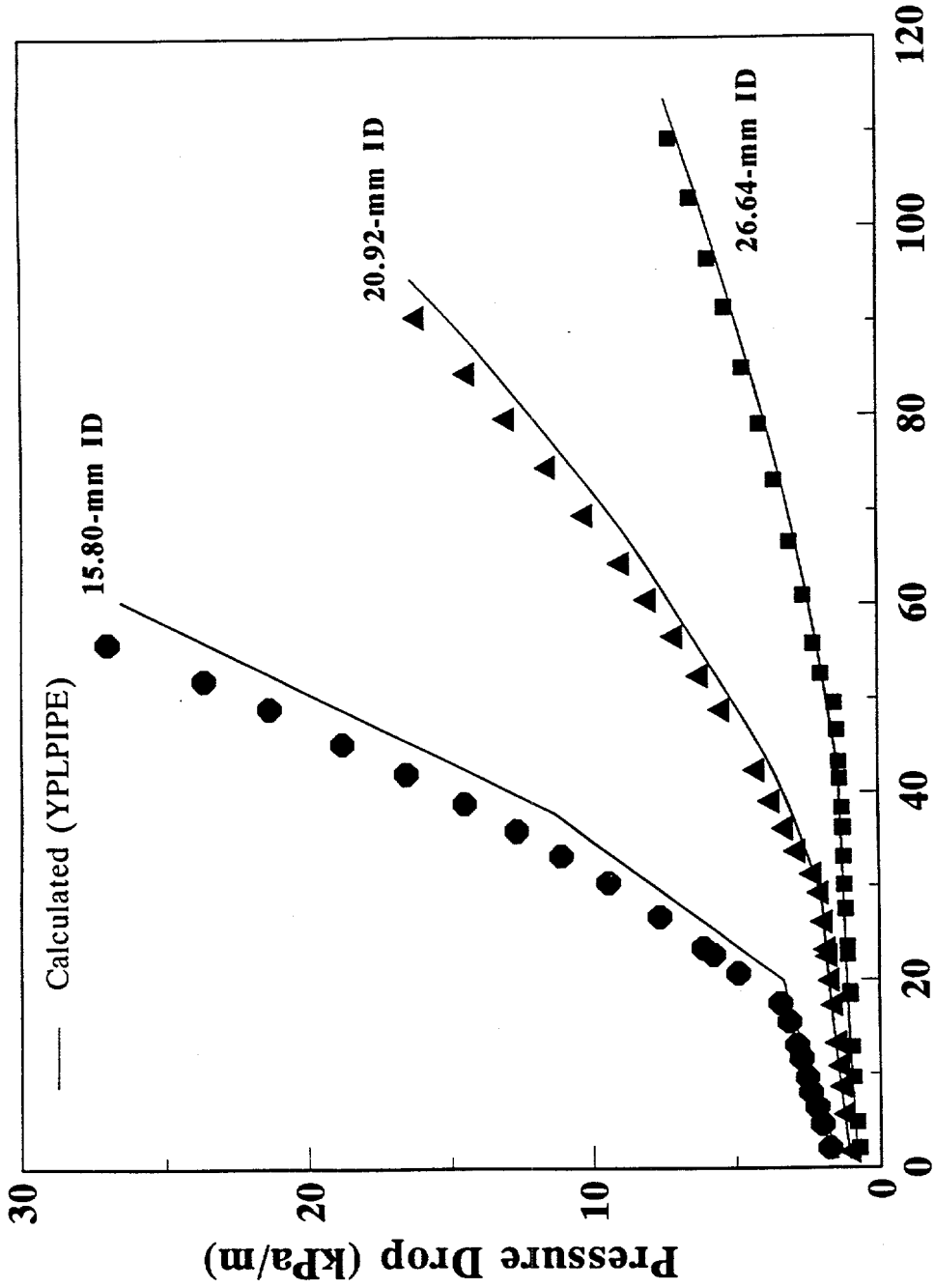

Figure 10. Typical pressure drop versus flow rate for MVST surrogate slurry.

shear rate data. Figure 11 is a plot of shear stress versus shear rate (commonly referred to as a rheogram) for the pressure drop data (in the laminar region) shown in Figure 10 as analyzed according to the Bingham plastic model. The dashed lines in Figure 11 represent the Bingham plastic analysis for the individual pipeline viscometers. The solid line represents the Bingham plastic analysis by combining and analyzing the data from all three viscometers. The diagrams of pressure drop versus flow rate and shear stress versus shear rate for runs A-1 through C-2 were similar in appearance to Figures 10 and 11. A complete set of the pressure drop diagrams is included in Appendix C, and a complete set of rheograms is included in Appendix D. The lines drawn in Figure 11 and Appendix D were analyzed for statistical fit by the correlation factor r^2 (i.e., sum of residuals squared). The r^2 values are included with the rheology data in the rheograms. The Bingham plastic rheology data for these runs are compiled in Table 4.

In the absence of all experimental error, the shear stress–shear rate lines for each of the pipeline viscometers shown in Figure 11 should be on top of each other; however, it should be noted that the magnitude of pascal units is very small (101,325 Pa = 1 atm), and the graph's scaling may magnify the difference between the viscometers. The space between the lines in the rheogram indicates that slippage may be occurring at the walls of the pipe. Heywood [Brown et al., 1991] describes a procedure for determining the wall slip velocity (V_s). This procedure involved determining values of 8V/D at fixed values of τ_w for the various pipe diameters. The 8V/D data were plotted against 1/D for the various constant values of τ_w. When a straight line is drawn through each set of constant τ_w, the slope of the line is equivalent to $8V_s$. A typical diagram should look similar to that shown in Figure 12. This procedure was used with the data obtained from the test loop with each of the runs; however, the analysis indicated that the wall slip velocity was either negative or unreasonable for all of the runs.

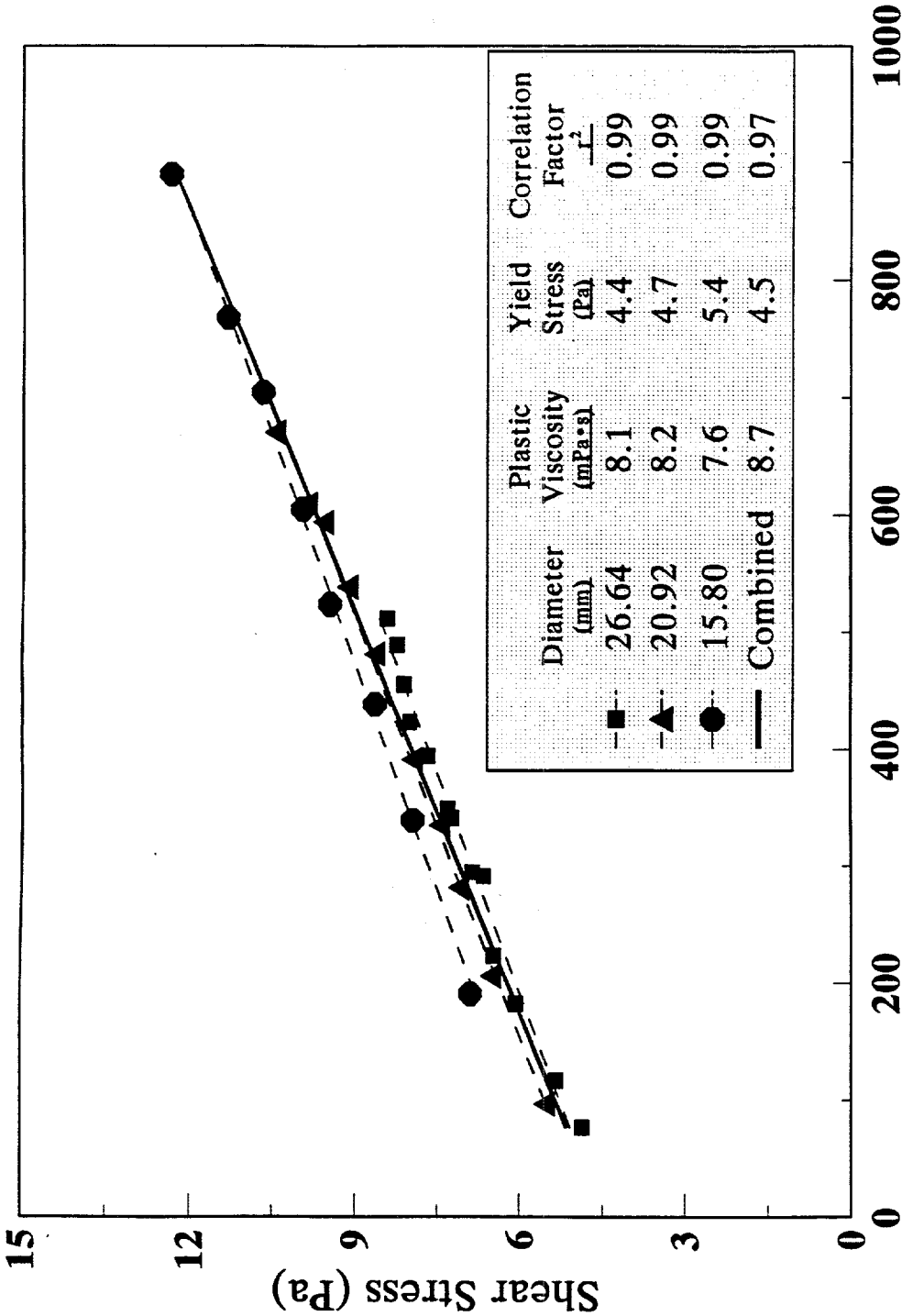

Figure 11. Typical rheogram for MVST surrogate slurry (Bingham plastic).

Table 4. Compilation of results from the Bingham plastic model analysis

Run number	Slurry temperature (°C)	Bingham plastic model results: Plastic viscosity (mPa·s)	Bingham plastic model results: Yield stress (Pa)
A-1	25	8.1	2.4
A-2	35	7.4	3.3
A-3	45	6.6	4.8
A-4	25	8.0	4.8
B-1	25	12.0	5.7
B-2	35	10.6	5.0
B-3	25	11.8	4.2
C-1	25	6.4	0.93
C-2	35	5.4	0.87
D-1	25	NA[a]	NA[a]
D-2	25	NA[a]	NA[a]
D-4	25	NA[a]	NA[a]

[a]NA = not applicable.

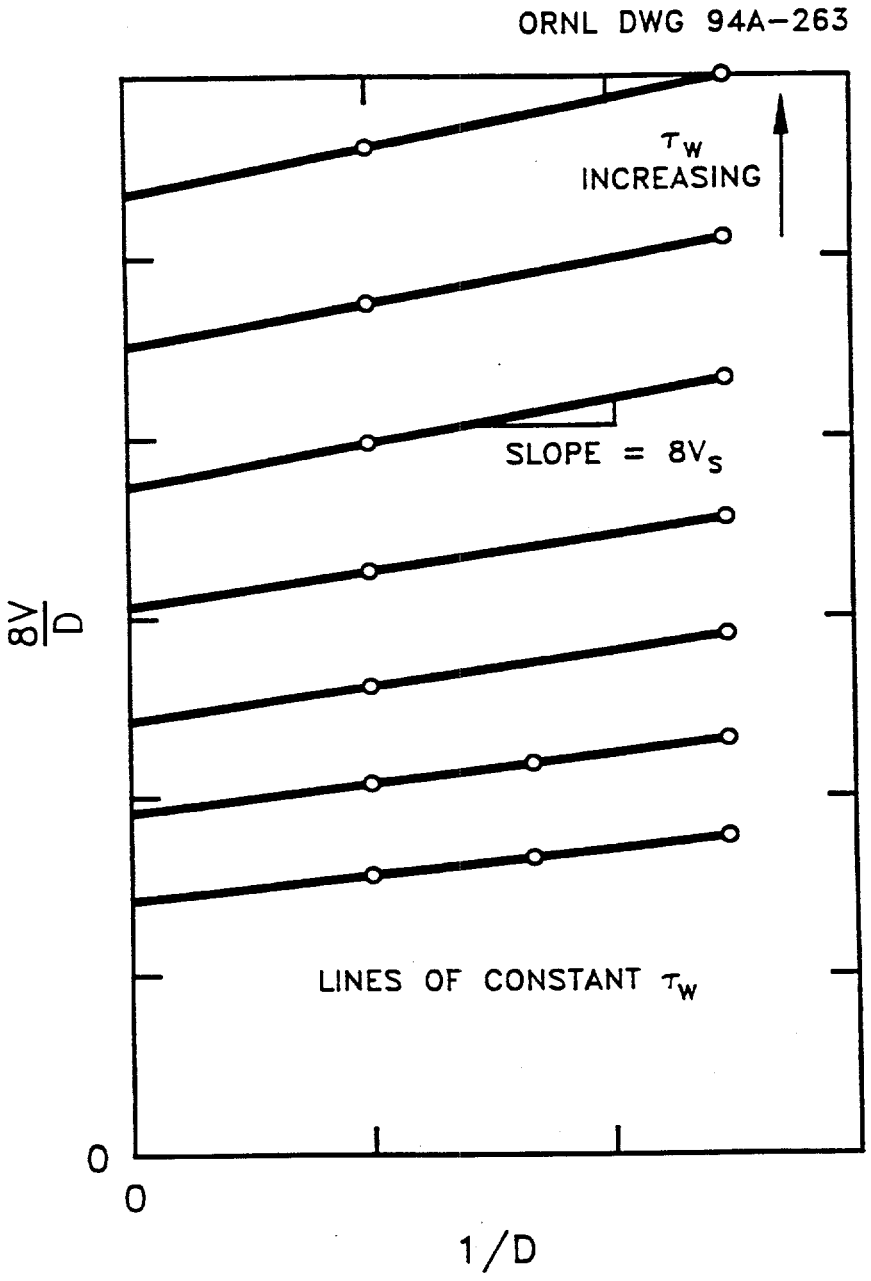

Figure 12. Example of method for determining wall slip velocity.

Adapted with permission from N. I. Heywood, "Rheological Characterisation of Non-settling Slurries," Chapter 4 in N. P. Brown and N. I. Heywood (eds.), *Slurry Handling Design of Solid-Liquid Systems*. Elsevier Science Publishers, Essex, England, 1991.

Since it is impossible to have a negative wall slip velocity or a wall slip velocity that is greater than the fluid velocity, it was assumed that the actual wall slip velocity was less than our experimental design and techniques could detect. Therefore the wall slip velocity was assumed to be negligible for the purposes of determining the rheologies of the slurries.

The pressure differential data from the vertical viscometer (due to friction) were consistently higher than the pressure drop data measured with the same-size horizontal viscometer. This was true for the sucrose calibration fluid and the surrogate slurry. When the vertical viscometer was constructed, the flow-smoothing section included a smooth bend with only 15 pipe diameters space between the bend and the first pressure-sensing point. The bend may have caused fluid turbulence, which resulted in higher a pressure drop measured with the vertical viscometer. It was decided that the data from the vertical viscometer should not be used in determining the rheology of the slurries; however, the vertical viscometer performed an important role in determining the minimum transport velocity, which is discussed later in this report.

R. W. Hanks has developed a software program titled Yield Power Law Pipeline Design Program (YPLPIPE) for pipeline design. As indicated by the program title, the program models non-Newtonian behavior with the Yield Power Law model based on information supplied by the user. However, YPLPIPE may also be used for fluids that can be modeled by the Power Law, Bingham plastic, and Newtonian models. The program requires entering the following parameters about the fluid: flow rate, pipe diameter, slurry density, consistency (K), flow behavior parameter (n), and yield stress (τ_y). If $\tau_y = 0$, the program computes the Power Law parameters based on the method of Hanks and Ricks [1975]. If $n = 1$, $K = \eta$, and $\tau_y \neq 1$, the program uses the method of Hanks and Dadia [1971] to compute the Bingham plastic behavior.

The program will calculate the Newtonian flow parameters if $\tau_y = 0$, $K = \mu$, and $n = 1$. YPLPIPE also calculates the Reynolds number, the critical Reynolds number, and the friction factor for a given set of data. It will also calculate the Hedström number when computing the Bingham plastic model. YPLPIPE is commercially available.

The Bingham plastic parameters obtained from our experimental testing were entered into the YPLPIPE program to compare the measured pressure drop results with the predicted pressure drop results as a function of flow rate. The solid lines shown in Figure 10 and Appendix C represent the results provided by the YPLPIPE program. The program's predicted pressure drops compared well with the pressure drop measured with the test loop data. This software program could prove useful for designing the pipeline for transporting the actual MVST slurry.

The plastic viscosity of the slurries increased as the concentration of suspended solids increased as demonstrated in Figure 13. However, this relationship, as expected, is shown to be nonlinear. Although a linear regression could be performed on the data, it would have little meaning. At best, the linear regression could be used for interpolation; however, extrapolation beyond the data could be dangerous. For example, if one were to extrapolate back to zero percent suspended solids, the predicted plastic viscosity would be less than zero, which is not possible.

The friction factors were calculated from equation 14 and compared with the friction factor determined from equation 26 for the laminar region. The results of a typical evaluation are shown in Figure 14, and a complete set of diagrams for each of the runs is attached in Appendix E. Equation 26 is used by Hanks in his computer program YPLPIPE for the laminar region for the Bingham plastic model. The line drawn in the turbulent region was determined from the YPLPIPE program.

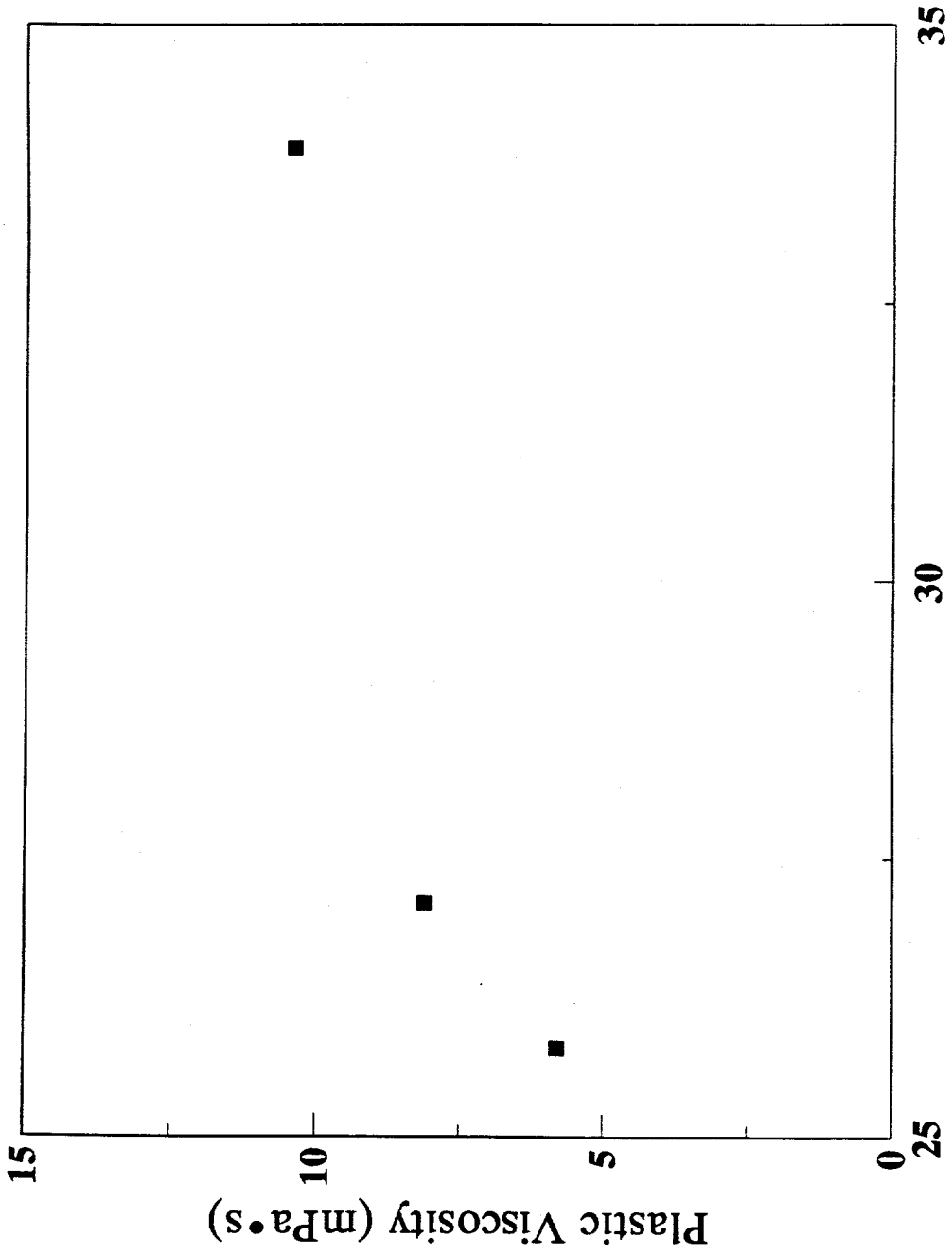

Figure 13. Relationship of plastic viscosity to suspended solids concentration.

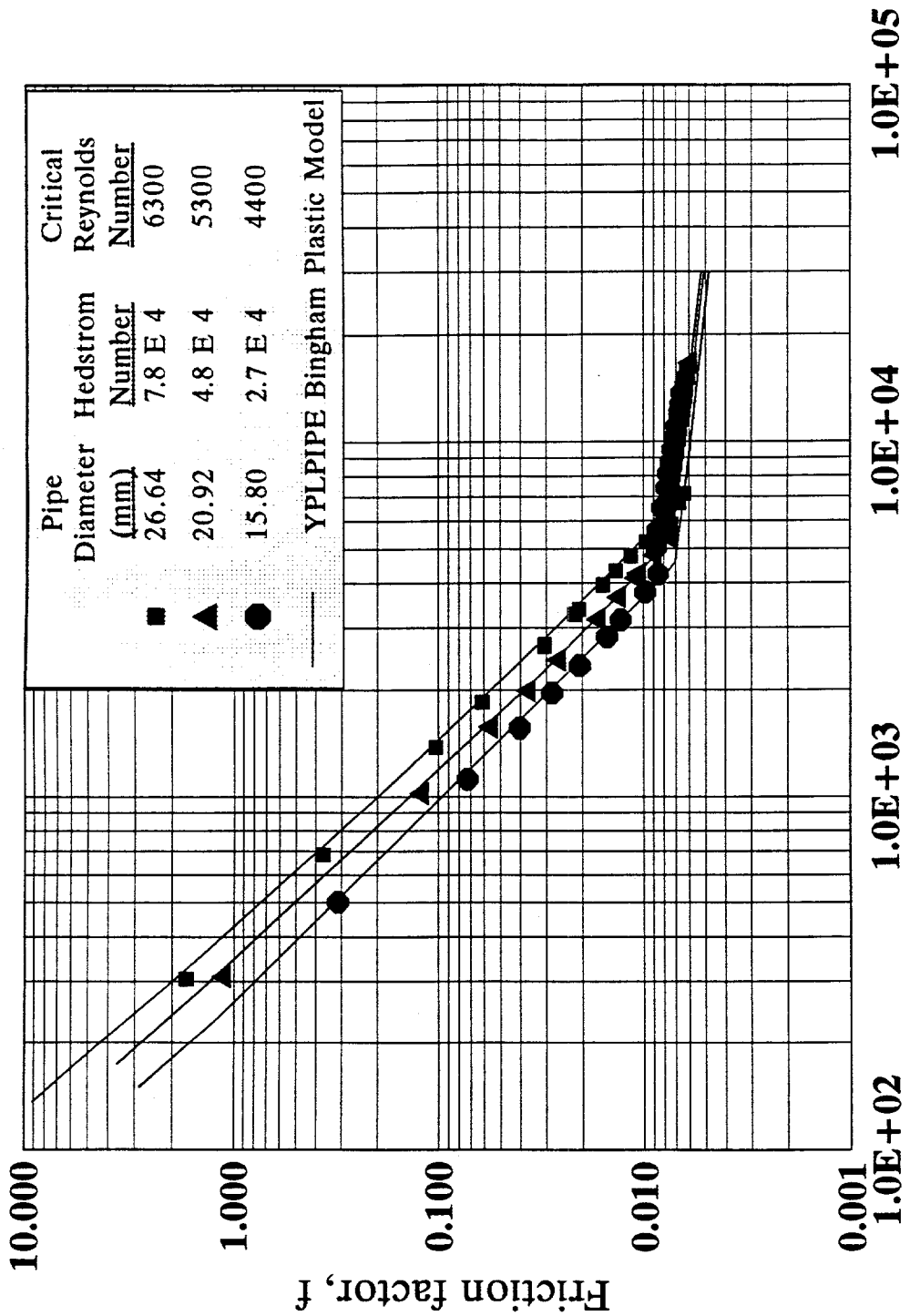

Figure 14. Fanning friction factor versus Reynolds number (Bingham plastic model).

The results indicate that temperature has little effect on the rheological properties of the slurries. The plastic viscosity of the slurries was observed to decrease slightly as the slurry temperature increased. This is a reasonable result since the temperature would not change the properties of the suspended solids much when compared to a pure liquid, and the slurries contained a large amount of suspended solids.

5.3.2 Power Law Model Results

The laminar flow portions of the pressure drop versus flow rate curves (which are in Appendix C) were reanalyzed to determine the shear stress and shear rate of the slurries with the Power Law model. These data were also converted to shear stress and shear rate using the techniques described in Section 2.2. A rheogram example is shown in Figure 15 for a Power Law analysis of the data. The dashed lines indicate the analysis for each individual horizontal pipeline viscometer. The solid line represents the results for all three viscometers combined. These lines were also analyzed for statistical fit with the correlation factor r^2 (i.e., sum of residuals squared), and the factors are included in the rheogram figures. A complete set of Power Law rheograms is included in Appendix F.

Once again the curves shown in the rheogram should have been indistinguishable in the absence of experimental error. As discussed in the Bingham plastic model results, a portion of the error may be attributable to wall slip. However, the analysis for wall slip velocity indicated that this value was either negative or greater than the measured slurry velocity, which is not possible. Therefore the wall slip velocity was assumed to be negligible for the analysis of the Power Law parameters.

The determination of K' and n' was made as discussed and demonstrated in Section 2.2. For a Power Law fluid, n' is equivalent to the Power Law exponent n. The Power Law

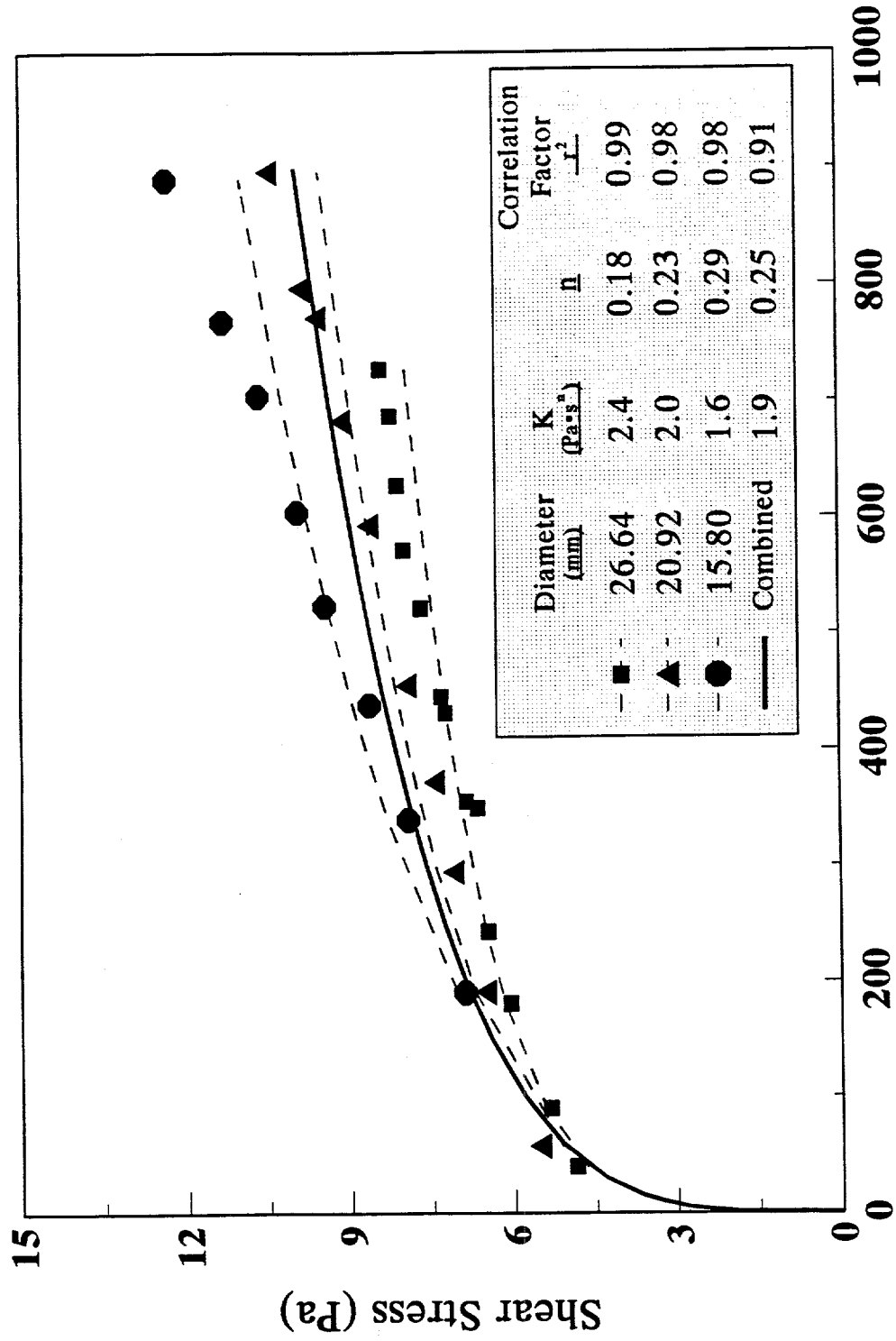

Figure 15. Typical rheogram for MVST surrogate slurry (Power Law model).

consistency factor (K) was determined by equation 24. The three curves were analyzed individually and combined to obtain one value of K and n. The dashed lines in the rheograms represent the individual pipeline viscometer analyses, and the solid line represents the combined data from all three viscometers. Table 5 compiles the Power Law model factors for runs A-1 through C-2.

The friction factors were calculated from equation 22 and compared with equation 14. The results of a typical comparison are shown in Figure 16, and a complete set of diagrams is in Appendix G for runs A-1 through C-2. The lines drawn in the laminar region correspond to equation 22, and the line in the turbulent region corresponds to equation 23.

In general, the K values increased as the suspended solids concentration increased. The value of the Power Law exponent remained approximately the same for the A- and B-series of runs, but increased slightly for the lower suspended solids concentration analyzed in the C-series of runs. The effect of temperature on the K and n values was not consistent, so no conclusion can be reached for these data.

5.3.3 Minimum Transport Velocity

The minimum transport velocity was determined by adding glass spheres to the surrogate slurry. The glass spheres had a specific gravity of 2.55 and size tolerances of 80–110, 160–250, and 400–520 μm. Pressure drop versus velocity diagrams are shown for runs D-1, D-2, and D-4 in Figures 17 through 19. It should be noted in these figures that the pressure drop in the horizontal pipeline viscometers shows a minimum, whereas the vertical pipeline viscometer, as expected, did not exhibit the same behavior. The minimum value of pressure drop in the horizontal viscometer determines the minimum transport velocity. The minimum transport velocity is indicated on the diagrams.

Table 5. Compilation of results from the Power Law model analysis

Run number	Slurry temperature (°C)	Power Law model results	
		K ($Pa \cdot s^n$)	n
A-1	25	1.0	0.26
A-2	35	1.4	0.24
A-3	45	2.9	0.18
A-4	25	1.9	0.25
B-1	25	2.7	0.22
B-2	35	2.4	0.22
B-3	25	1.6	0.27
C-1	25	0.46	0.33
C-2	35	0.43	0.34
D-1	25	NA[a]	NA[a]
D-2	25	NA[a]	NA[a]
D-4	25	NA[a]	NA[a]

[a] NA = not applicable.

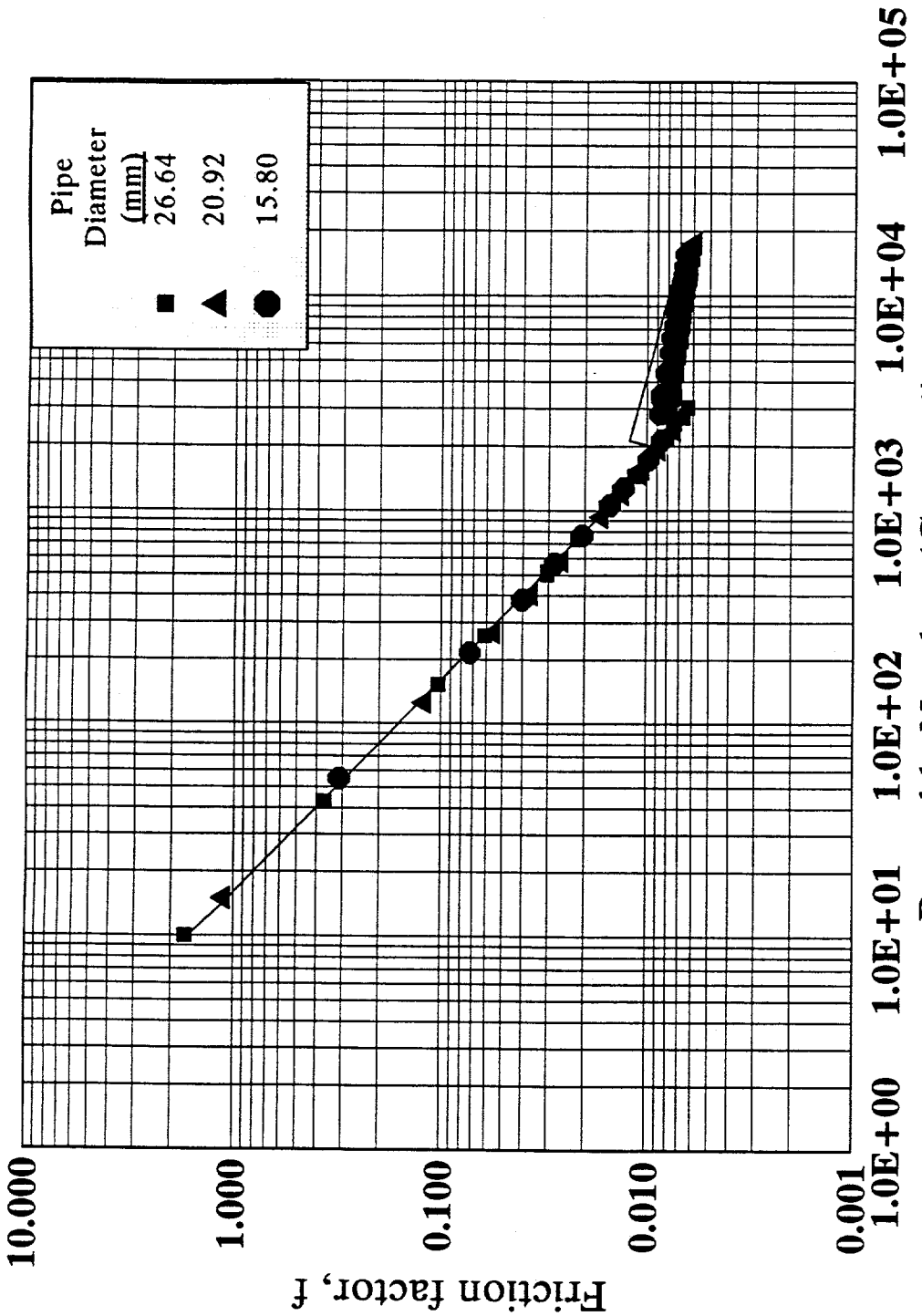

Figure 16. Friction factor versus Reynolds number (Power Law model).

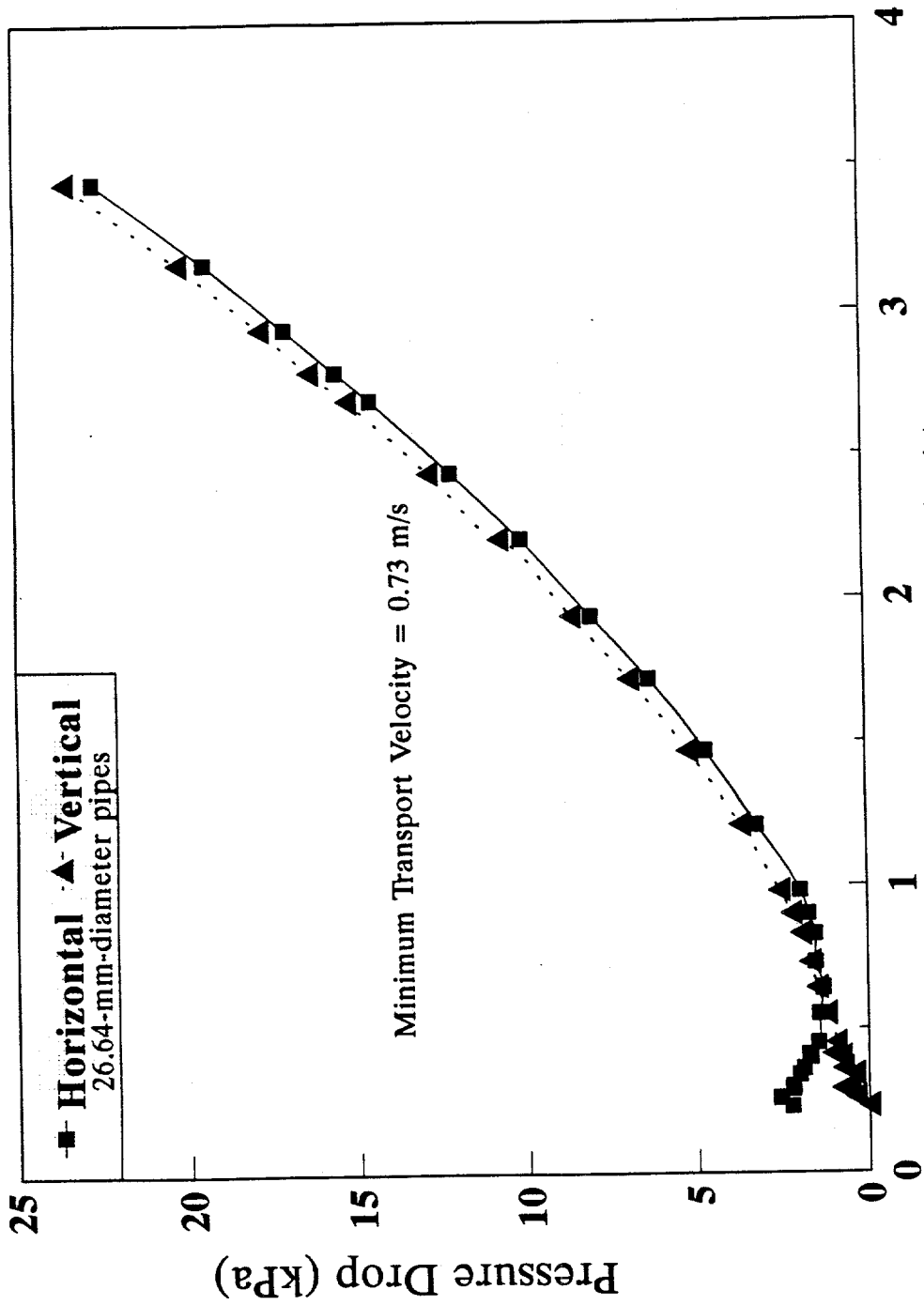

Figure 17. Pressure drop versus flow rate for run D-1.

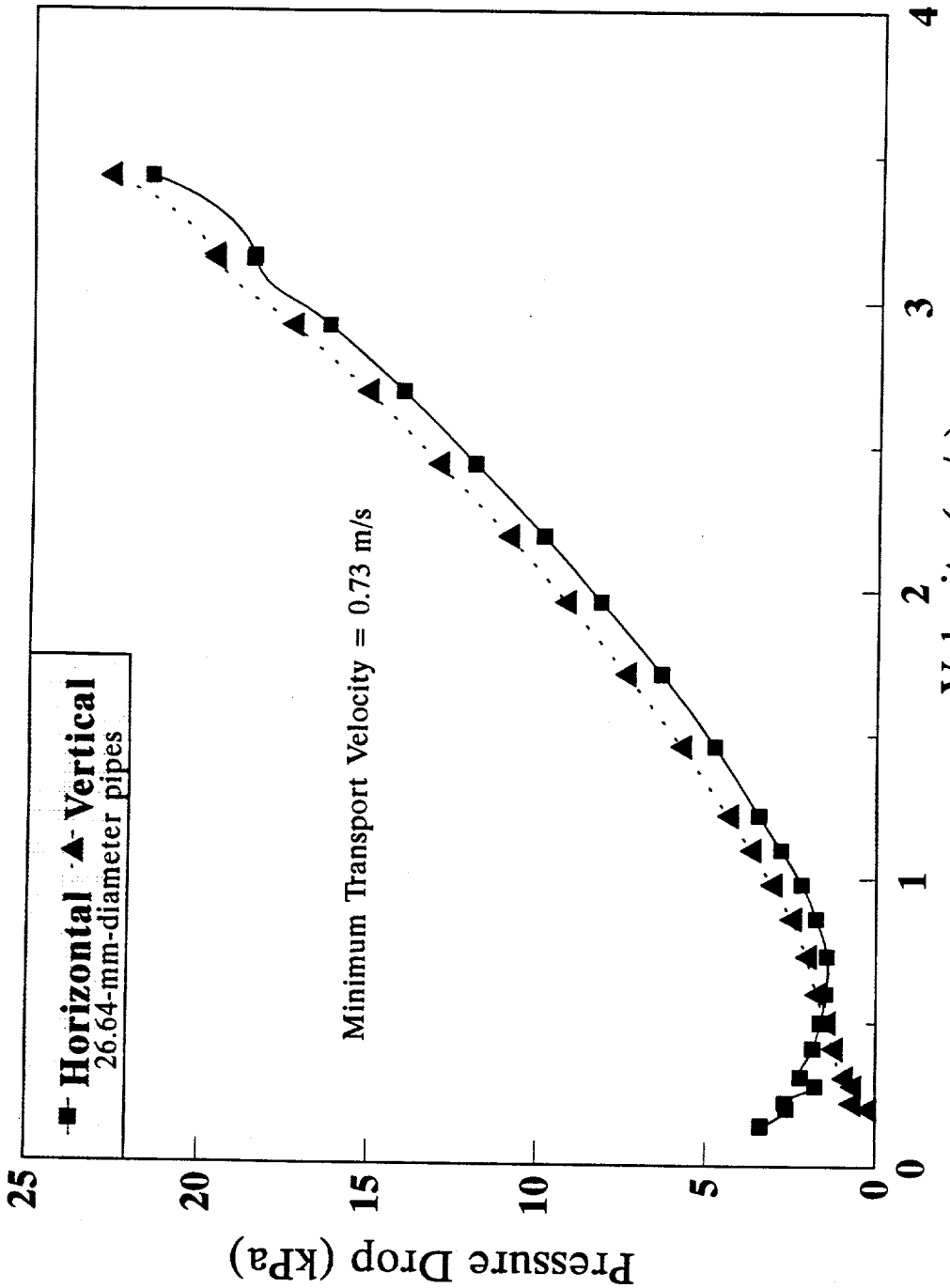

Figure 18. Pressure drop versus flow rate for run D-2.

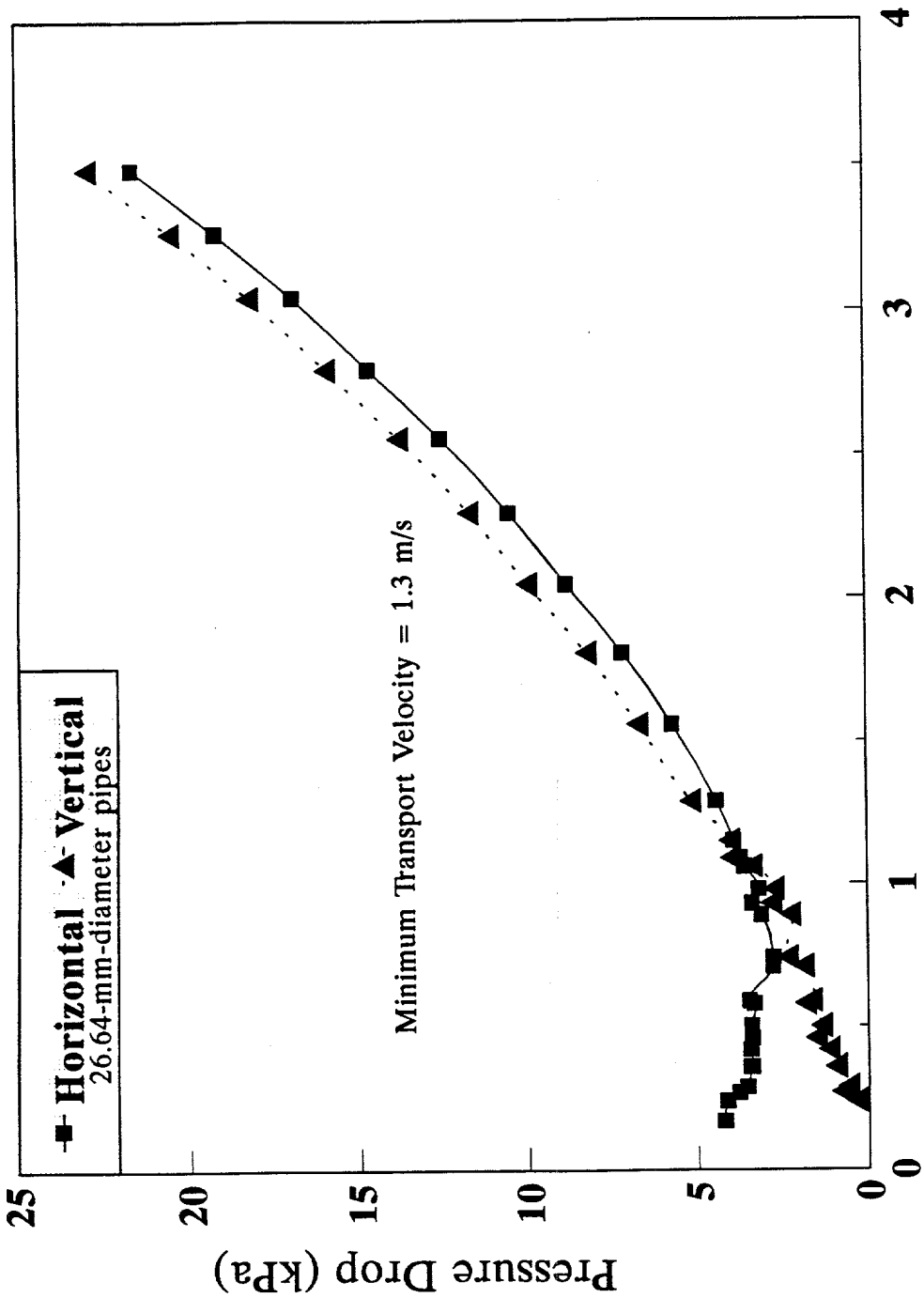

Figure 19. Pressure drop versus flow rate for run D-4.

The pressure drop data were collected by starting with a homogenous slurry (i.e., the solids were uniformly distributed); however, as the velocity decreased to a point that a stationary or sliding bed was formed, the mixture was then a heterogenous slurry. It should be noted that the minimum transport velocity is concerned with horizontal flow. The solids are more easily transported in vertical pipes since the particle fall velocities are usually much lower than the normal flow velocity [Wasp et al., 1979].

The results indicated that particles up to 500 μm would not settle out in the thick slurry except at low velocities. Run D-3 was aborted when the pump stopped because the inlet line plugged with solids while pumping the slurry that contained the nominal 500-μm particles. Normally, the minimum transport velocity occurs in the turbulent flow regime, but in the test loop, the minimum transport velocity was in the laminar flow regime. It is believed that this was because of the high concentration of suspended solids in the slurry that induced hindered settling. Therefore, the minimum transport velocity determined in this study may underpredict the actual minimum transport velocity. Section 5.3.4 provides more information about settling rates for the different concentrations tested.

5.3.4 Settling Rate Results

One-liter samples of slurry were collected from runs A-2, B-1, C-1, D-1, D-2, and D-4 for the purpose of measuring the settling rate of the solid particles. The samples were mixed well and poured in a 1-L Pyrex graduated cylinder to begin the test. The interface between the solid particles and the clear liquid was monitored versus time. Figure 20 shows settling rate curves for these samples. The curves show that the surrogate slurries settled very slowly and exhibited hindered settling due to the high concentration of solids in the slurry. Hindered settling occurs when the motion of a particle is impeded by other particles. The hindered settling

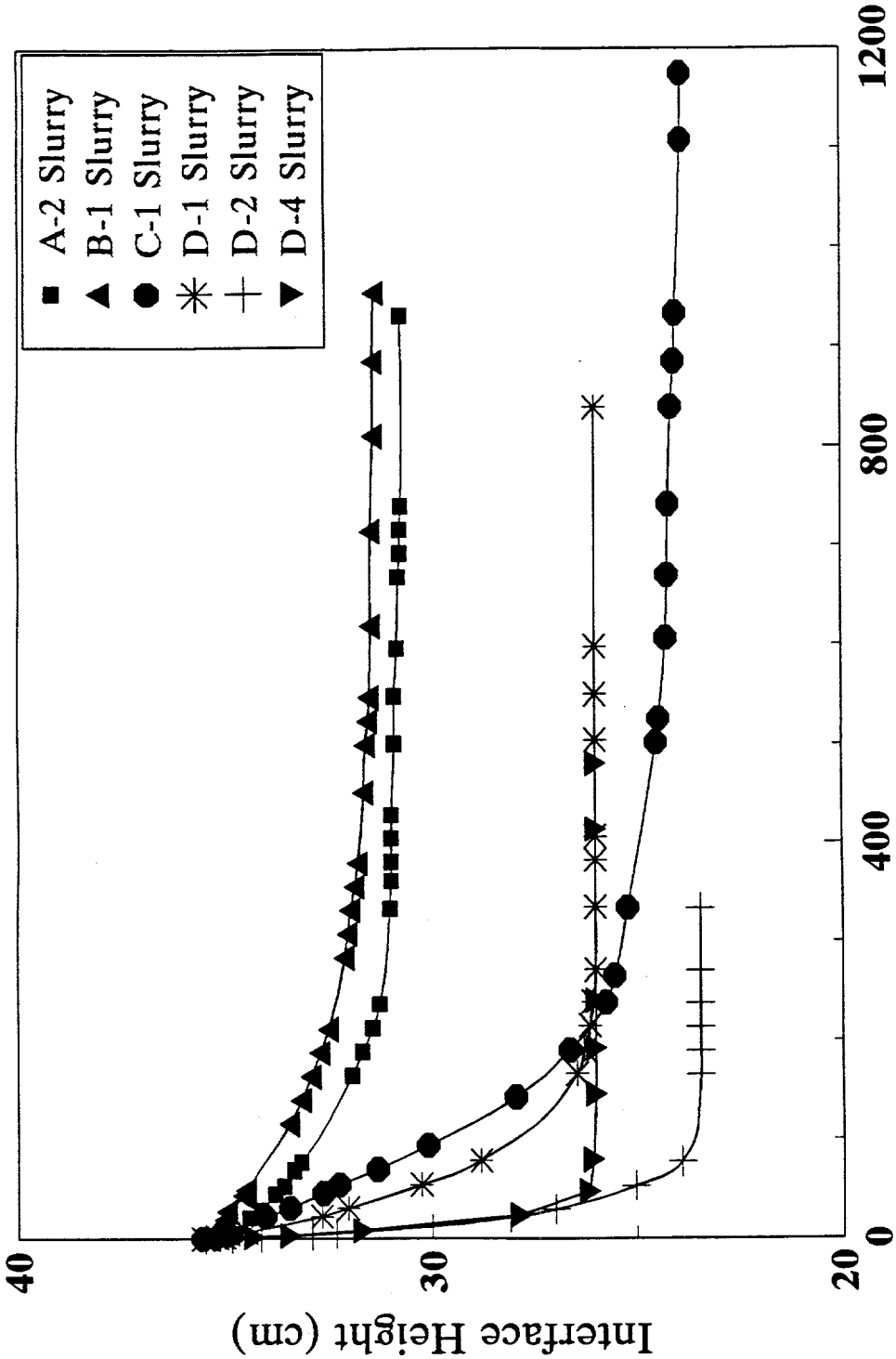

Figure 20. Settling rate curve for slurries tested in the test loop.

behavior is likely to decrease the minimum transport velocity since the solid particles remain in suspension longer.

Three dilute slurry mixtures were prepared by mixing A-2 slurry with clear supernatant. These slurry mixtures contained 0.5, 2.8, and 5.4 wt % of suspended solids. Settling rate tests were conducted with these mixtures for comparison with the undiluted samples discussed above. Settling rate curves for these slurry mixtures are shown in Figure 21. The settling rates determined for these dilute mixtures were 0.84, 0.20, and 0.094 cm/min, respectively. These dilute mixtures settled in a manner of hours rather than days as required by the concentrated samples.

5.3.5 Particle Size Analyses

Slurry samples were obtained from the test loop for determining the particle sizes of the slurries. A sample was submitted from each group (A, B, and C) for evaluating the particle size without the effect of glass spheres in the slurry. As one might expect, the surrogate slurries contained a range of particle sizes. The particle size analysis curves tended to be similar, with only minor changes in the diameter and fraction sizes. The results are shown in Figure 22 for the weight percent versus the particle diameter. A diagram that shows the cumulative weight percent versus particle size is included in Appendix H.

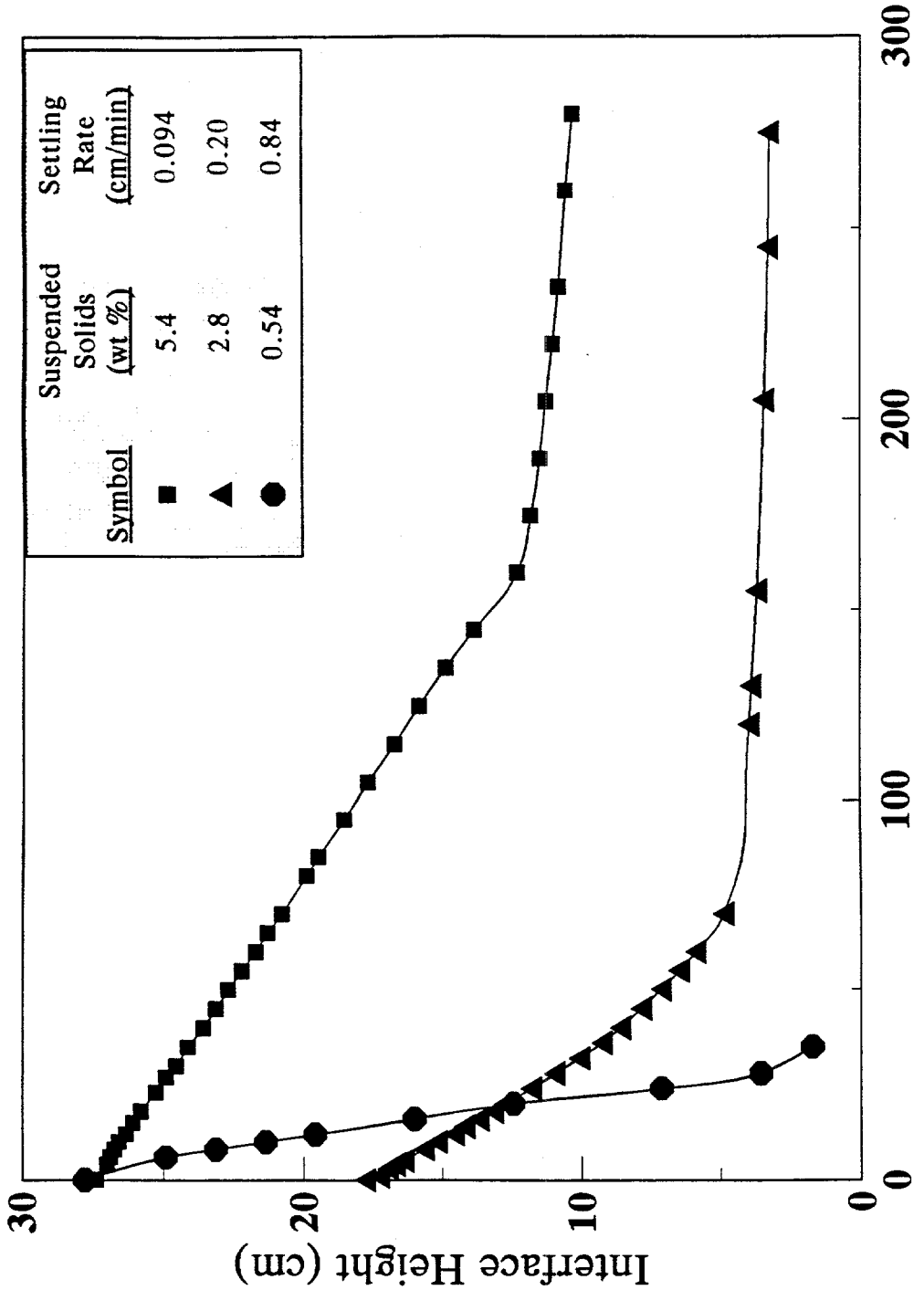

Figure 21. Settling rate curve for dilute suspended solids surrogate slurries.

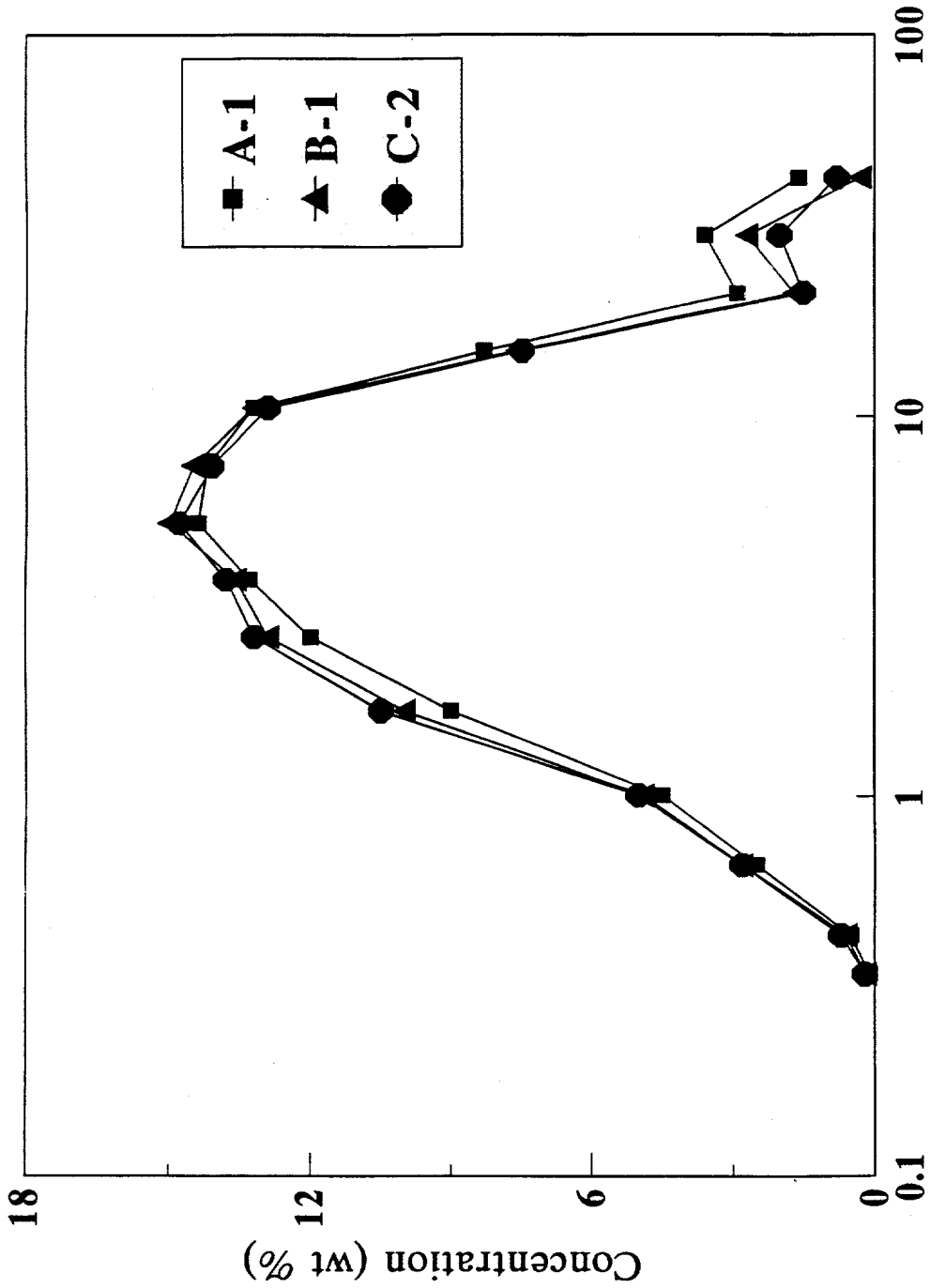

Figure 22. Particle size analysis of surrogate slurries used in the test loop.

6. CONCLUSIONS AND RECOMMENDATIONS

The objective of this study was to develop correlations for predicting the flow parameters needed for the design and operation of slurry pipeline transport systems for the radioactive waste slurry stored in the ORNL MVSTs. Nonradioactive simulated slurries with chemical compositions and rheological properties similar to the waste in the MVSTs were developed for use in this study. The rheology of a surrogate slurry of the MVSTs at ORNL was evaluated and compared with the Power Law and Bingham plastic models. Suspended solids concentrations ranging from ≈23 to 34 wt % and slurry temperatures ranging from 25 to 45°C were evaluated.

It appears that the Bingham plastic model can be used to adequately represent the rheology of the surrogate slurry based on the match of the model to the rheograms. The Bingham plastic parameters are more easily related to physical properties.

It also appears that the Power Law model could be used to adequately represent the rheology of the surrogate slurry evaluated based on the match of the model to the rheograms. The Power Law is favored because of its mathematical simplicity; however, it should be emphasized that the Power Law model should not be extrapolated beyond the experimental data.

The statistical fit of the data using the r^2 correlation factors indicated that the Bingham Plastic and Power Law models fit the data about the same. However, it can be seen from the Power Law model rheograms that the curves are diverging away from the data points at the upper shear rates. Therefore, the Bingham Plastic model is considered to represent the slurry rheology slightly better than the Power Law model.

The Bingham plastic results indicated that the plastic viscosity increased as the concentration of suspended solids increased. The results for the temperature effect showed that

there was only a slight effect on the rheology of the slurry. As the temperature increased, a slight decrease in plastic viscosity was observed; however, the yield stress results were inconsistent. The A-series of runs indicated that the yield stress increased slightly as the temperature increased, but the B- and C-series of runs indicated that the yield stress decreased slightly as the temperature increased. It may be that the higher temperature caused some chemical changes in the slurry during the A-series of runs, or the difference may be due to data scatter. The basic conclusion is that slurry temperature had little effect on the rheology.

The Power Law model results generally showed that the consistency factor increased as the concentration of suspended solids increased and the flow behavior index decreased as the concentration of suspended solids increased. The consistency factor decreased as the slurry temperature increased, and the flow behavior index appeared to increase slightly as the slurry temperature increased.

The minimum transport studies were inconclusive as to whether there would be any problems in handling slurries with large particles (≈500 μm). The experimental data indicated that the particles would remain suspended in the horizontal pipes until a low velocity was reached; however, it was shown that these slurries exhibited hindered settling. Further tests should be performed with a surrogate slurry that does not contain as many suspended solids.

The work described in this report should prove valuable in designing the transport systems for the MVST slurries. However, in addition to the tests recommended for determining the minimum transport velocity, it is recommended that more studies should be performed to support the design of the transport system for the MVST slurries. The recommended studies are discussed below.

The data obtained in this report are for pipes without joints, valves, and other items that cause pressure drop in a transport system. It is not known if the standard correlations used for

pressure drop of Newtonian fluids through pipe fittings are adequate for non-Newtonian slurries. The slurry test loop could be modified to determine the additional correlations for those items.

The test loop could also be redesigned to obtain more data about the surrogate slurry, if desired. For example, the three horizontal pipeline viscometers could be connected in series rather than parallel. This modification would mean that the slurry conditions and flow rate would be precisely the same for each viscometer; however, a bypass line should be installed around the smaller-diameter viscometers to allow the collection of data at high flow rates with the larger-diameter viscometers.

The vertical viscometer used in this study consistently showed higher pressure drops (due to friction) than the same-size horizontal viscometer for a calibration fluid and the surrogate slurry. The vertical viscometer was deemed unreliable for measuring the rheology because of the short flow-smoothing section (the first pressure tap was only 15 pipe diameters above a smooth bend). The vertical viscometer should be redesigned to reflect the space limitations. The most reasonable modification is to construct the vertical viscometer from a smaller-diameter pipe (e.g, 0.75-in. pipe rather than the 1-in. used for this report). This would allow a shorter flow-smoothing section, and permit a shorter overall length of the viscometer.

Studies in longer pipes would also be desirable. A longer distance between the pressure taps of the pipeline viscometer would allow the measurement of a higher pressure drop, which would most likely increase the accuracy of the differential pressure transmitters, particularly at low flow rates. The limitation for this option is that the overall length of the viscometer must not exceed the maximum length of available pipe.

REFERENCES CITED AND SELECTED BIBLIOGRAPHY

Baroid Drilling Fluids, Inc., 1989. "FANN® Model 35 Viscometer: Instruction Manual," Part No. 354960001EA, Baroid Drilling Fluids, Inc., Houston.

Ceo, R. N., M. B. Sears, and J. T. Shor, 1990. *Physical Characterization of Radioactive Sludges in Selected Melton Valley and Evaporator Facility Storage Tanks.* ORNL/TM-11653. Oak Ridge National Laboratory.

Darby, R., R. Mun, and D. V. Boger, 1992. "Predict Friction Loss in Slurry Pipes." *Chemical Engineering*, September.

Dodge, D. W. and A. B. Metzner, 1959. "Turbulent Flow of Non-Newtonian Systems." *A.I.Ch.E. Journal*, Vol. 5, No. 2.

Govier, G. W., and K. Aziz, 1972. *The Flow of Complex Mixtures in Pipes.* Van Nostrand Reinhold, New York.

Hanks, R. W., 1986. "Principles of Slurry Pipeline Hydraulics." Chapter 6. In *Encyclopedia of Fluid Mechanics*, Vol. 5, N. P. Cheremisinoff (ed.), Gulf Publishing Co, Houston.

Hanks, R. W., 1992. "Yield Power Law Pipeline Design Program." Richard W. Hanks Associates, Inc., Orem, Utah.

Hanks, R. W., and B. H. Dadia, 1971. "Theoretical Analysis of the Turbulent Flow of Non-Newtonian Slurries in Pipes." *AIChE Journal*, Vol. 17, No. 3.

Hanks, R. W., and B. L. Ricks, 1975. "Transitional and Turbulent Pipeflow of Pseudoplastic Fluids." *Journal of Hydronautics*, Vol. 9, No. 1.

Hedström, B. O. A., 1952. "Flow of Plastics Materials in Pipes." *Industrial and Engineering Chemistry*, Vol. 44, No. 3.

Heywood, N. I., 1991. "Pipeline Design for Non-Settling Slurries." Chapter 7. In N. P. Brown and N. I. Heywood (eds.), *Slurry Handling Design of Solid-Liquid Systems.* Elsevier Science Publishers, Essex, England.

Heywood, N. I., 1991. "Rheological Characterisation of Non-settling Slurries." Chapter 4. In N. P. Brown and N. I. Heywood (eds.), *Slurry Handling Design of Solid-Liquid Systems.* Elsevier Science Publishers, Essex, England.

International Critical Tables of Numerical Data, Physics, Chemistry and Technology, 1929. Vol. 5, McGraw-Hill, New York.

Jacobs, B. E. A., 1991. *Design of Slurry Transport Systems.* Elsevier Science Publishers, Essex, England.

McCabe, W. L., and J. C. Smith, 1976. *Unit Operations of Chemical Engineering.* 3rd ed. McGraw-Hill Inc., New York.

Metzner, A. B., and J. C. Reed, 1955. "Flow of Non-Newtonian Fluids—Correlation of the Laminar, Transition, and Turbulent-flow Regions." *A.I.Ch.E. Journal*, Vol. 1, No. 4.

Rose, C., and G. E. Vass, 1993. "Consider the Attractions of Magnetic Flowmeters." *Chemical Engineering Progress*, Vol. 89, No. 12.

Ryan, N. W., and M. M. Johnson, 1959. "Transition from Laminar to Turbulent Flow in Pipes." *A.I.Ch.E. Journal*, Vol. 5, No. 4.

Sears, M. B., et al., 1990. *Sampling and Analysis of Radioactive Liquid Wastes and Sludges in the Melton Valley and Evaporator Facility Storage Tanks at ORNL.* ORNL/TM-11652. Oak Ridge National Laboratory.

Skelland, A. H. P., 1967. *Non-Newtonian Flow and Heat Transfer.* John Wiley & Sons, Inc., New York.

Wasp, E. J., J. P. Kenny, and R. L. Gandhi, 1979. *Solid-Liquid Flow Slurry Pipeline Transportation.* Gulf Publishing Co., Houston.

Wilson, K. C., G. R. Addie, and R. Clift, 1992. *Slurry Transport Using Centrifugal Pumps.* Elsevier Science Publishers, Essex, England.

Youngblood, E. L., Jr., et al., 1994. *Fluid Dynamic Demonstrations for Waste Retrieval and Treatment.* ORNL/TM-12660. Oak Ridge National Laboratory.

APPENDIX A

SLURRY PREPARATION AND CEO METHODS

RECIPE FOR 190-L BATCH OF MVST SURROGATE SLURRY

This is a recipe for preparing Melton Valley Storage Tank (MVST) surrogate slurry. It forms the iron, aluminum, and calcium hydroxide compounds from the reaction of sodium hydroxide with the nitrate form of the metal ion involved. For example, the reaction of calcium nitrate with sodium hydroxide yields calcium hydroxide and sodium nitrate. Please be aware that heat may be generated during the mixing process. Magnesium hydroxide is not prepared similarly because of difficulty in obtaining magnesium nitrate.

1. Obtain a clean 55-gal stainless steel drum. Add 38 L (37.92 kg) of water to the drum. Initiate stirring with an agitator and continue stirring throughout the procedure.

2. Obtain 16.86 kg of sodium hydroxide (NaOH) flakes or pellets. Slowly add the NaOH to the agitated water. Be aware that adding NaOH to water will cause heat to be generated. It is recommended that you control the temperature by adjusting the addition rate. Proceed to the next step when the NaOH is dissolved.

3. In another clean container, add 1.25 kg of iron nitrate [$Fe(NO_3)_3 \cdot 9H_2O$]. Dissolve the iron nitrate in 1.9 L (1.9 kg) of water. **Slowly** add the solution to the 55-gal drum when the iron nitrate is dissolved. It is important to add the solution slowly to enhance the formation of small particles of $Fe(OH)_3$.

4. Add 41.90 kg of calcium nitrate [$Ca(NO_3)_2 \cdot 4H_2O$] to another clean container. Dissolve the compound in 19 L (18.96 kg) of water. **Slowly** add the solution to the 55-gal drum when the calcium nitrate is dissolved. It is important to add the solution slowly to enhance the formation of small particles of $Ca(OH)_2$.

4. Add 7.10 kg of aluminum nitrate [$Al(NO_3)_3 \cdot 9H_2O$] to another clean container. Dissolve the compound in 4.73 L (4.72 kg) of water. **Slowly** add the solution to the 55-gal drum when the aluminum nitrate is dissolved. It is important to add the solution slowly to enhance the formation of small particles of $Al(OH)_3$.

5. In a separate container, dissolve 0.89 kg sodium chloride (NaCl), 4.01 kg sodium carbonate (Na_2CO_3), 9.08 kg potassium nitrate (KNO_3), and 21.12 kg sodium nitrate ($NaNO_3$) in 38 L (37.92 kg) of water. Because of the size of this batch, you may want to break this step in two steps. Note that the dissolution of sodium nitrate is an endothermic reaction. Some gentle heating may be required to assist the compound to dissolve. Add the solution to the 55-gal drum when the compounds are dissolved.

6. Obtain 37.06 kg of calcium carbonate ($CaCO_3$) and 8.08 kg of magnesium hydroxide [$Mg(OH)_2$]. Slowly add these compounds to the 55-gal drum.

7. Obtain 0.076 kg of sodium hydroxide (NaOH) and dissolve it in 0.15 L of water. Please note that this will form 12.7 *N* sodium hydroxide. When the sodium hydroxide is dissolved, add 1.59 kg of silicic acid (H_2SiO_3) to the sodium hydroxide. This should form a solution of sodium silicate. Add this solution to the 55-gal drum to complete the additions to the surrogate slurry. Continue mixing until the slurry is homogeneous.

CEO METHOD

Procedure Used to Determine Density and Solids Values

Reference: R. N. Ceo et al., *Physical Characterization of Radioactive Sludges in Selected Melton Valley and Evaporator Facility Storage Tanks*, ORNL/TM-11653, Oak Ridge National Laboratory, October 1990.

Two portions of each sludge sample were required for a set of measurements. The first portion (about 5 g) was placed in a tared, graduated 15-mL centrifuge tube and weighed. The sludge was centrifuged for 15 min at high speed before reading the total volume and calculating the bulk density:

$$\text{Bulk density} = \frac{\text{Wet mass 1}}{\text{Wet volume 1}} .$$

The separated interstitial liquid was drawn off from the centrifuged sample using a transfer pipet, then filtered through a 0.45-μm filter. One milliliter of the filtered solution was weighed to determine the interstitial liquid density:

$$\text{Liquid density} = \frac{\text{Solution mass}}{\text{1 mL}} .$$

A second portion (about 1 g) of the original sludge was taken. This portion was placed into a tared 10-mL beaker and weighed. The sludge was dried at 110 ± 5°C for 16 ± 1 h, then reweighed to determine the total solids content and loss of water and other volatiles:

$$\text{Total solids} = \frac{\text{Dry mass 2}}{\text{Wet mass 2}} , \text{ and}$$

$$\text{Water loss (sludge)} = \text{Wet mass 2} - \text{Dry mass 2} .$$

The dissolved solids content was calculated from the solution residue mass, the water losses from sludge and solution, and the wet sludge mass:

$$\text{Dissolved solids} = \frac{\text{Residue mass}}{\text{Wet mass 2}} \times \frac{\text{Water loss (sludge)}}{\text{Water loss (1 mL liquid)}} .$$

The mass of interstitial liquid actually present in the second sludge portion is calculated from the liquid density and the ratio of water lost in drying the sludge to that lost in drying the liquid:

$$\text{Liquid mass} = \text{Liquid density} \times \frac{\text{Water loss (sludge)}}{\text{Water loss (1 mL liquid)}} .$$

The undissolved solids content was calculated by difference, as follows:

$$\text{Undissolved solids} = \text{Total solids} - \text{Dissolved solids} .$$

The undissolved solids density was also calculated as the ratio of differences in mass and volume:

$$\text{Floc density} = \frac{\text{Wet mass 2} - \text{Liquid mass}}{\frac{\text{Wet mass 2}}{\text{Bulk density}} - \frac{\text{Water loss (sludge)}}{\text{Water loss (1 mL liquid)}}} .$$

APPENDIX B

VENDOR INFORMATION SHEETS FOR THE GLASS SPHERES

JAYGO INCORPORATED 40 Whitney Road • Mahwah, NJ 07430 • 201/848-0200 • Fax No.: 201/891-1174

PROPERTIES OF DRAGONITE GRINDING MEDIA

Dragonite Grinding Media - Lead Free	
Si02 (Silica)	67%
Al203 (Aluminum Oxide)	1%
K20 (Potassium Oxide)	7%
Ba0 (Barium Oxide)	6%
B203 (Boric Oxide)	2%
Ca0 (Lime)	5%
Na20 (Soda)	10%
Mg0 (Magnesium Oxide)	1%

Properties	Units	
Specific Gravity	2.55 approx.	
Apparent weight according to size	Kg/Litre	1.4 - 1.6 approx.
Transformation temperature	°C	424
Modulus of Elasticity	Kp/mm2	6500
Modulus of Rigidity	Kp/mm2	2560
Hardness Rockwell according to standard	D/N 50103	47

All of the above data is approximate and will vary slightly

Figure B-1. Physical properties of glass spheres.

JAYGO INCORPORATED 40 Whitney Road • Mahwah, NJ 07430 • 201/848-0200 • Fax No.: 201/891-1174

SIZE SPECIFICATION SHEET FOR DRAGONITE GRINDING MEDIA

Code No.	Quality		Size Tolerance	
Art. PC	Unleaded Only	= ca.	1 -	20 Micron
Art. 31/20	Leaded or Unleaded	= ca.	1 -	60 Micron
Art. 31/18	" " "	= ca.	45 -	70 Micron
Art. 31/15	" " "	= ca.	55 -	95 Micron
Art. 31/14 - 0.09 mm	" " "	= ca.	80 -	110 Micron
Art. 31/13 - 0.11 mm	" " "	= ca.	90 -	130 Micron
Art. 31/12 - 0.15 mm	" " "	= ca.	110 -	180 Micron
Art. 31/11 - 0.2 mm	" " "	= ca.	160 -	250 Micron
Art. 31/10 - 0.3 mm	" " "	= ca.	230 -	320 Micron
Art. 31/9 - 0.4 mm	" " "	= ca.	290 -	420 Micron
Art. 31/8 - 0.5 mm	" " "	= ca.	400 -	520 Micron
Art. 31/7 - 0.6 mm	" " "	= ca.	490 -	700 Micron
Art. 31/5 - 0.75 mm	" " "	= ca.	650 -	900 Micron
Art. 31/4 - 1.0 mm	" " "	= ca.	850 -	1230 Micron
Art. 1.0 mm Special	Leaded Only	= ca.	990 -	1250 Micron
Art. 31/3 - 1.3 mm	Leaded or Unleaded	= ca.	1180 -	1400 Micron
ca. 1.5 mm	" " "	= ca.	1.4 mm -	1.6 mm
ca. 2.0 mm	" " "	= ca.	1.5 mm -	2.5 mm
ca. 3.0 mm	" " "	= ca.	2.5 mm -	3.5 mm
ca. 4.0 mm	" " "	= ca.	3.5 mm -	4.5 mm
ca. 5.0 mm	" " "	= ca.	4.5 mm -	5.5 mm
ca. 6.0 mm	" " "	= ca.	5.5 mm -	6.5 mm
ca. 7.0 mm	" " "	= ca.	6.5 mm -	7.5 mm
and up ...				

Figure B-2. Size specification sheet for glass spheres.

APPENDIX C

GRAPHS OF PRESSURE DROP VERSUS FLOW RATE

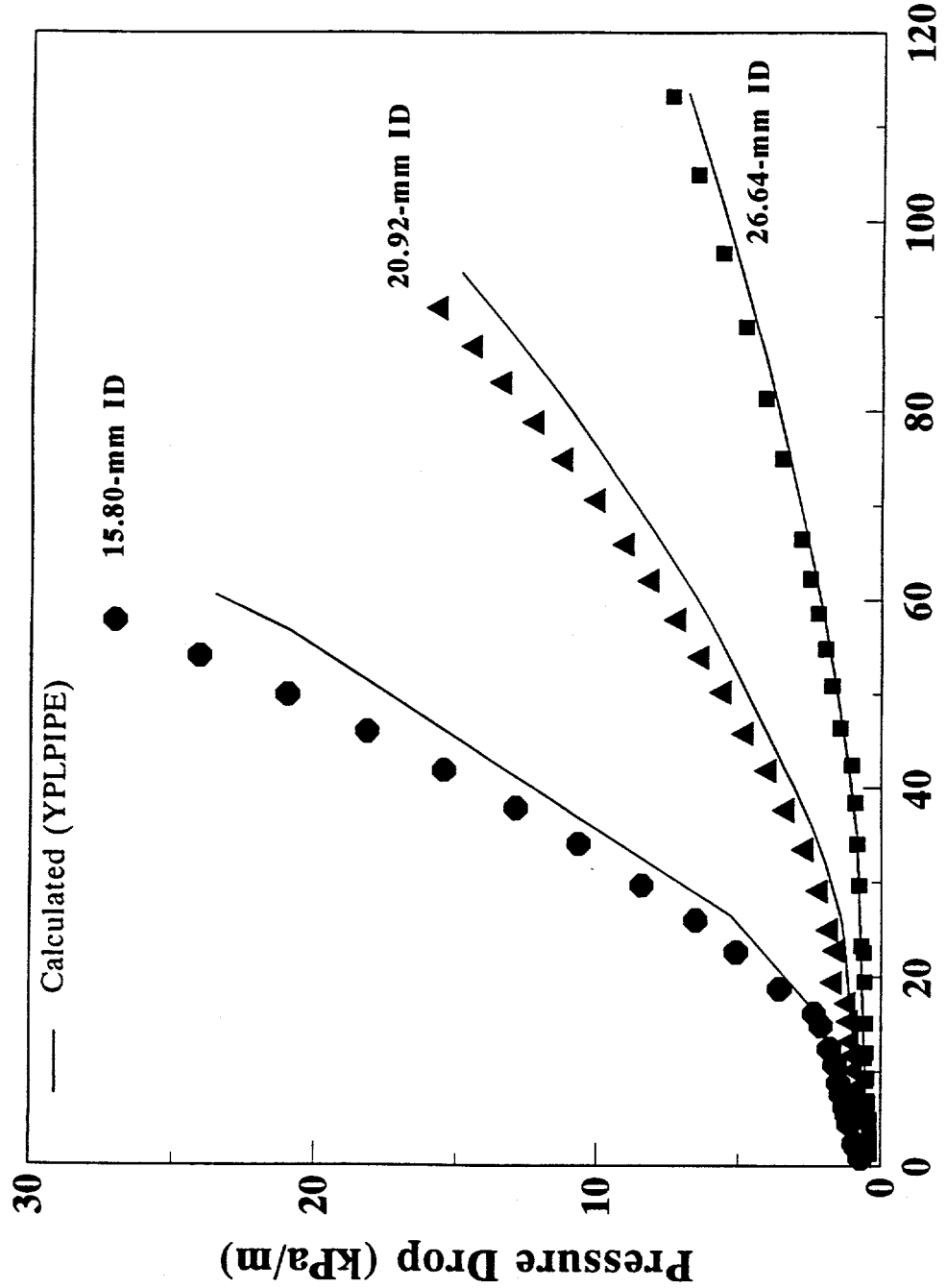

Figure C-1. Pressure drop versus flow rate for run A-1.

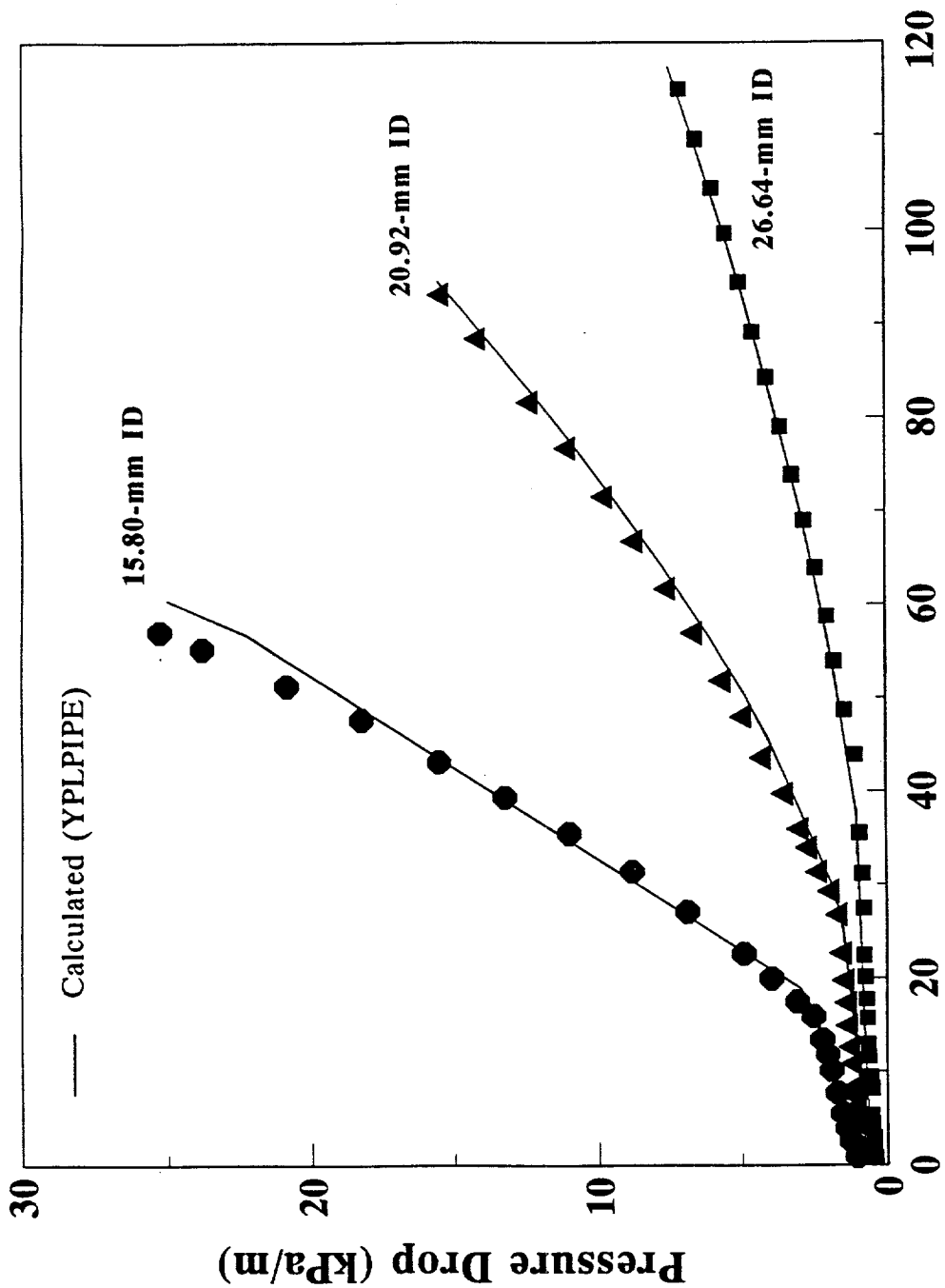

Figure C-2. Pressure drop versus flow rate for run A-2.

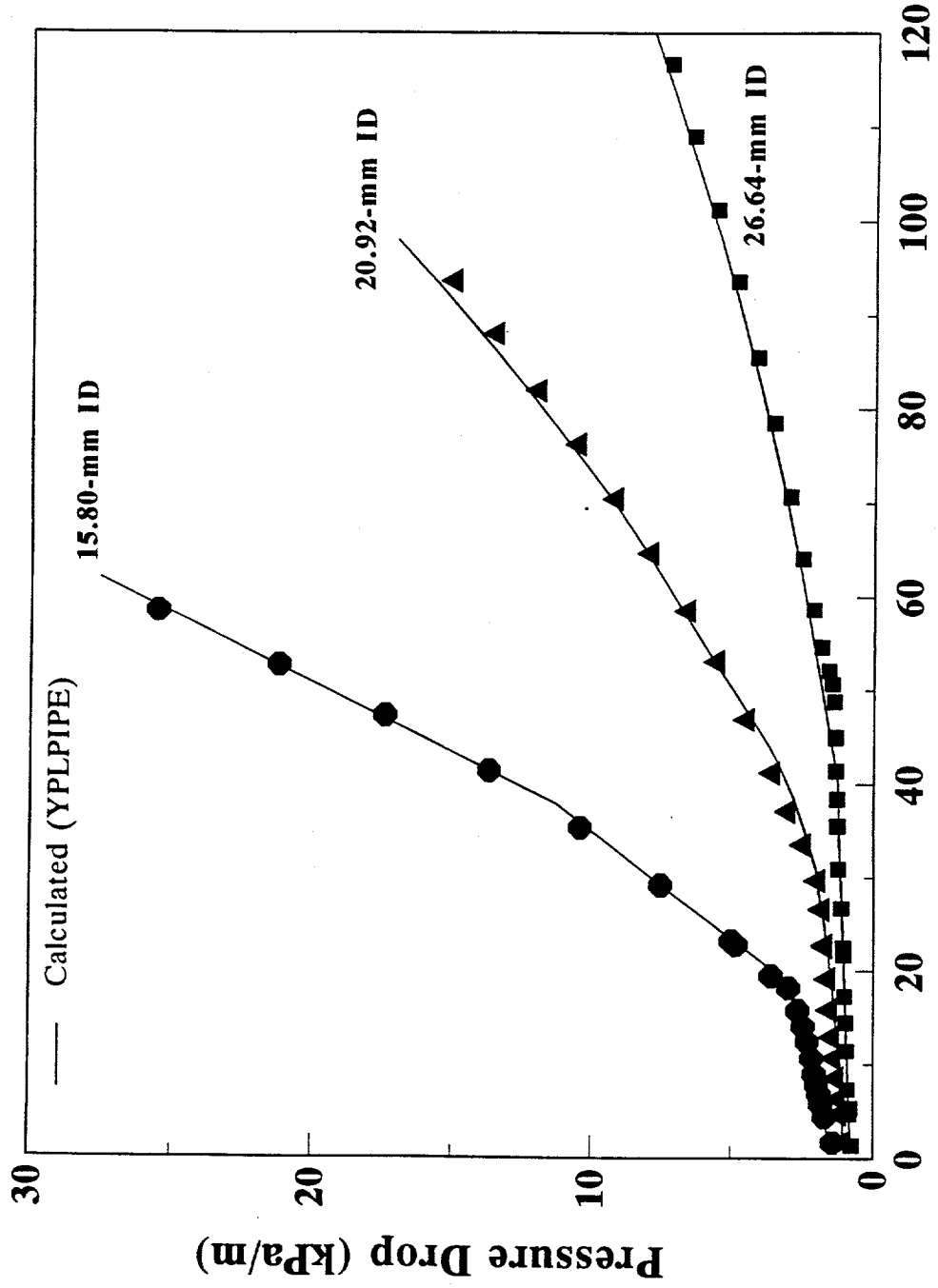

Figure C-3. Pressure drop versus flow rate for run A-3.

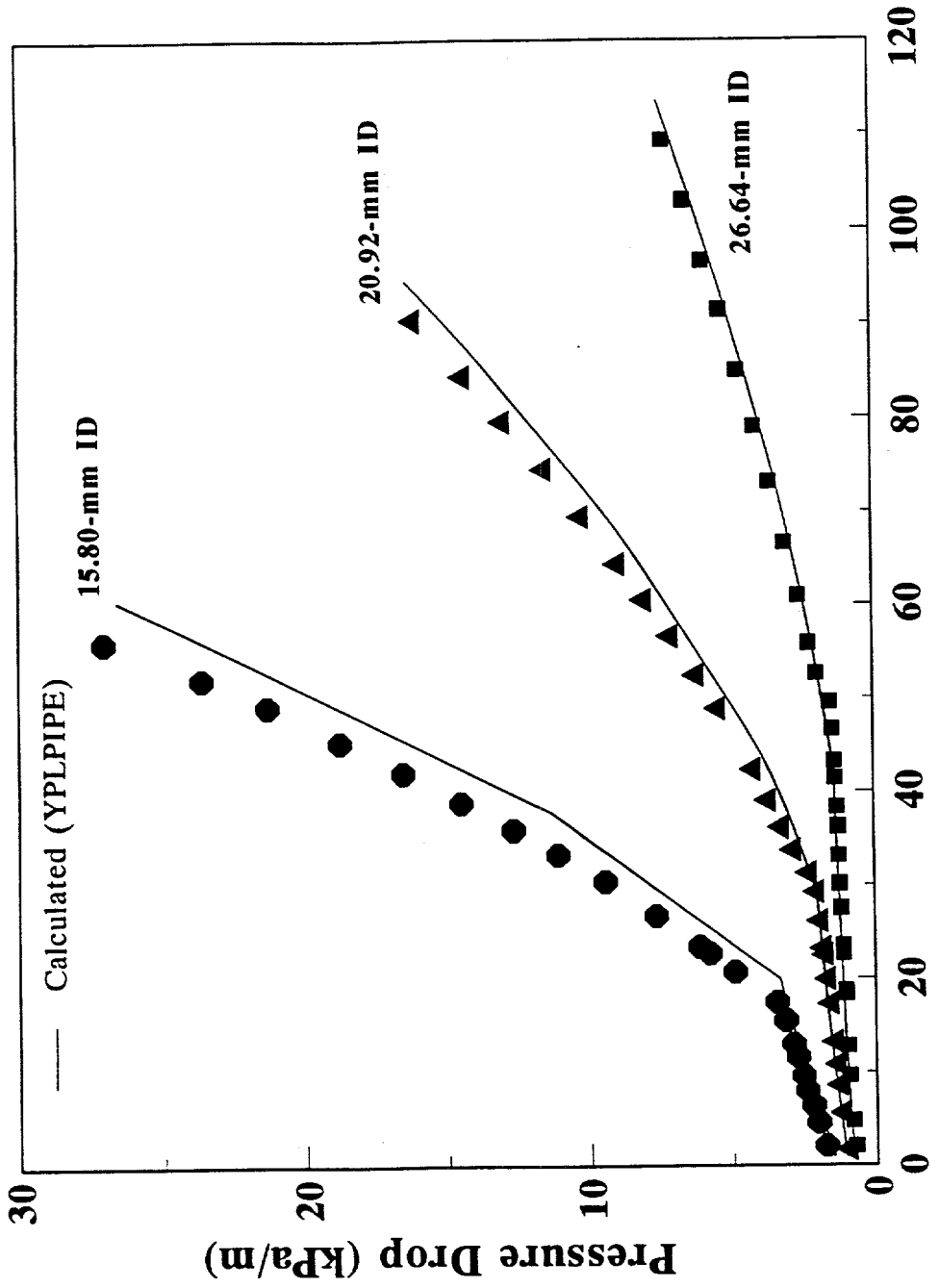

Figure C-4. Pressure drop versus flow rate for run A-4.

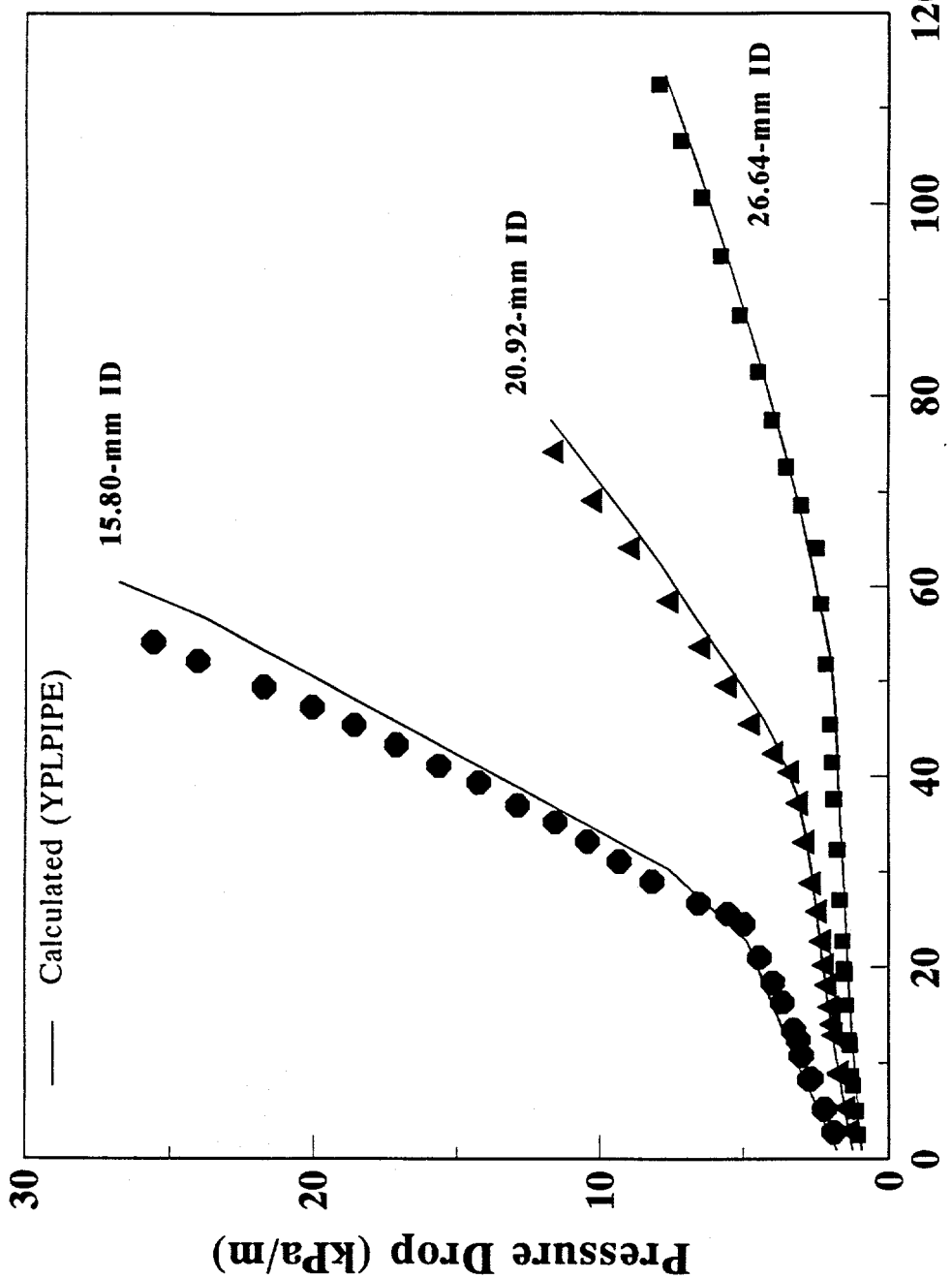

Figure C-5. Pressure drop versus flow rate for run B-1.

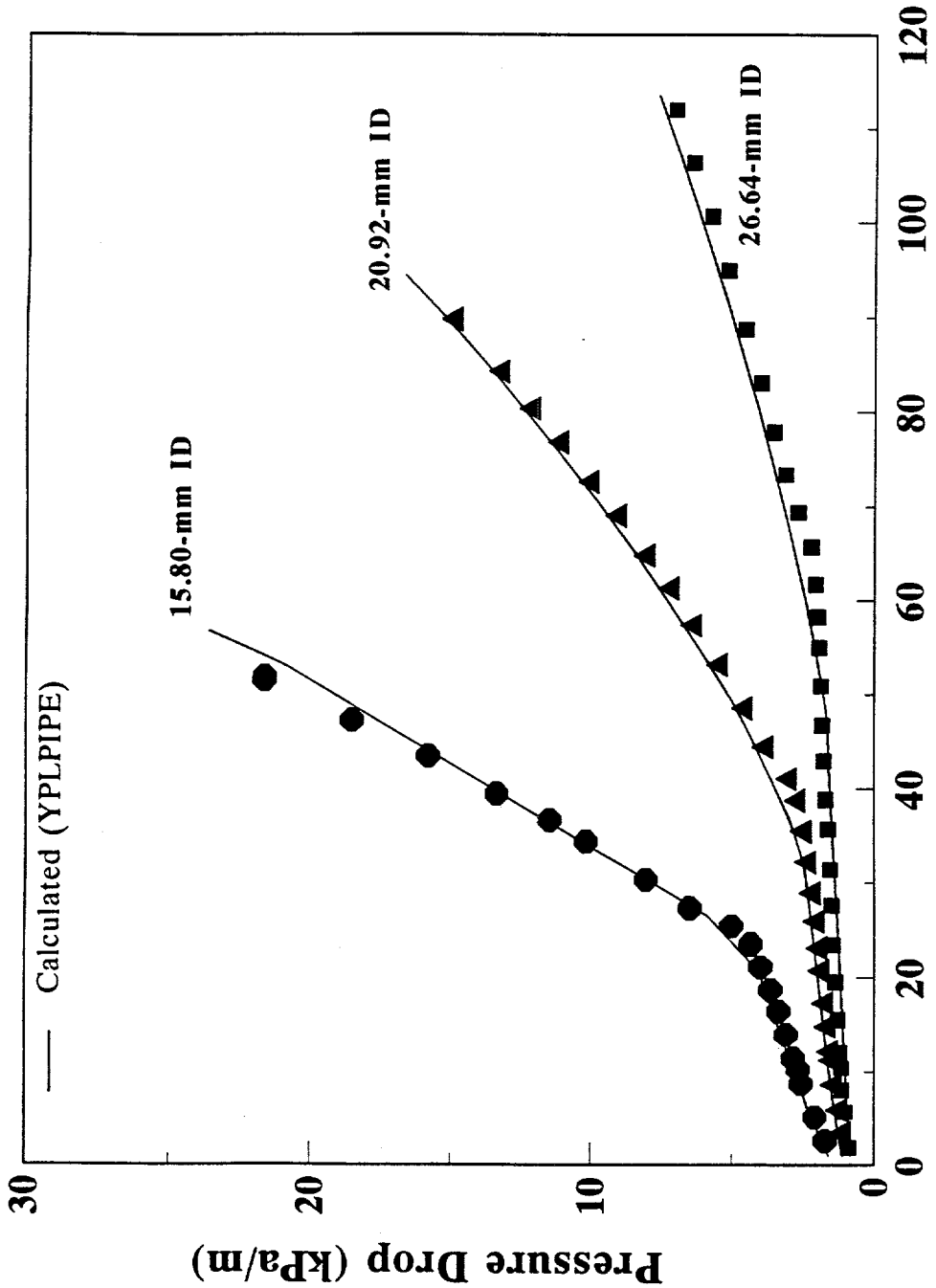

Figure C-6. Pressure drop versus flow rate for run B-2.

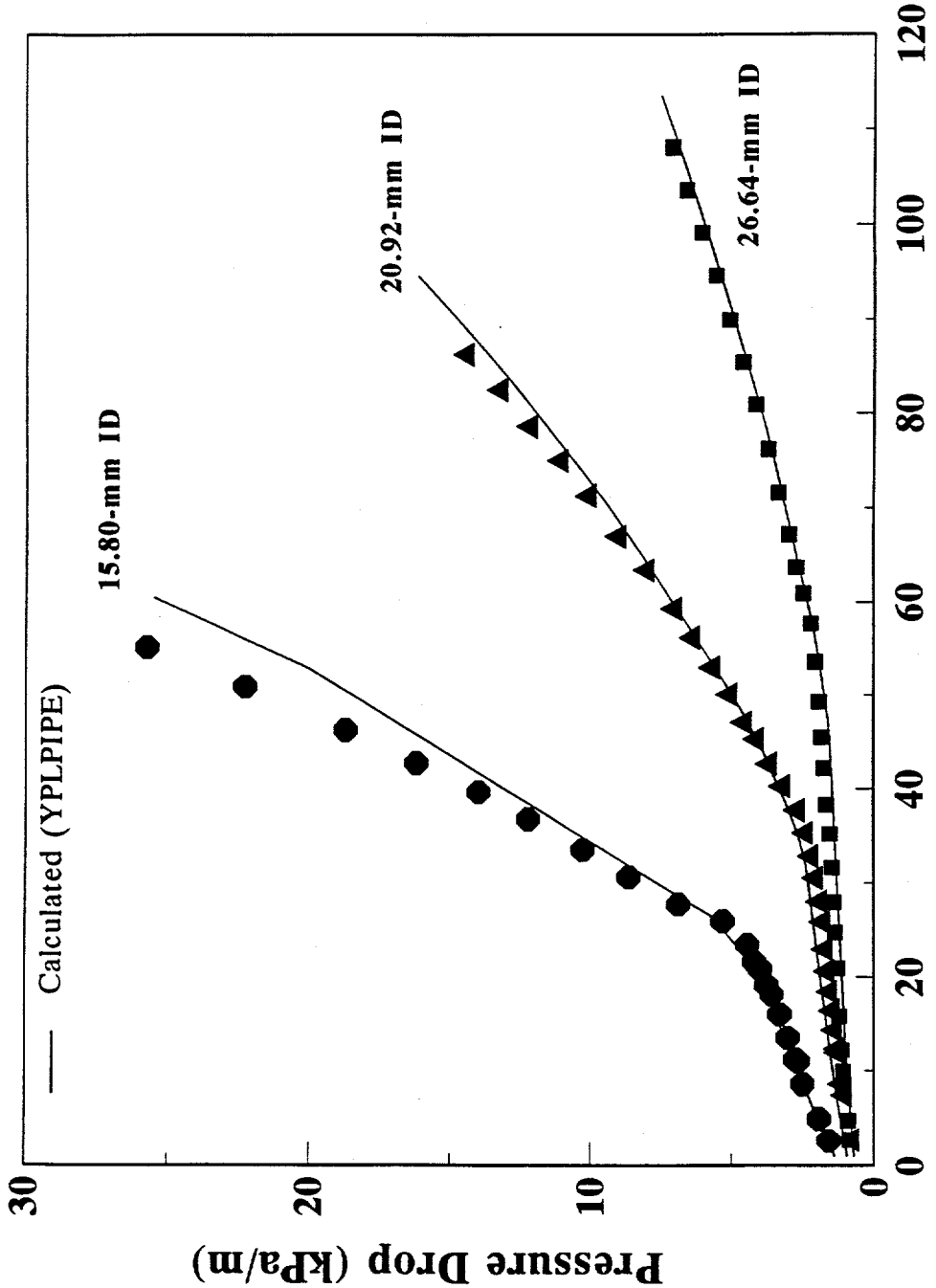

Figure C-7. Pressure drop versus flow rate for run B-3.

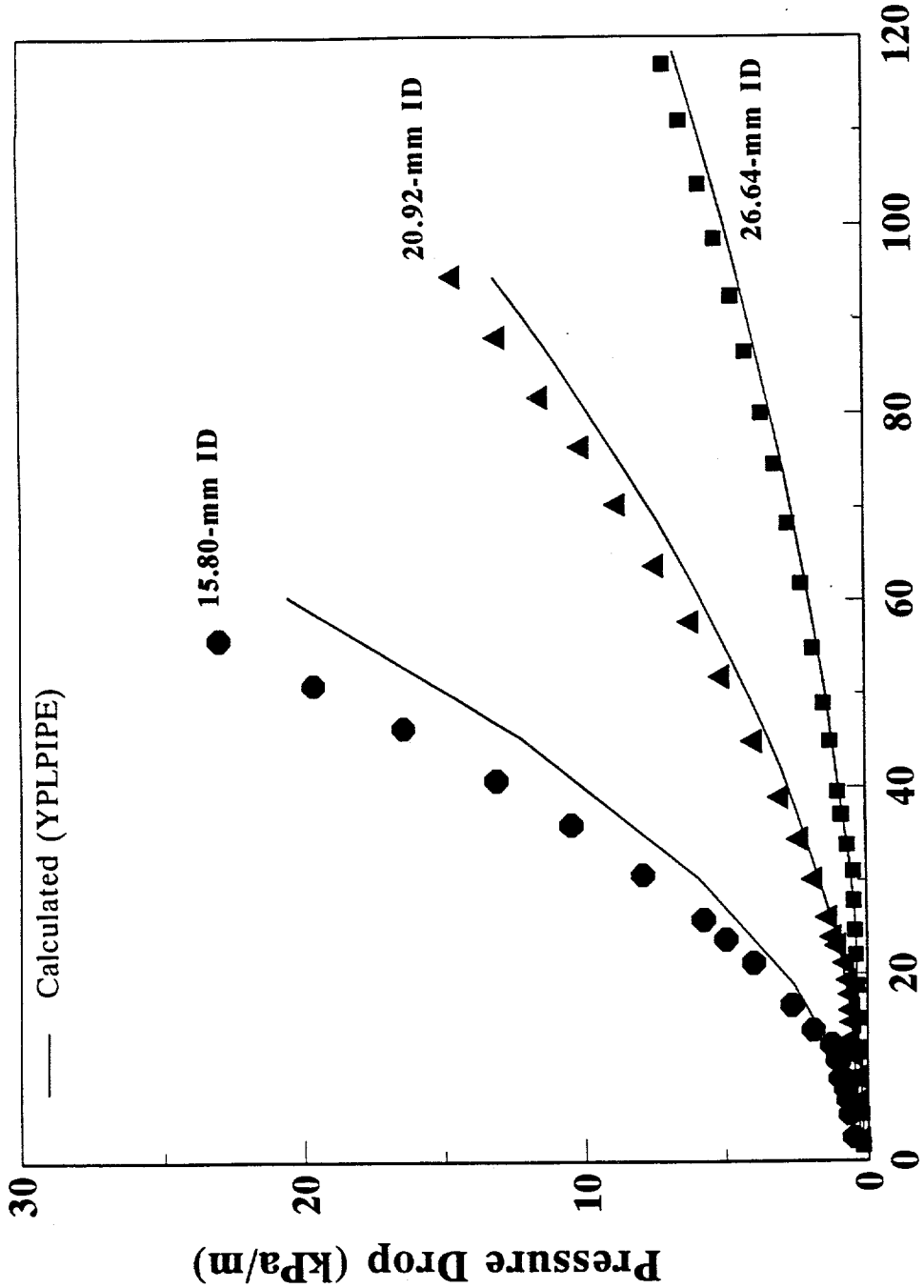

Figure C-8. Pressure drop versus flow rate for run C-1.

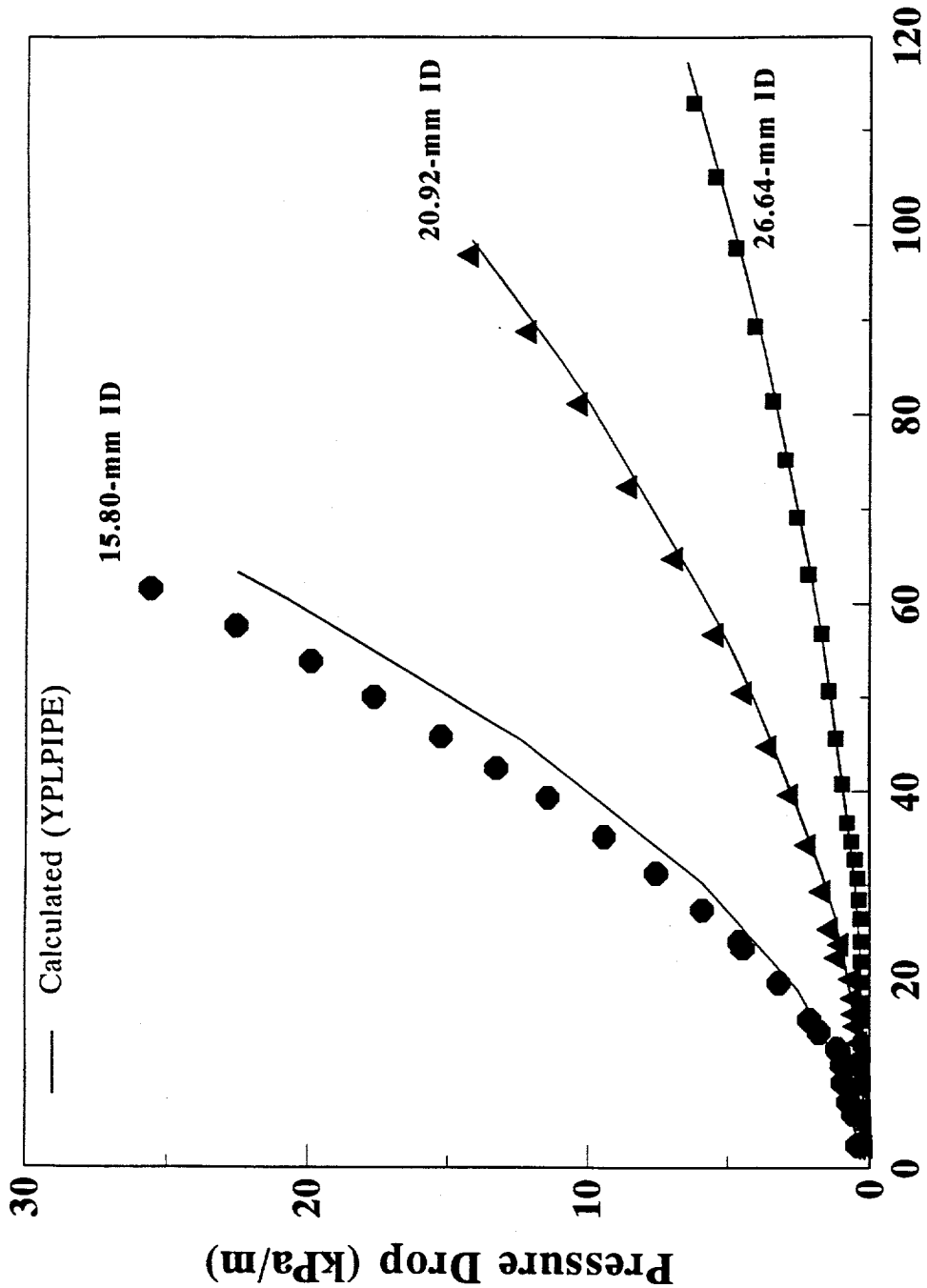

Figure C-9. Pressure drop versus flow rate for run C-2.

APPENDIX D

RHEOGRAMS FOR THE BINGHAM PLASTIC MODEL

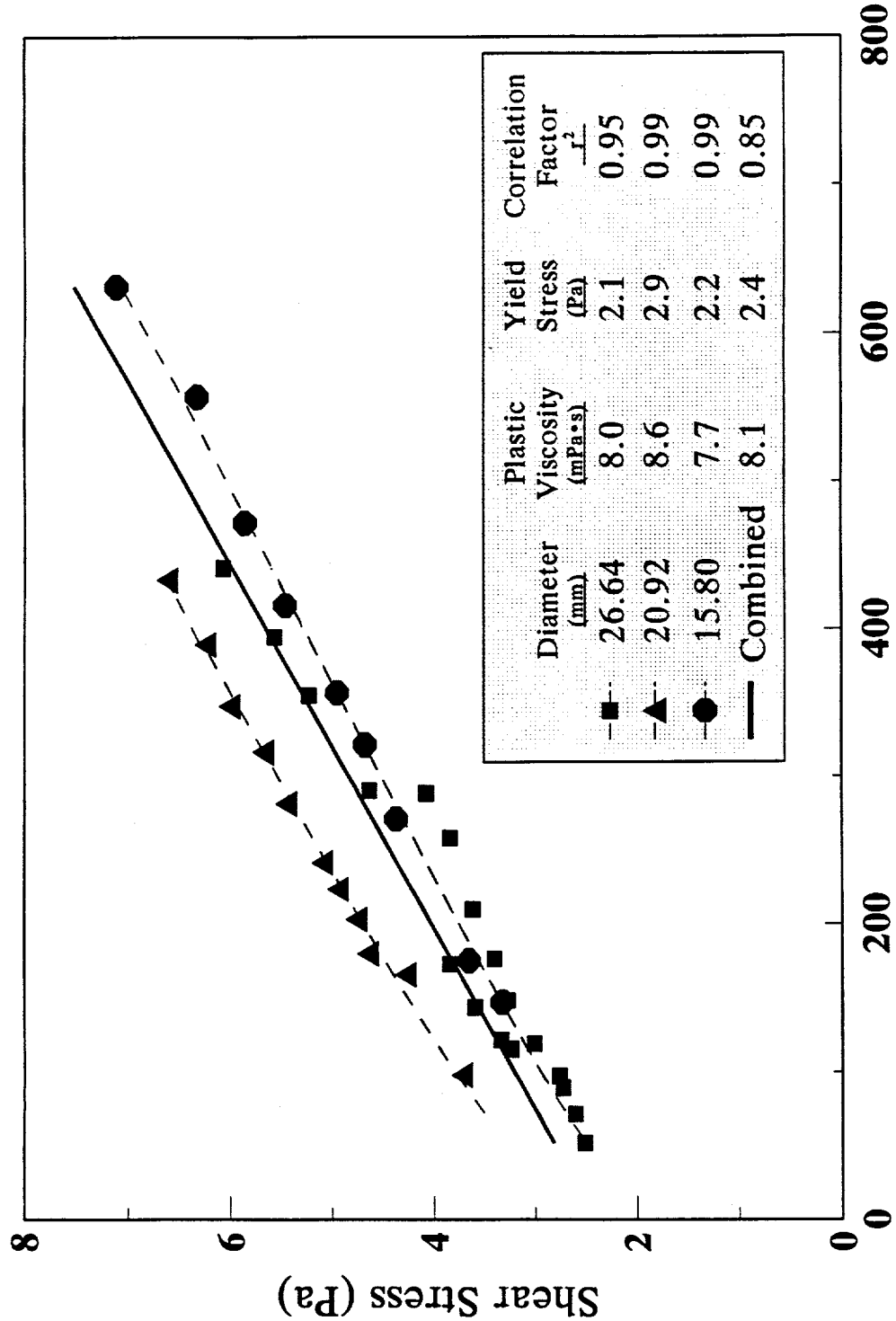

Figure D-1. Shear stress versus shear rate for run A-1 (Bingham plastic model).

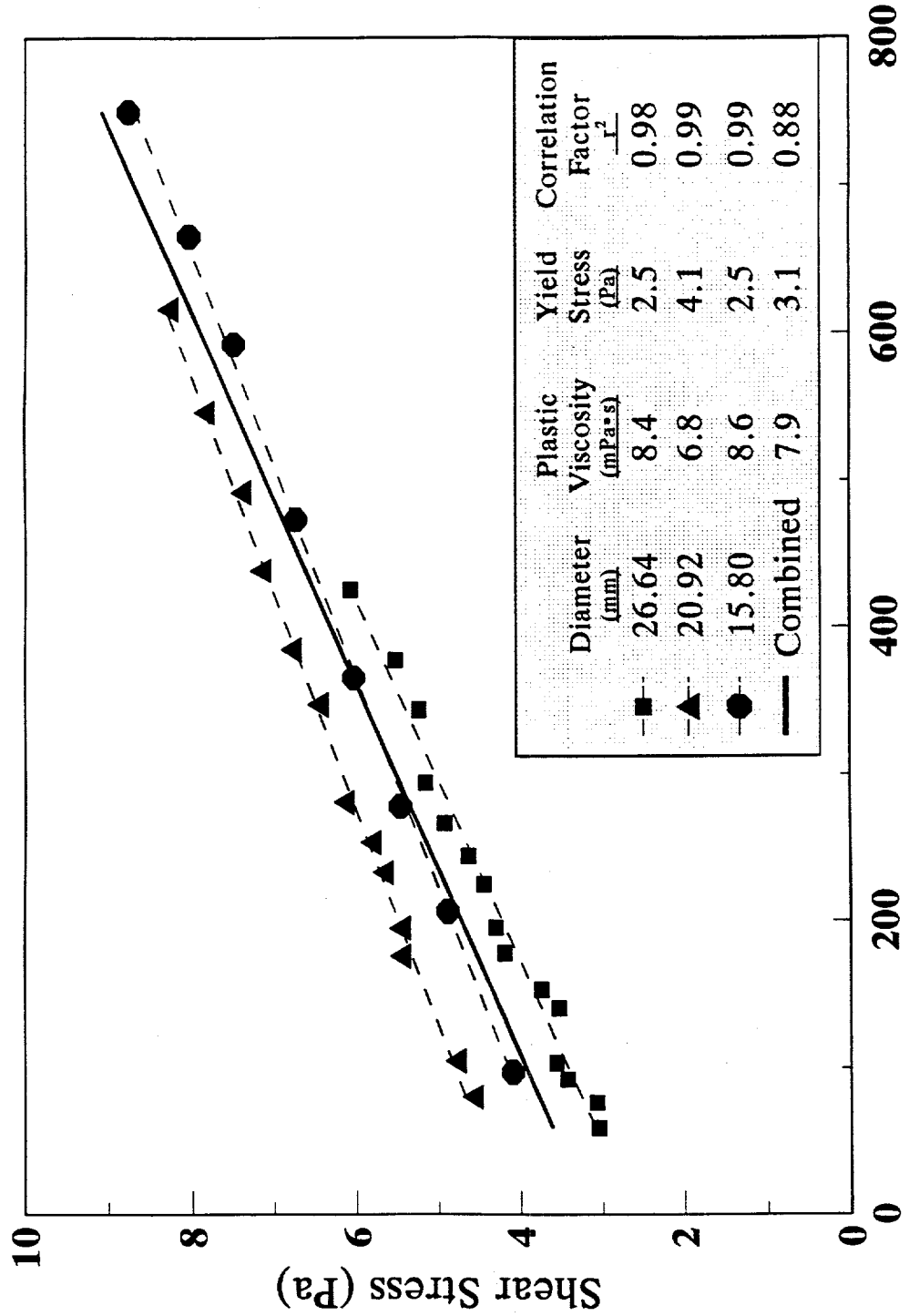

Figure D-2. Shear stress versus shear rate for run A-2 (Bingham plastic model).

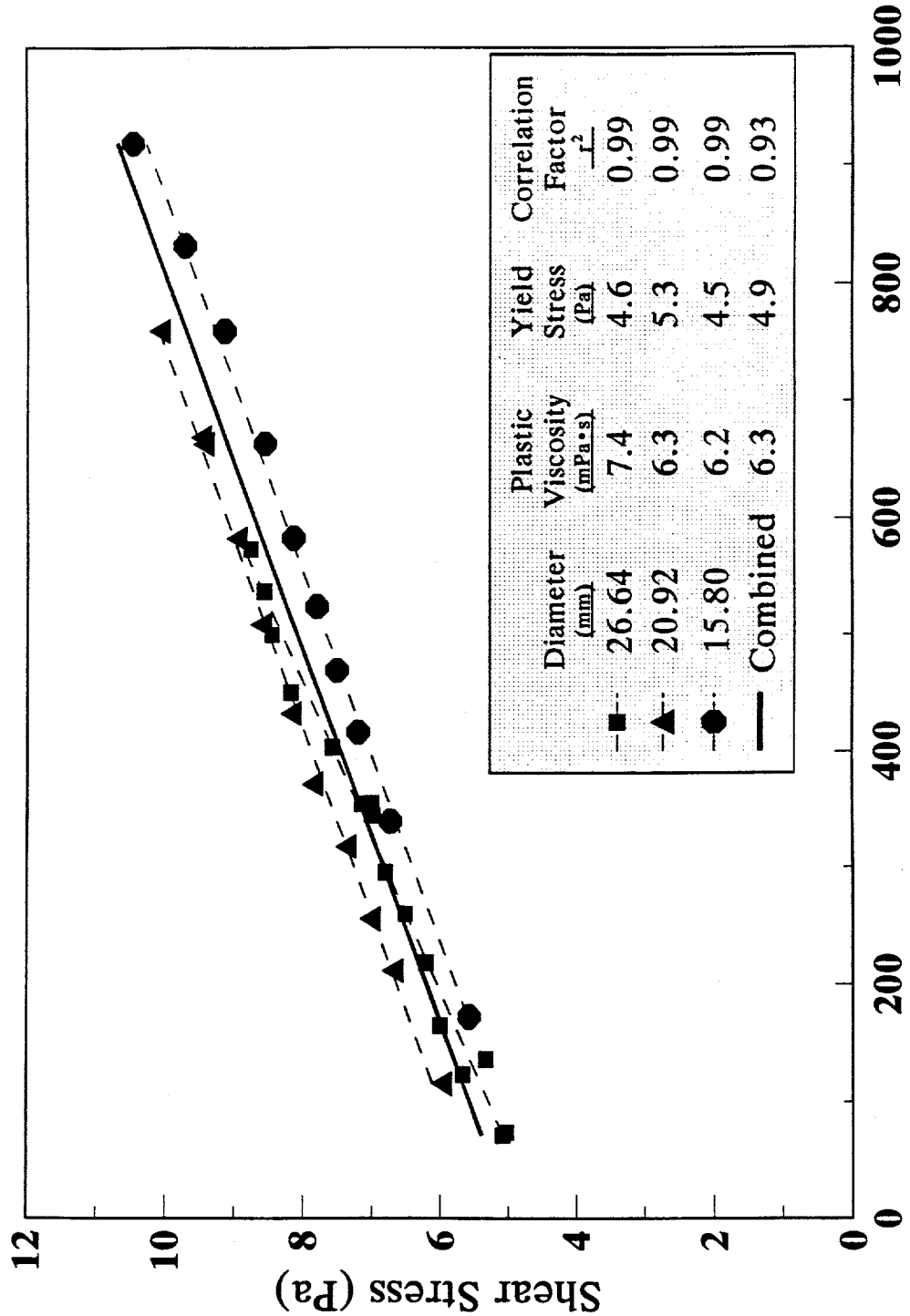

Figure D-3. Shear stress versus shear rate for run A-3 (Bingham plastic model).

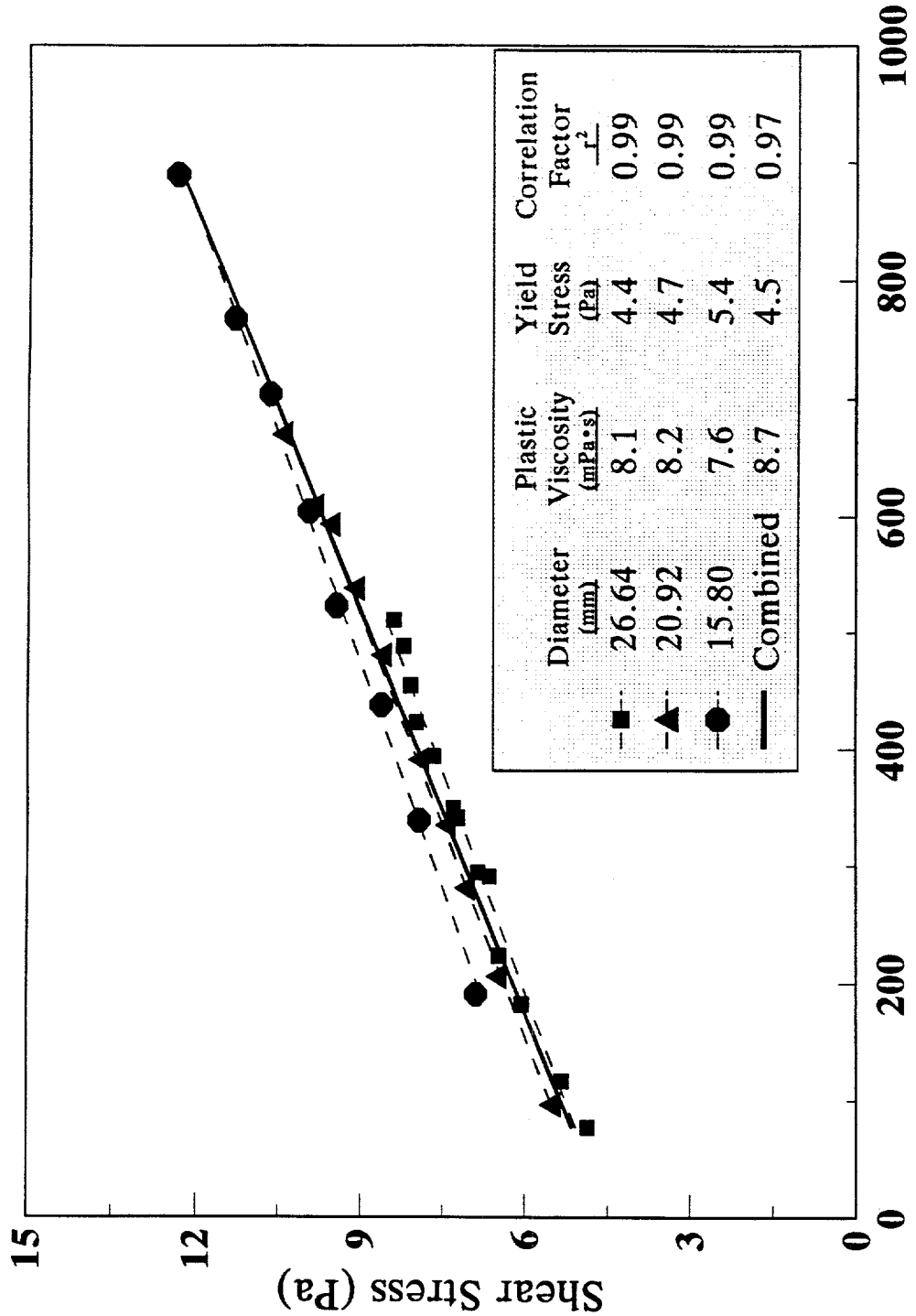

Figure D-4. Shear stress versus shear rate for run A-4 (Bingham plastic model).

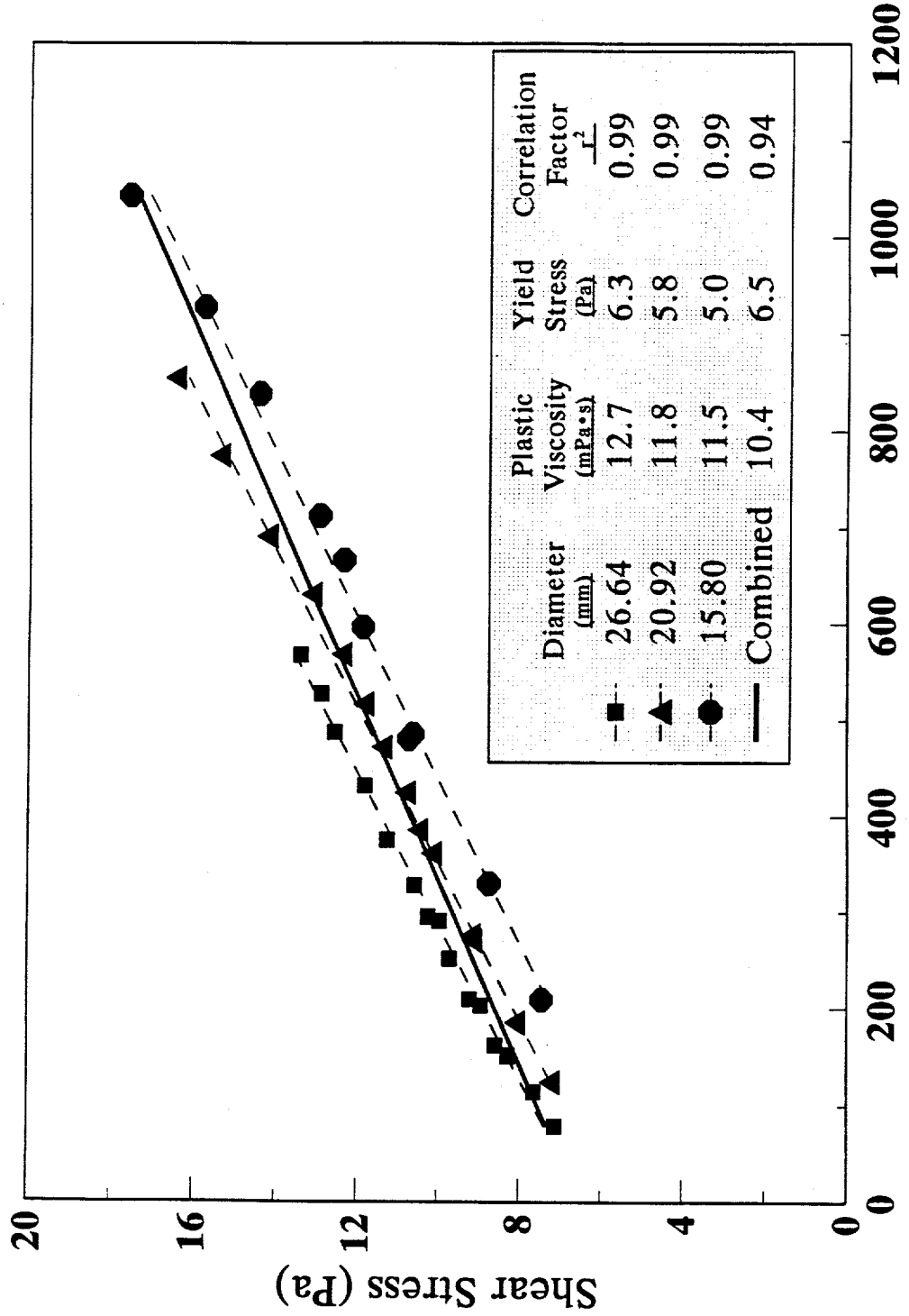

Figure D-5. Shear stress versus shear rate for run B-1 (Bingham plastic model).

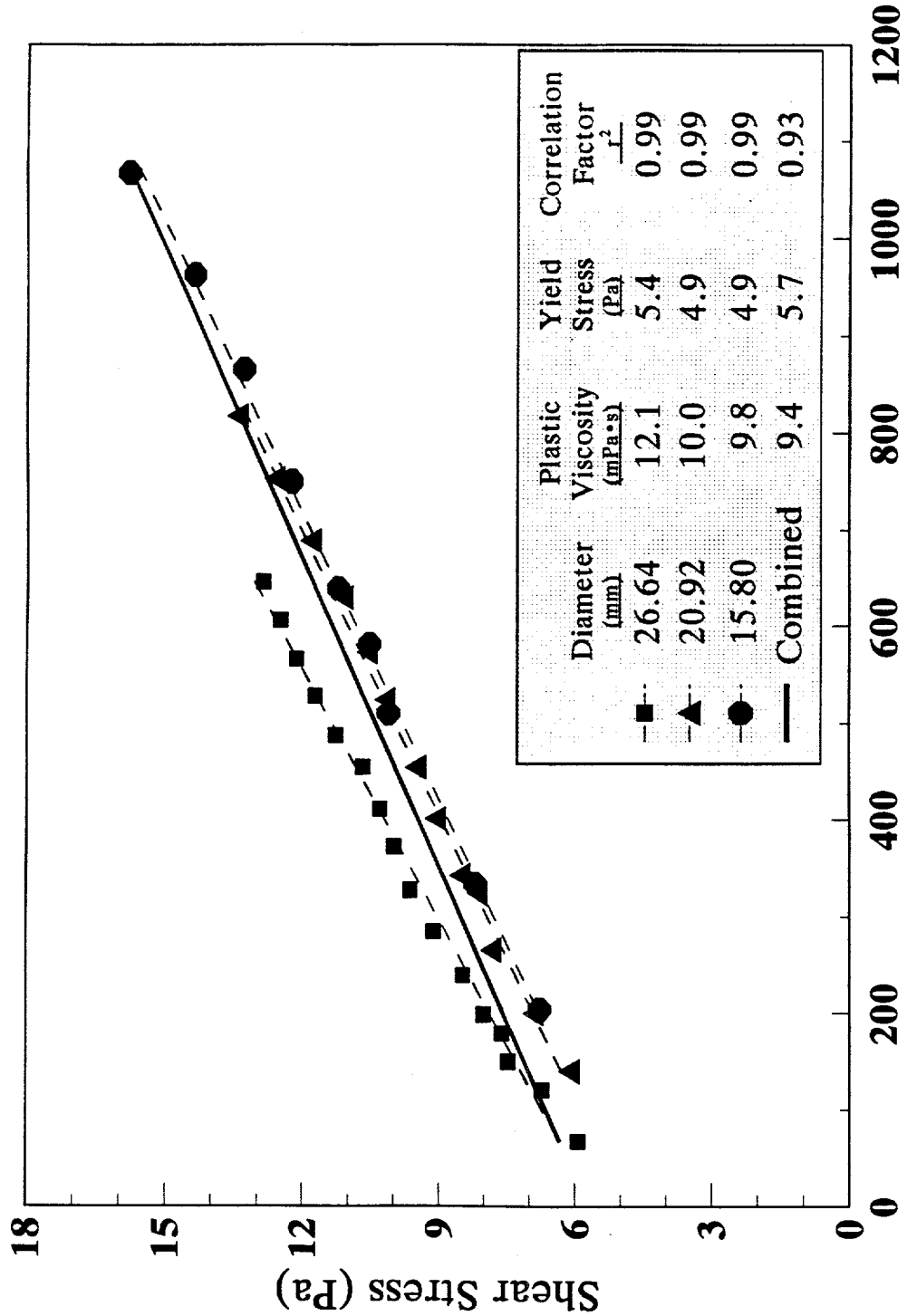

Figure D-6. Shear stress versus shear rate for run B-2 (Bingham plastic model).

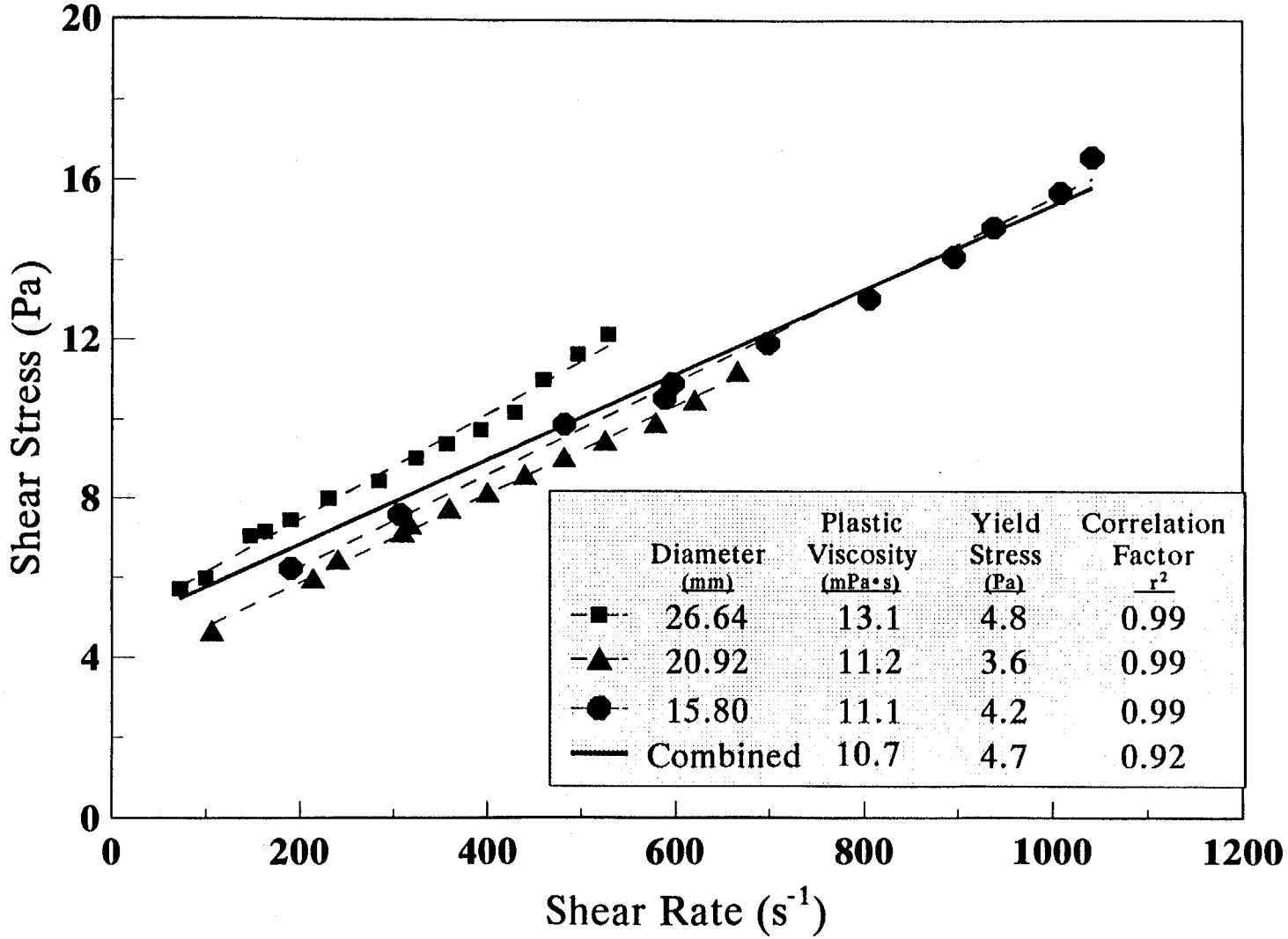

Figure D-7. Shear stress versus shear rate for run B-3 (Bingham plastic model).

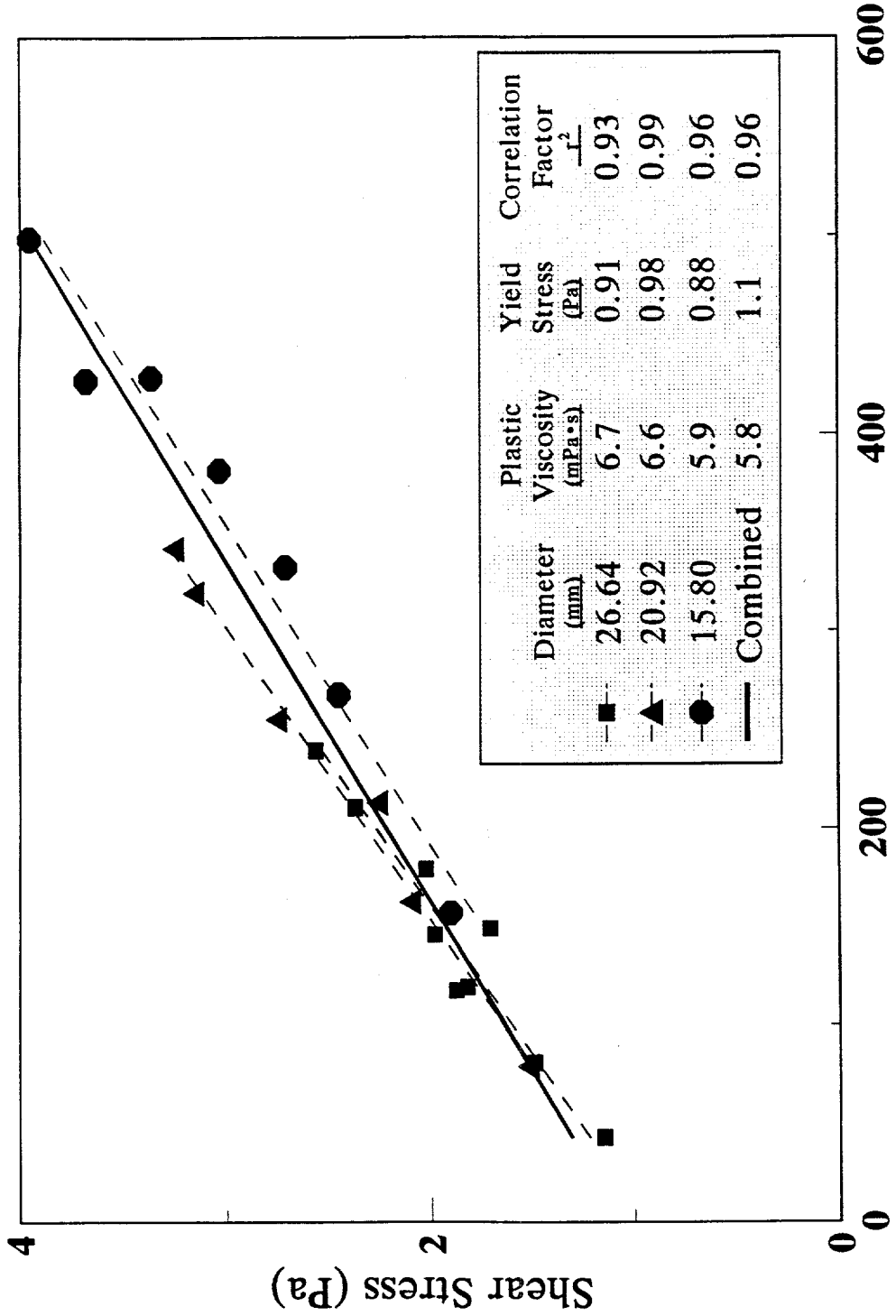

Figure D-8. Shear stress versus shear rate for run C-1 (Bingham plastic model).

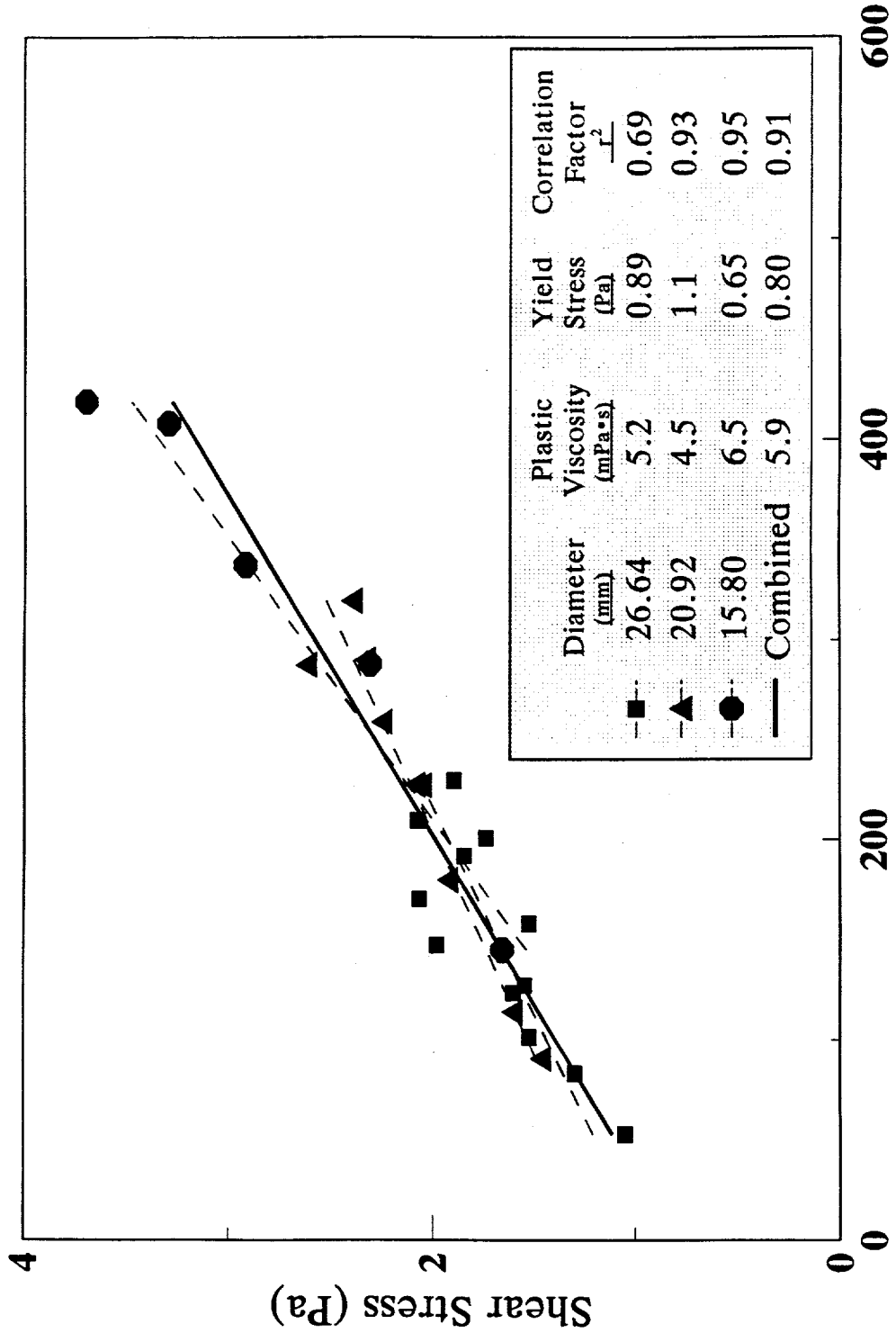

Figure D-9. Shear stress versus shear rate for run C-2 (Bingham plastic model).

APPENDIX E

GRAPHS OF FRICTION FACTORS VERSUS REYNOLDS NUMBER FOR THE BINGHAM PLASTIC MODEL

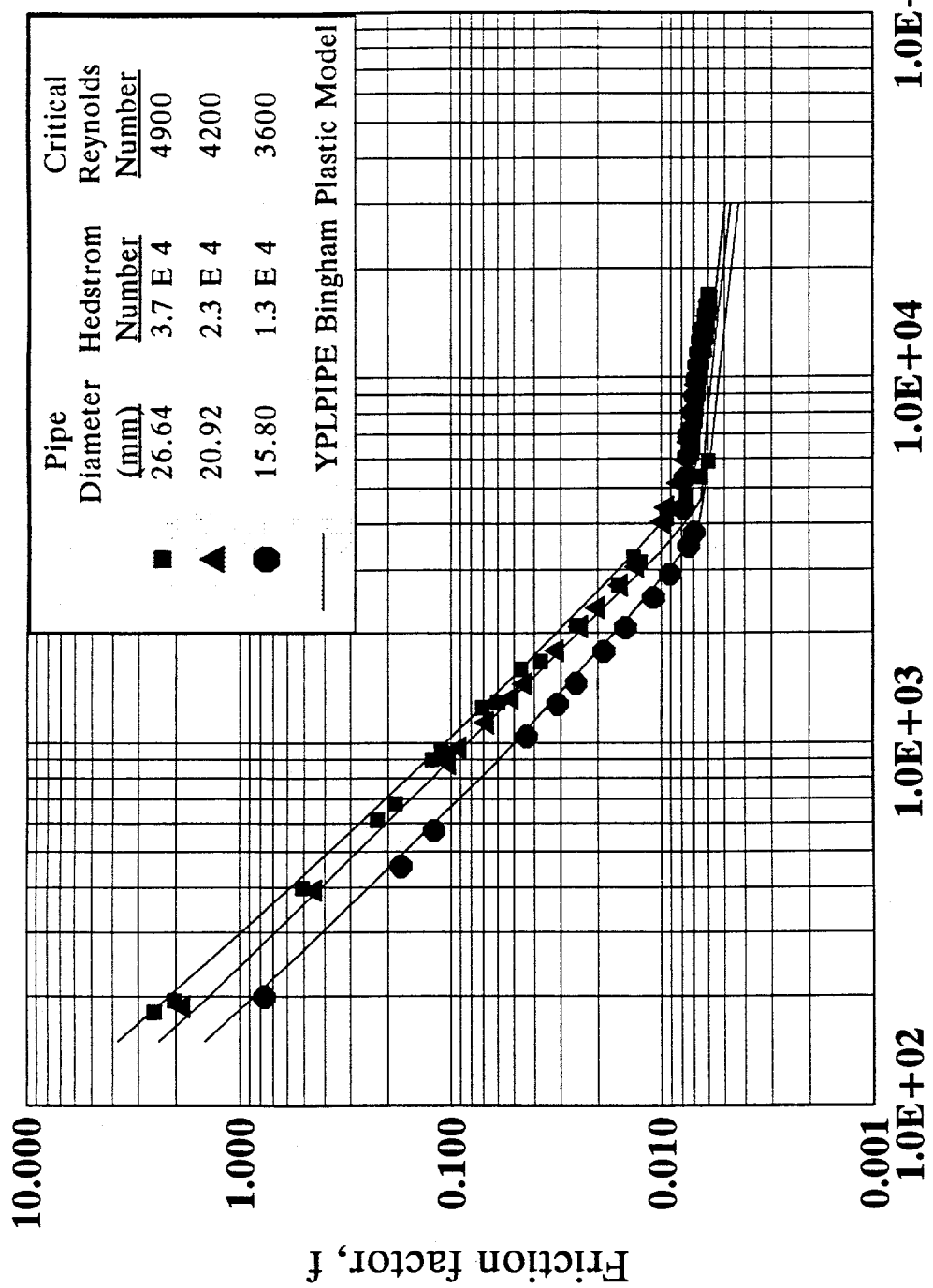

Figure E-1. Friction factor versus Reynolds number for run A-1 (Bingham plastic model).

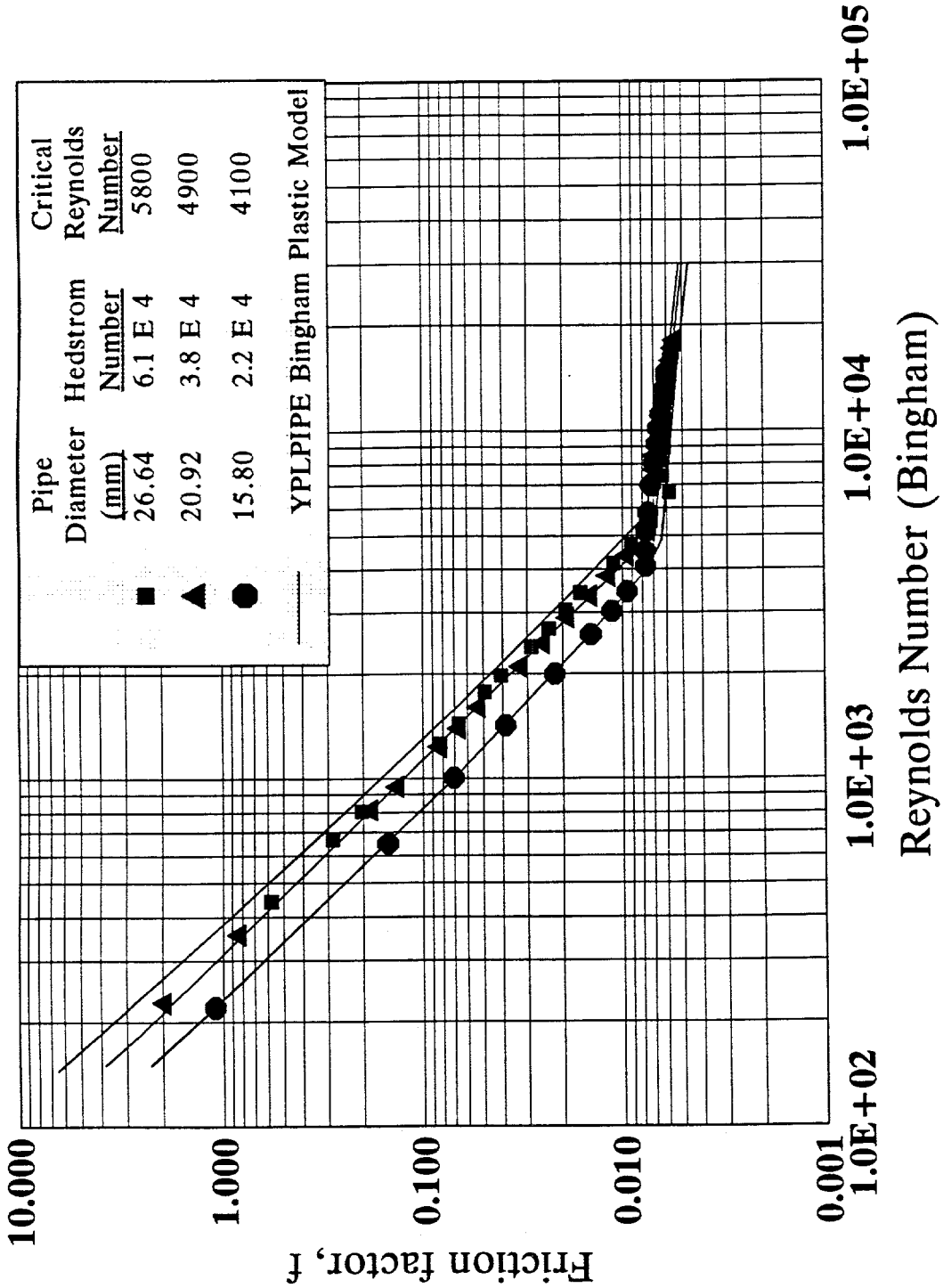

Figure E-2. Friction factor versus Reynolds number for run A-2 (Bingham plastic model).

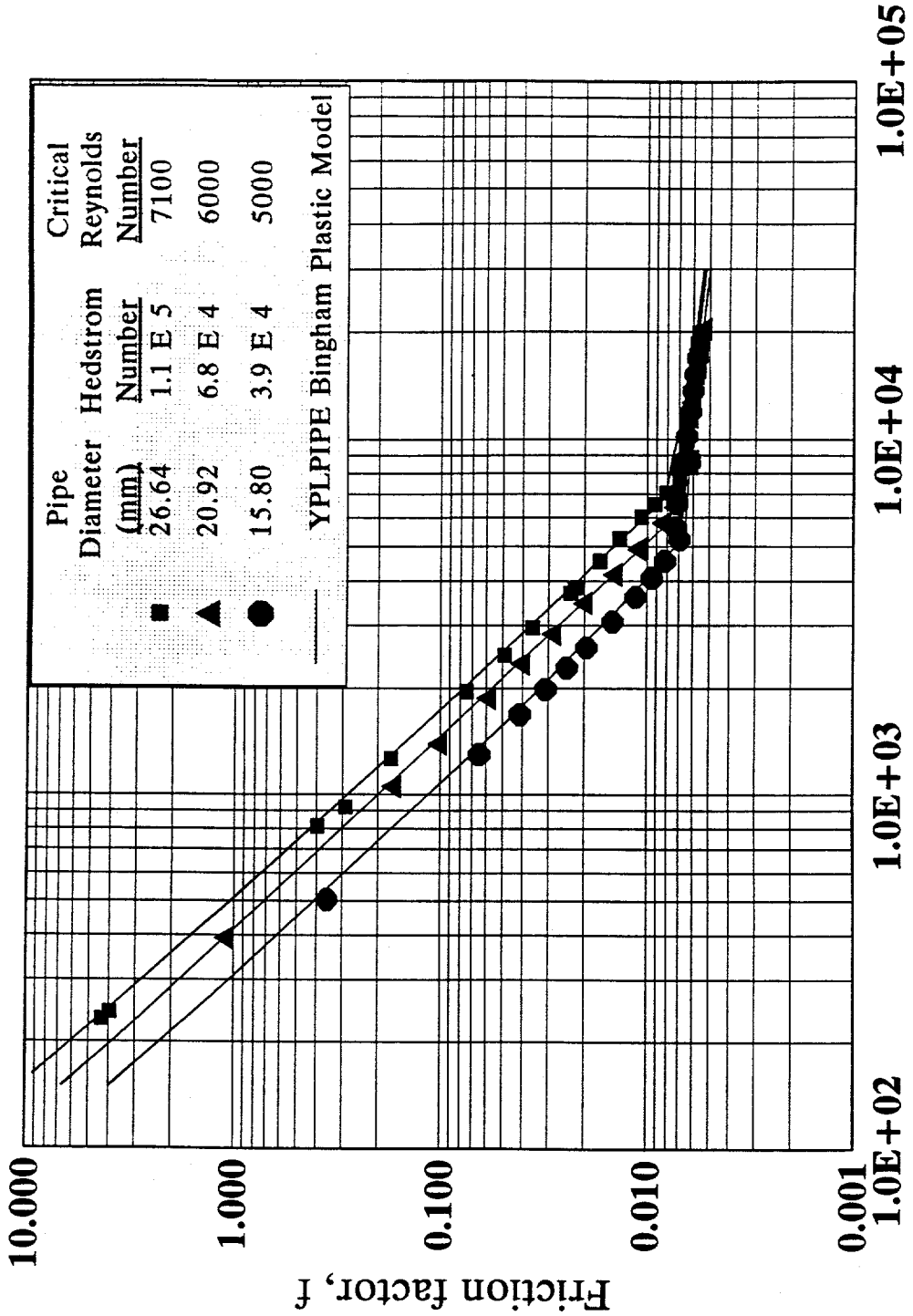

Figure E-3. Friction factor versus Reynolds number for run A-3 (Bingham plastic model).

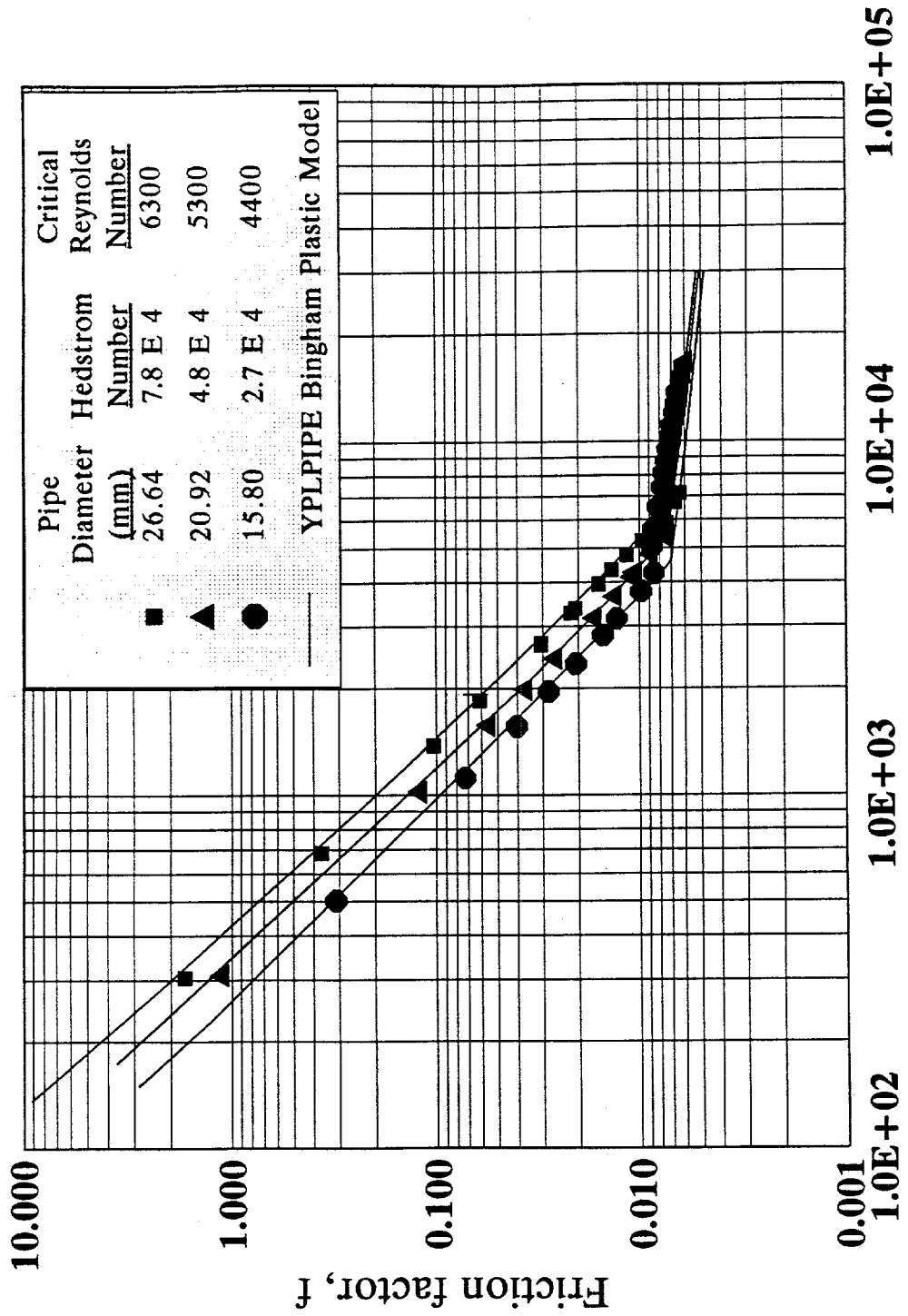

Figure E-4. Friction factor versus Reynolds number for run A-4 (Bingham plastic model).

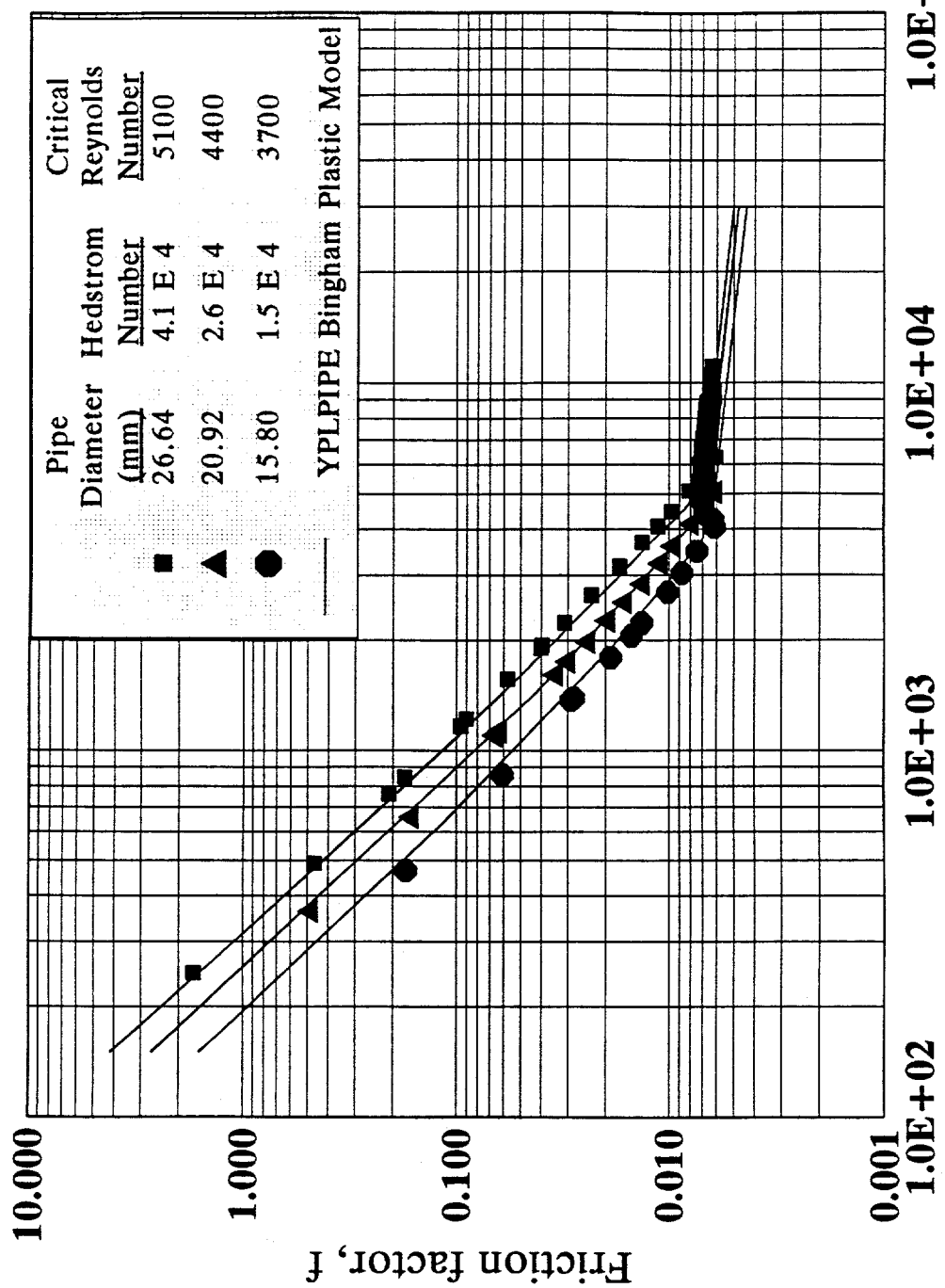

Figure E-5. Friction factor versus Reynolds number for run B-1 (Bingham plastic model).

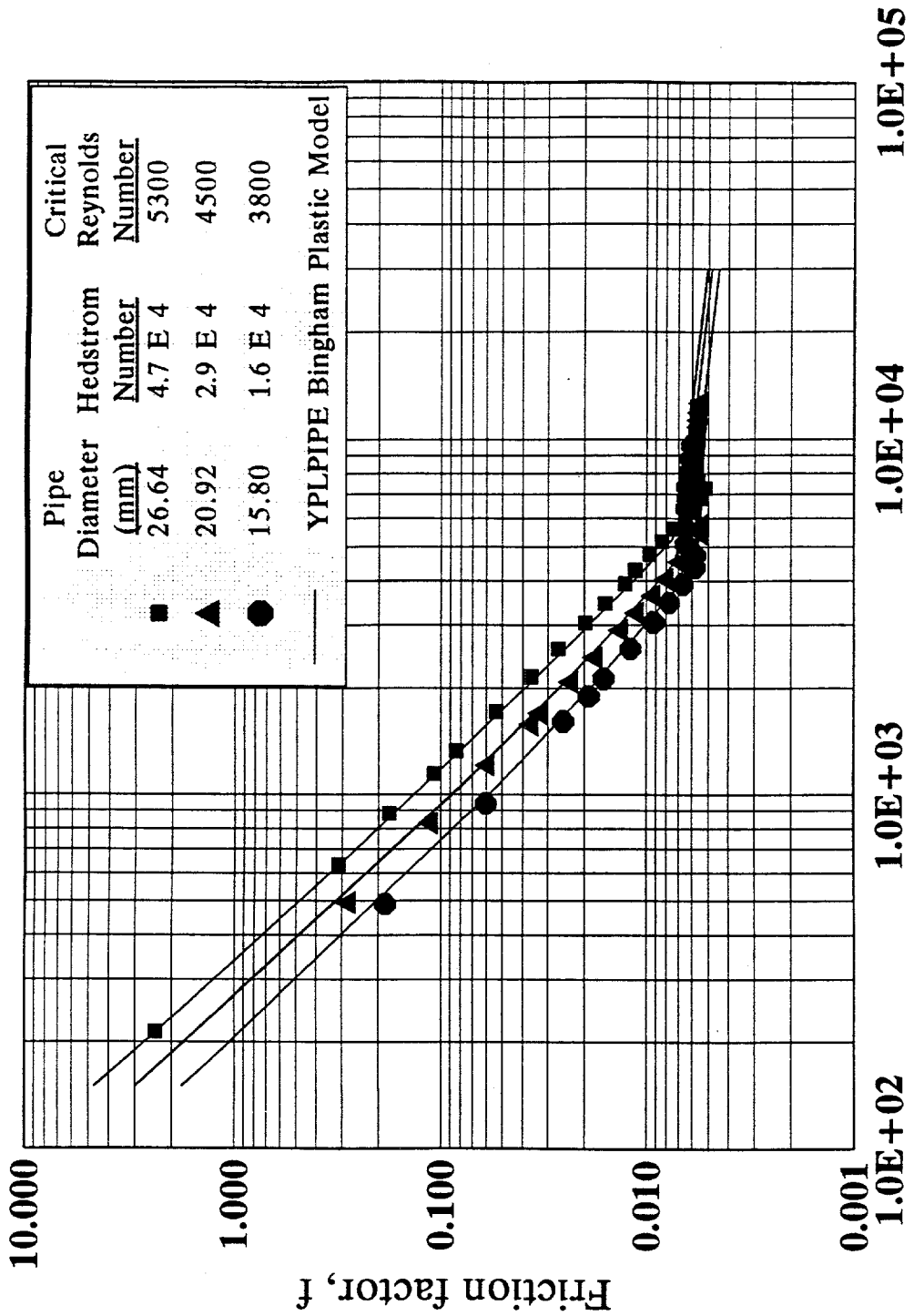

Figure E-6. Friction factor versus Reynolds number for run B-2 (Bingham plastic model).

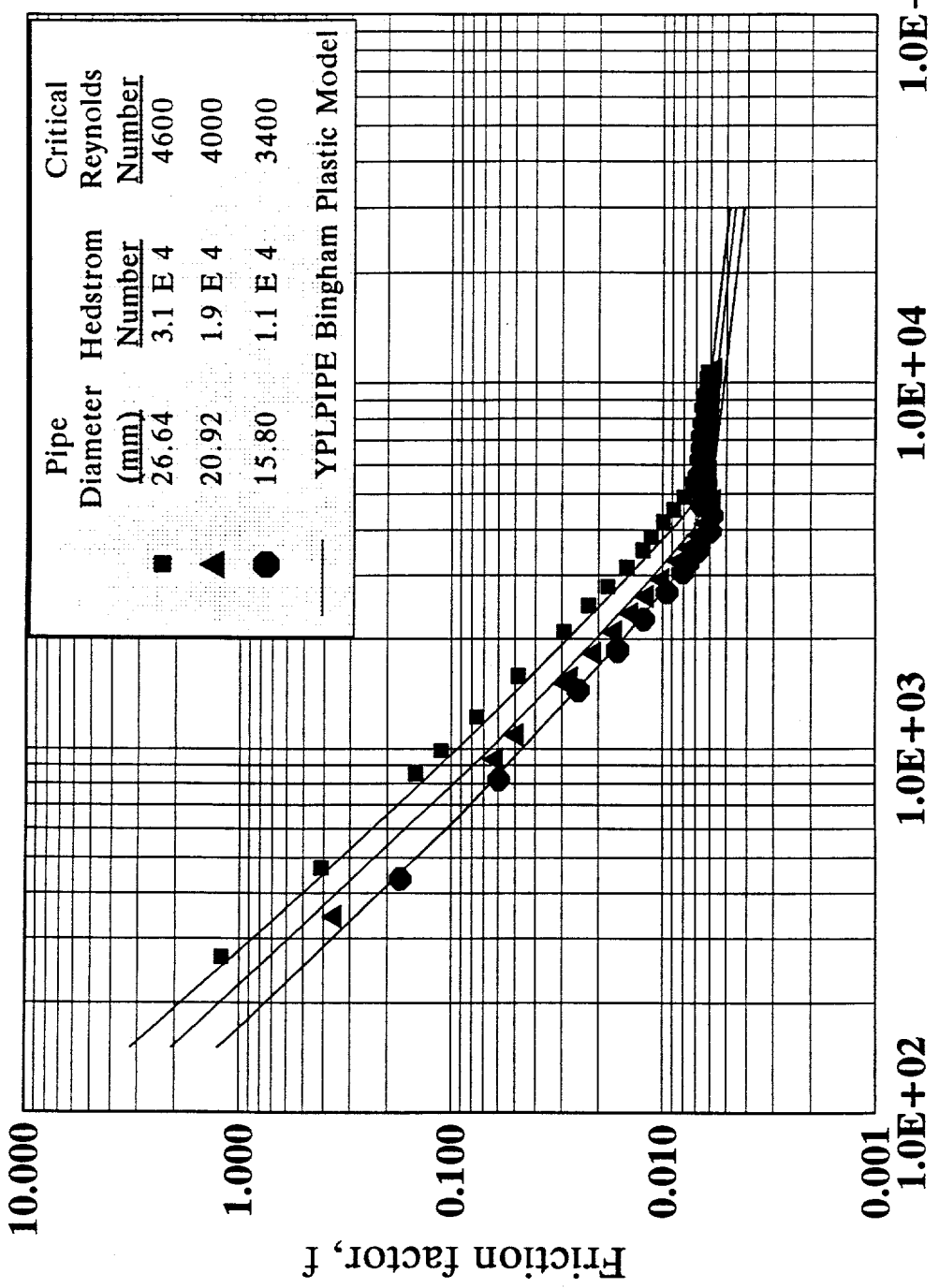

Figure E-7. Friction factor versus Reynolds number for run B-3 (Bingham plastic model).

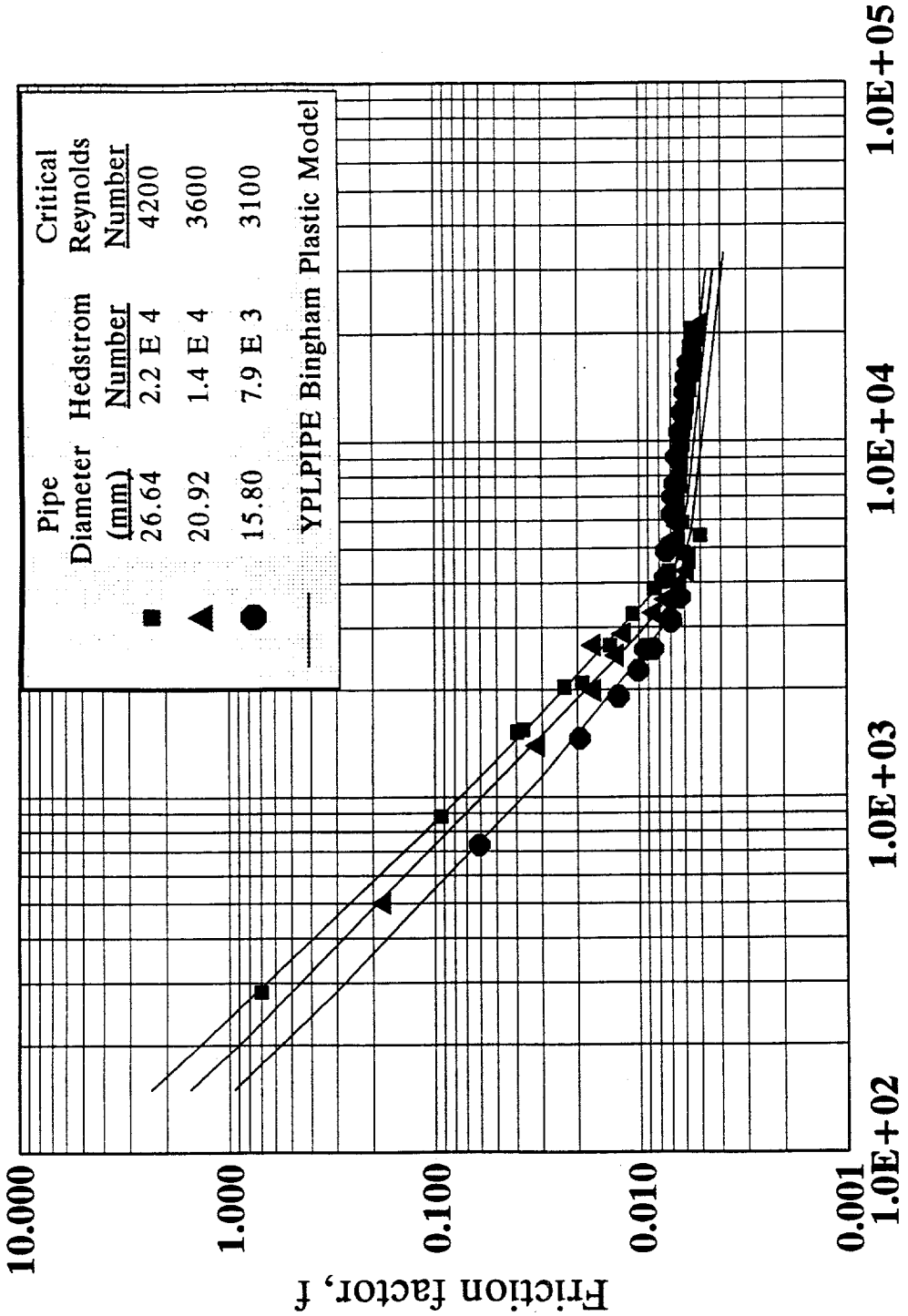

Figure E-8. Friction factor versus Reynolds number for run C-1 (Bingham plastic model).

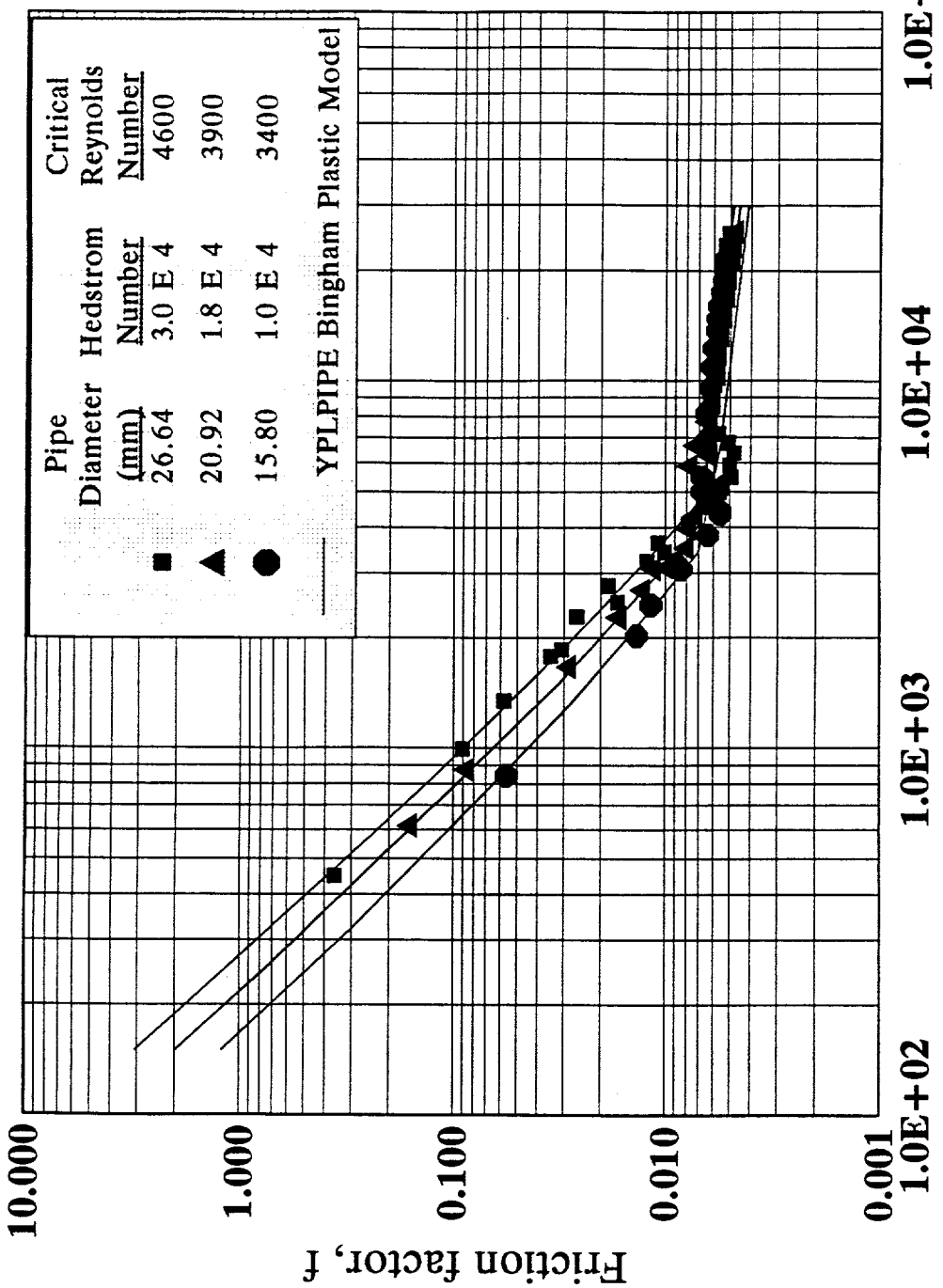

Figure E-9. Friction factor versus Reynolds number for run C-2 (Bingham plastic model).

APPENDIX F

RHEOGRAMS FOR THE POWER LAW MODEL

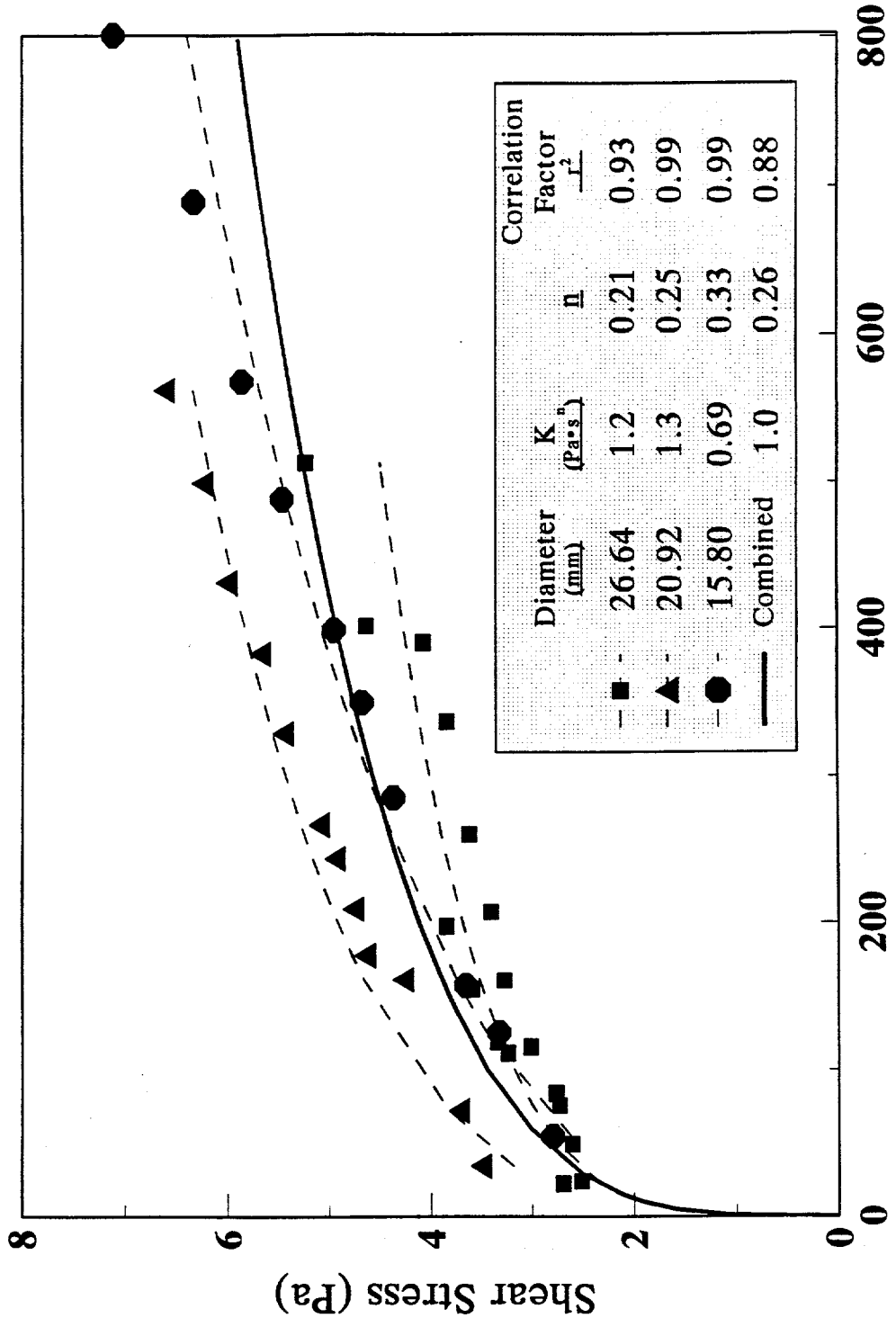

Figure F-1. Shear stress versus shear rate for run A-1 (Power Law model).

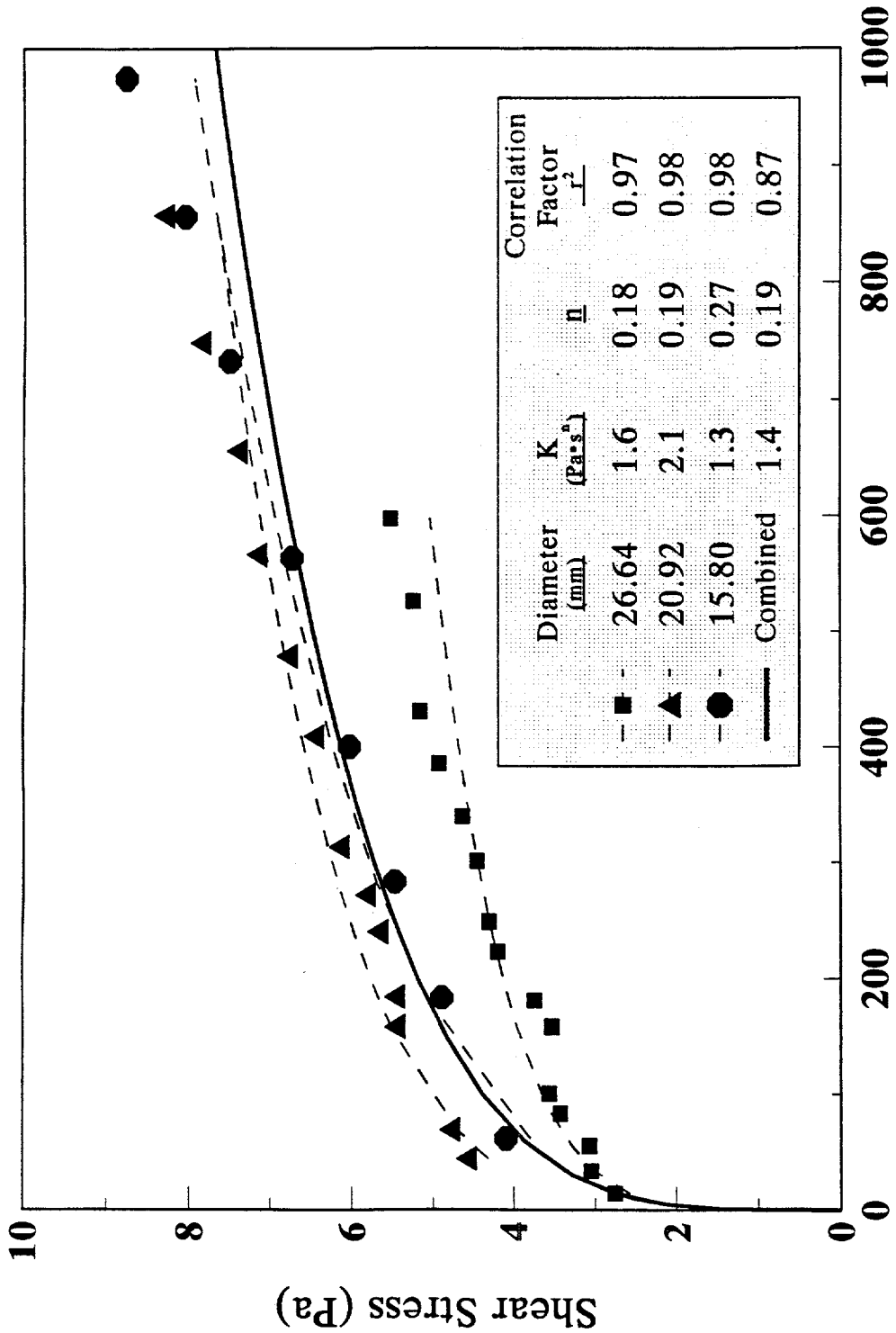

Figure F-2. Shear stress versus shear rate for run A-2 (Power Law model).

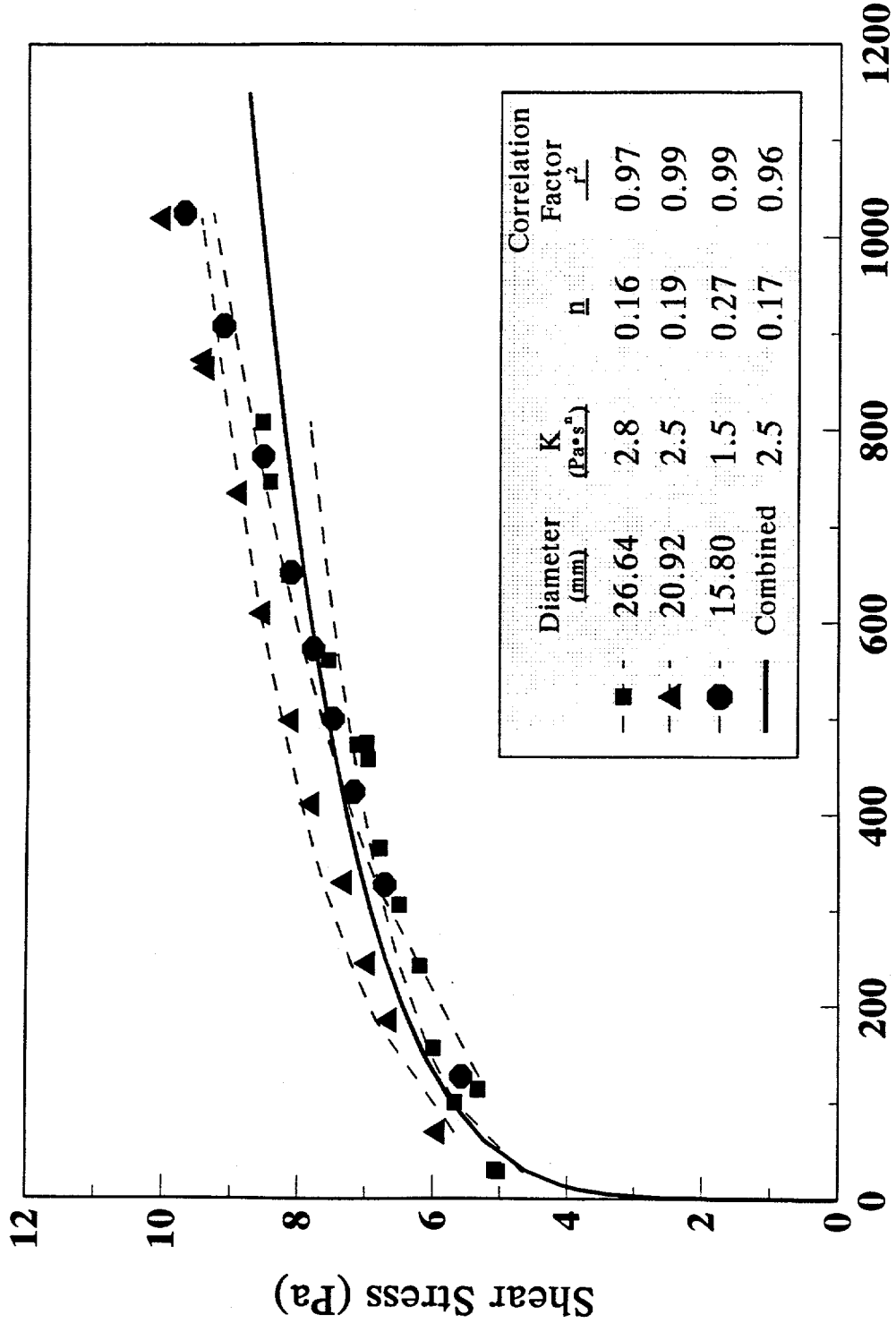

Figure F-3. Shear stress versus shear rate for run A-3 (Power Law model).

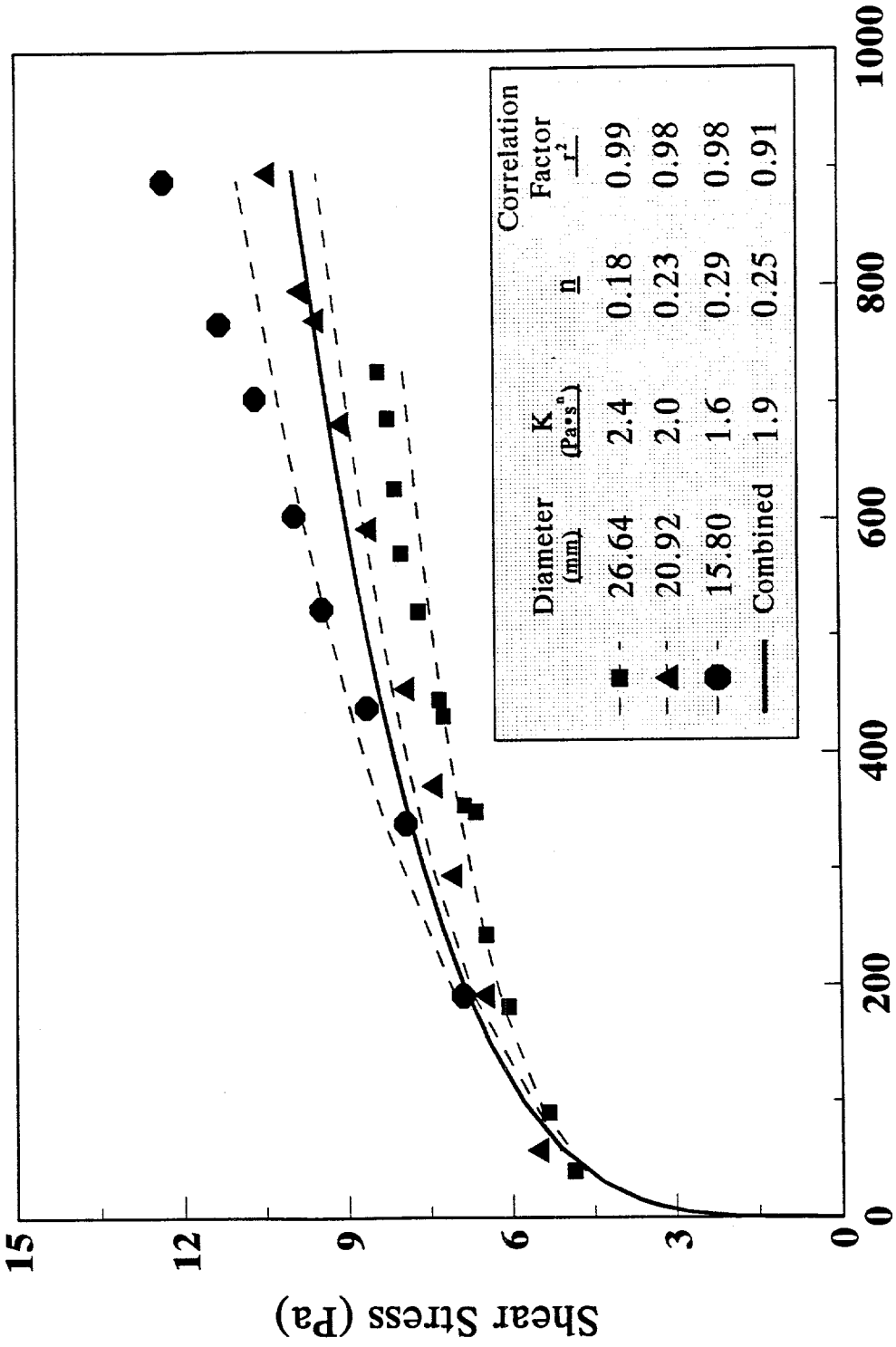

Figure F-4. Shear stress versus shear rate for run A-4 (Power Law model).

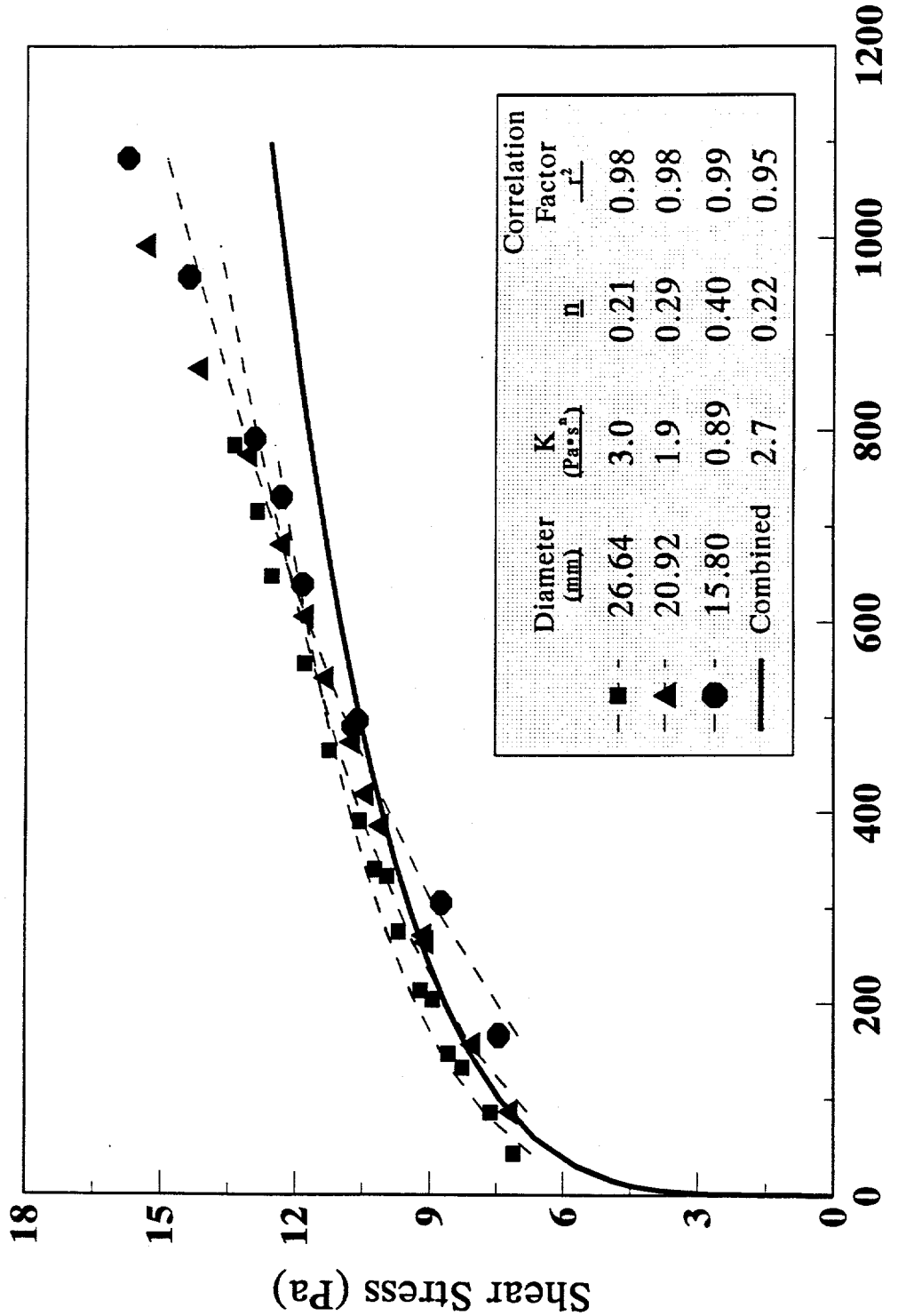

Figure F-5. Shear stress versus shear rate for run B-1 (Power Law model).

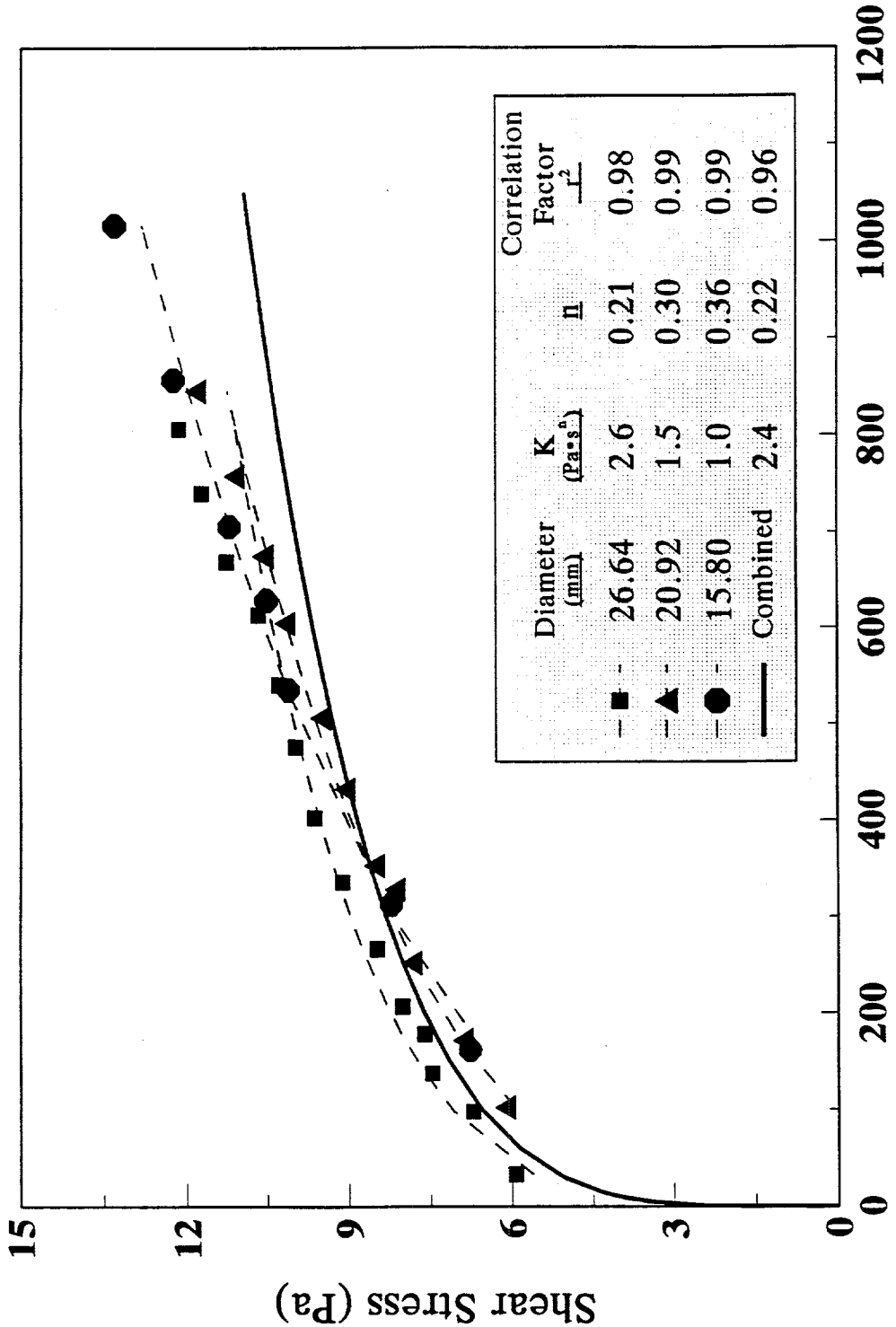

Figure F-6. Shear stress versus shear rate for run B-2 (Power Law model).

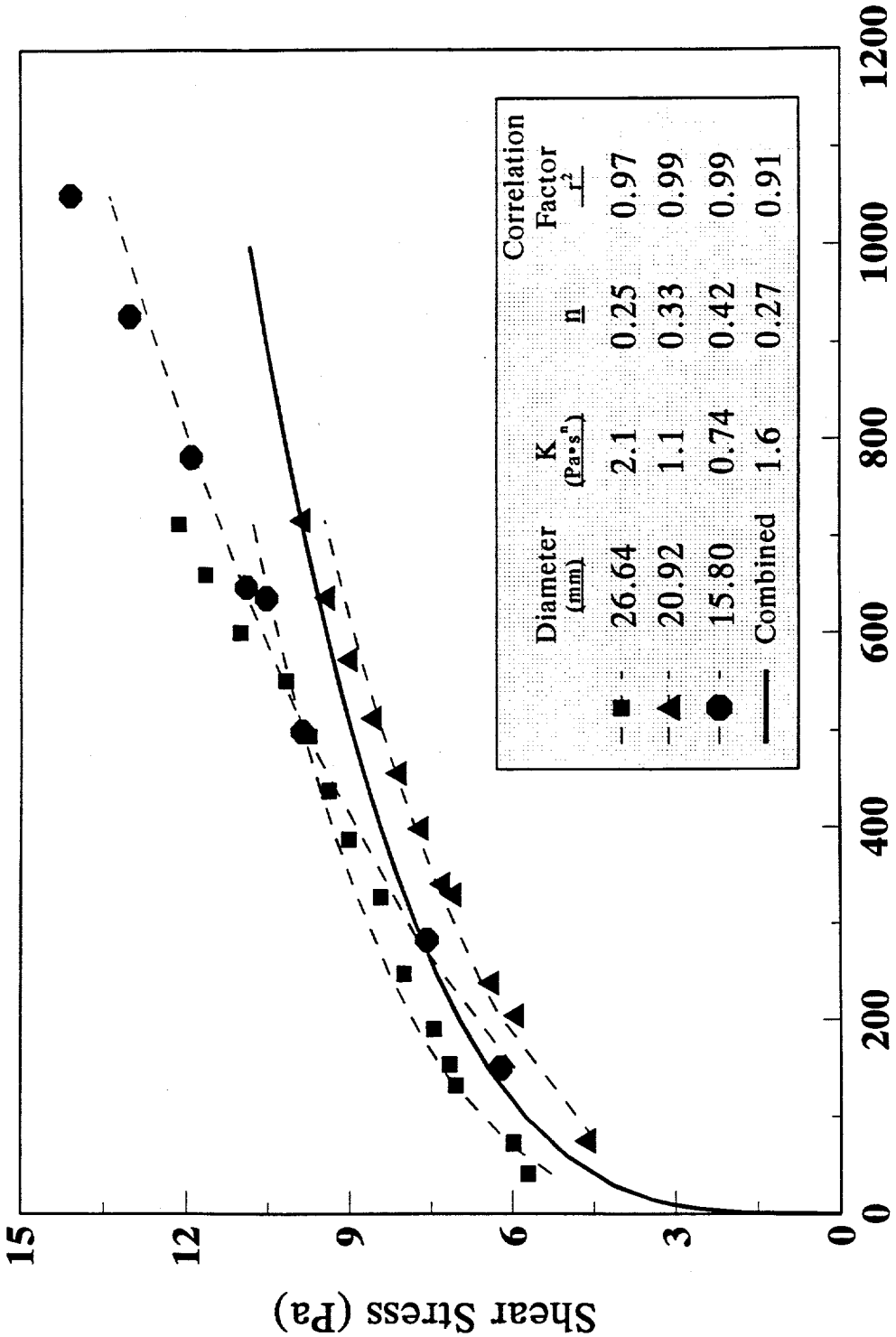

Figure F-7. Shear stress versus shear rate for run B-3 (Power Law model).

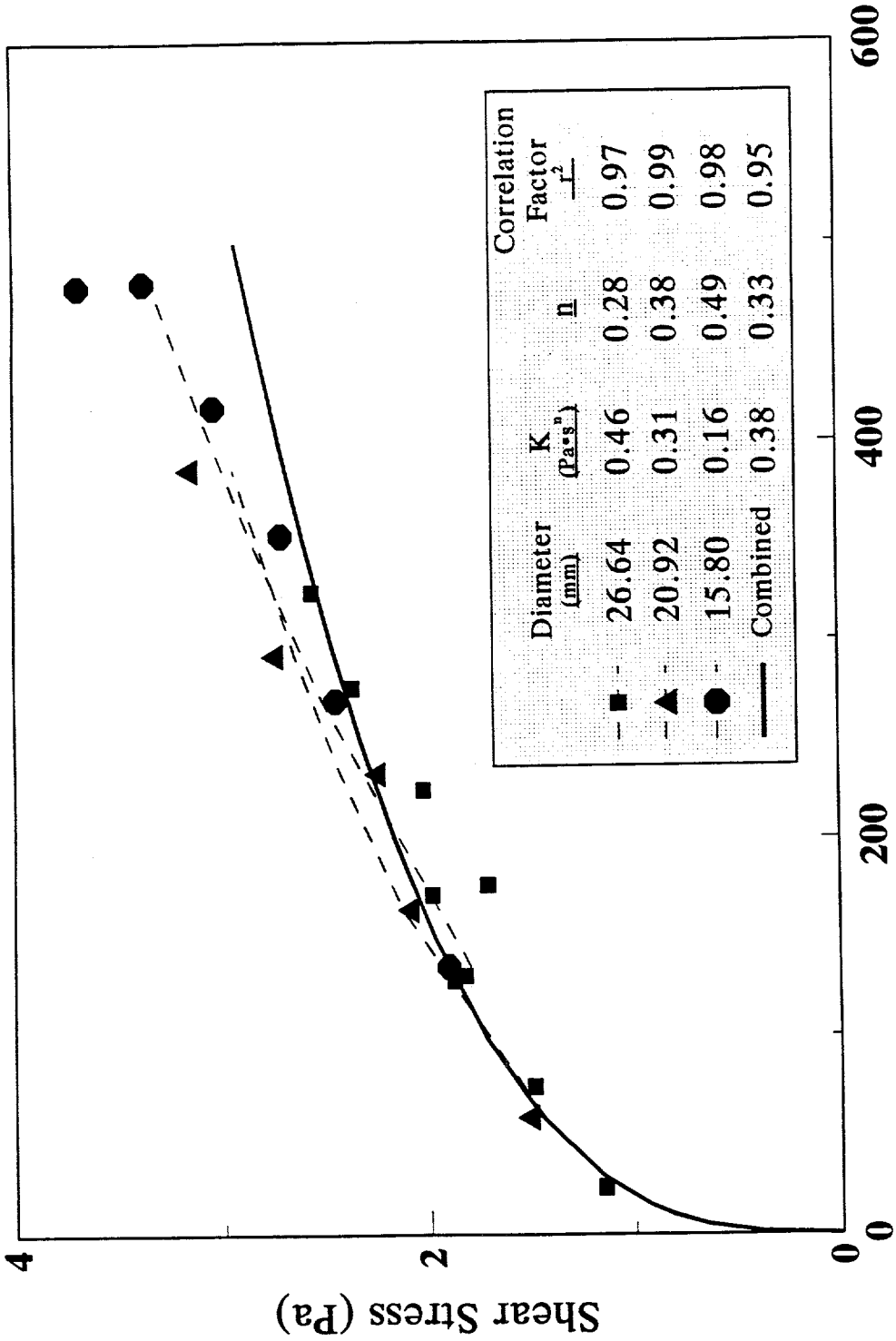

Figure F-8. Shear stress versus shear rate for run C-1 (Power Law model).

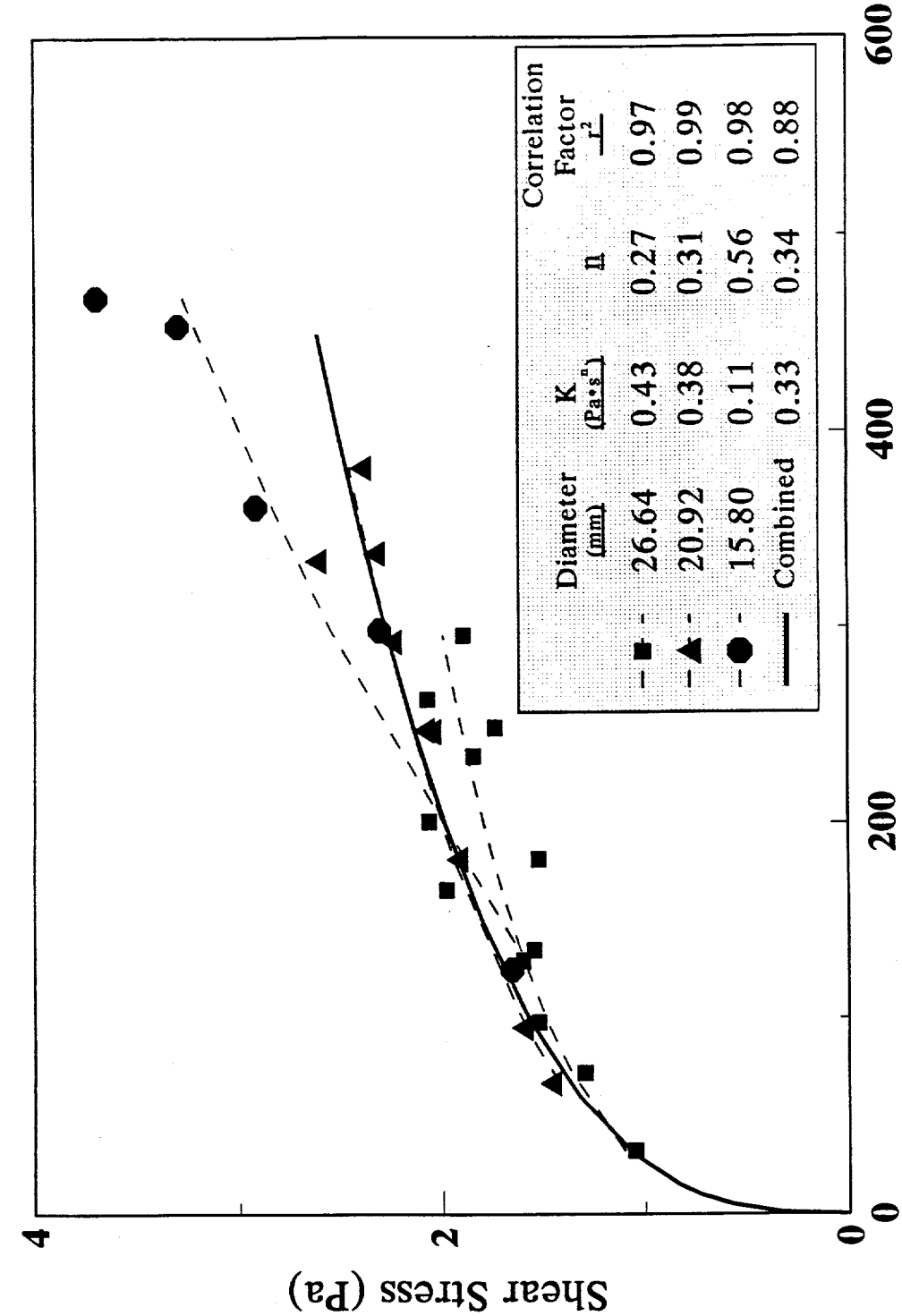

Figure F-9. Shear stress versus shear rate for run C-2 (Power Law model).

APPENDIX G

GRAPHS OF FRICTION FACTOR VERSUS REYNOLDS NUMBER FOR THE POWER LAW MODEL

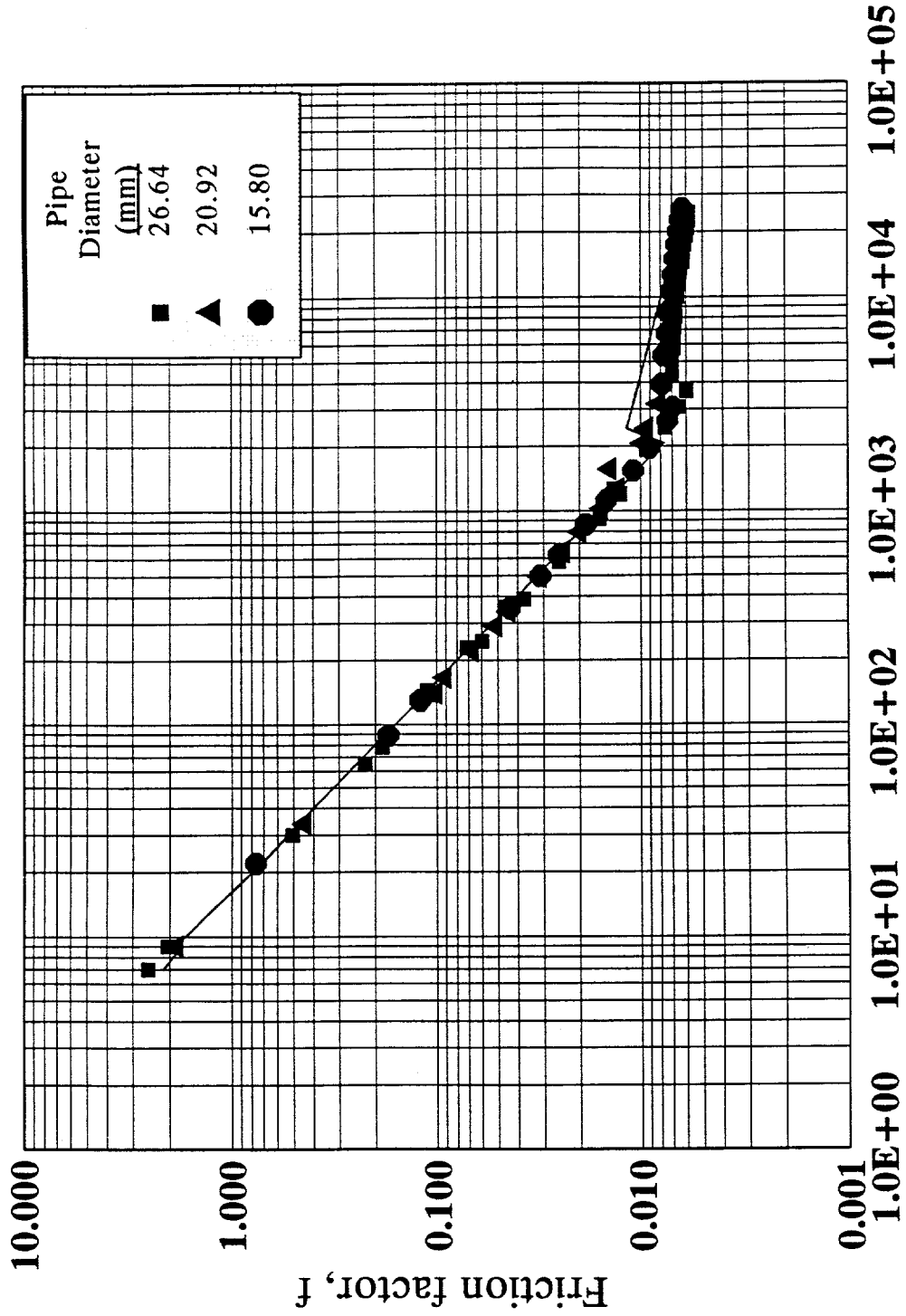

Figure G-1. Friction factor versus Reynolds number for run A-1 (Power Law model).

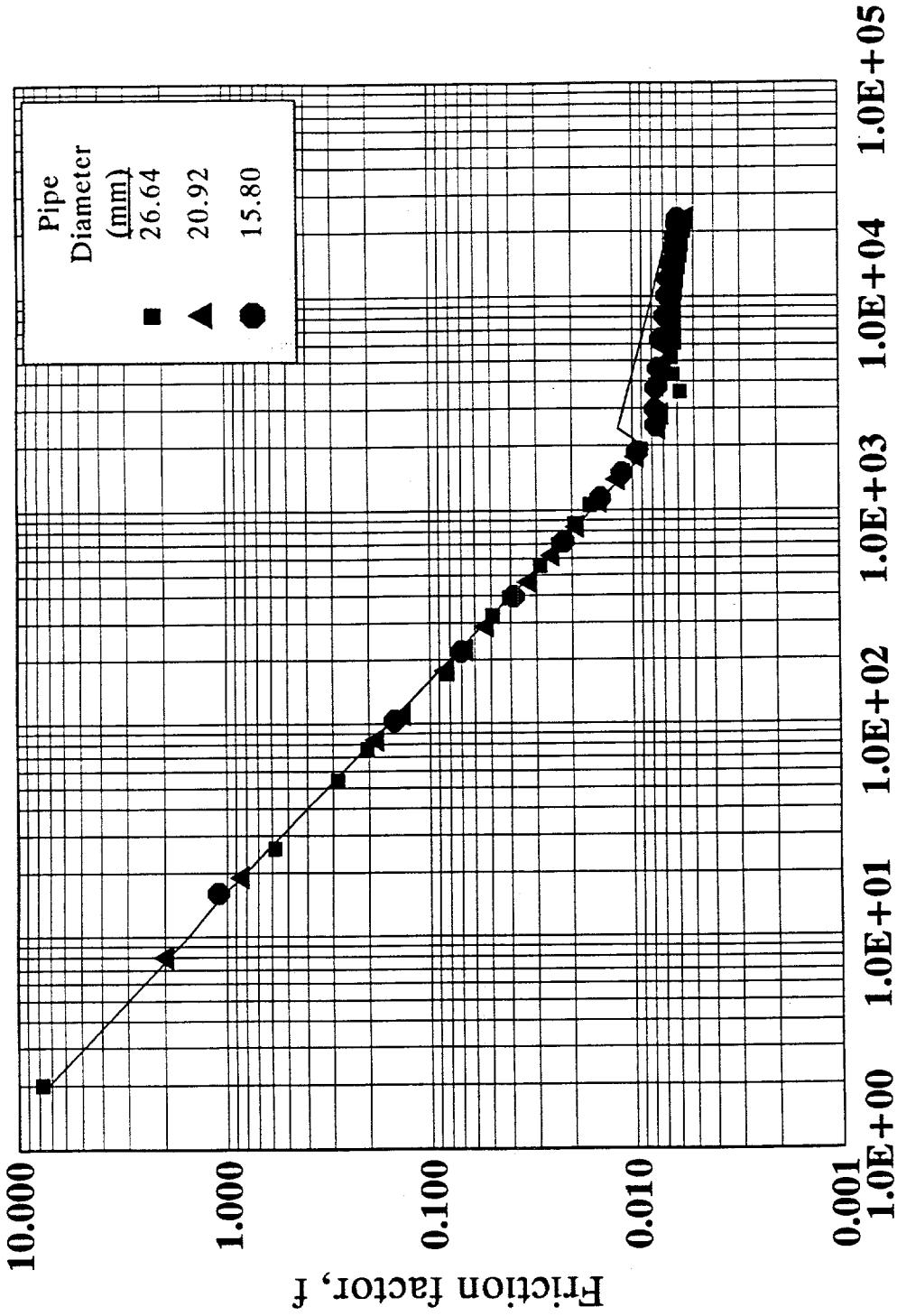

Figure G-2. Friction factor versus Reynolds number for run A-2 (Power Law model).

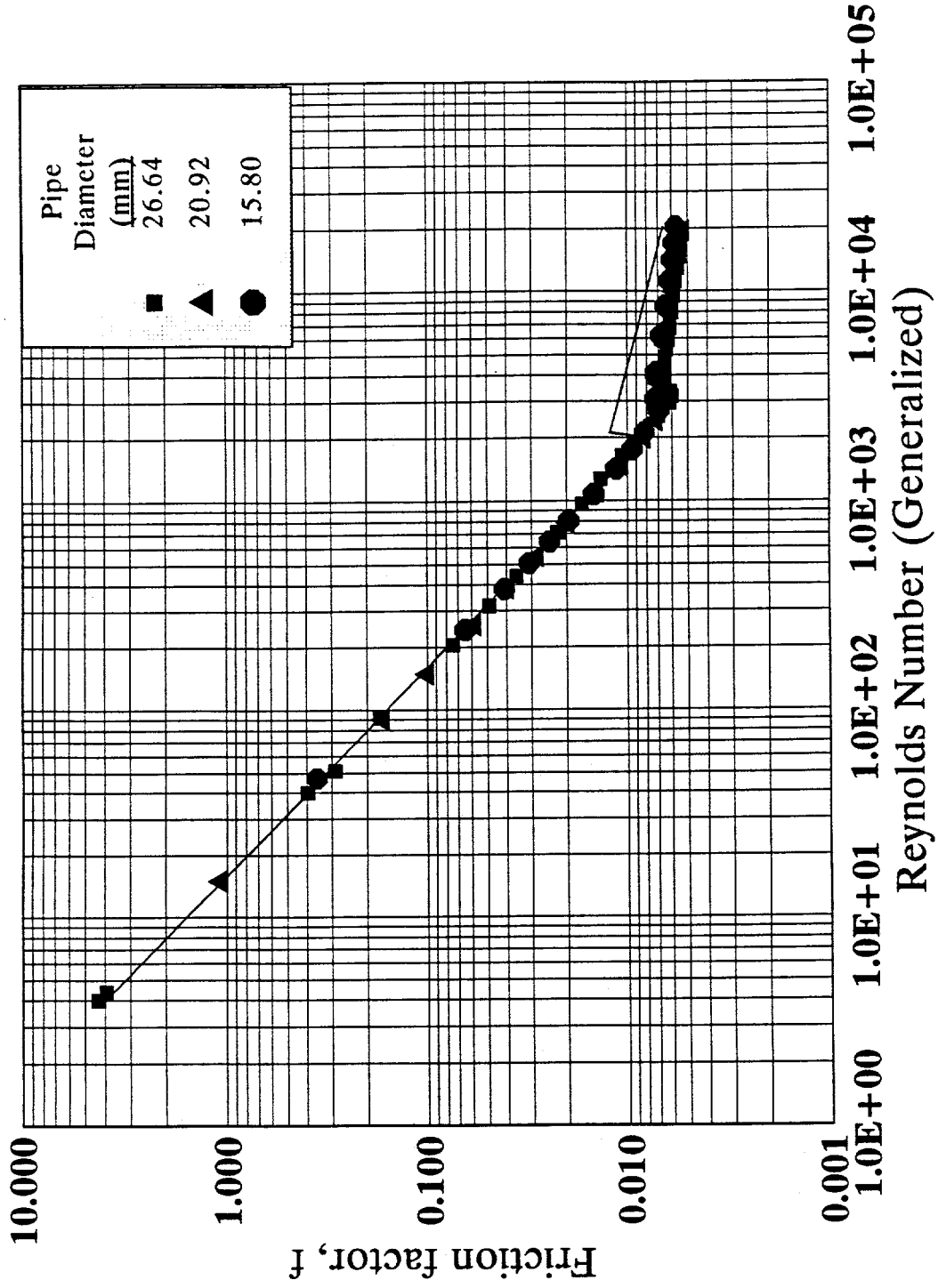

Figure G-3. Friction factor versus Reynolds number for run A-3 (Power Law model).

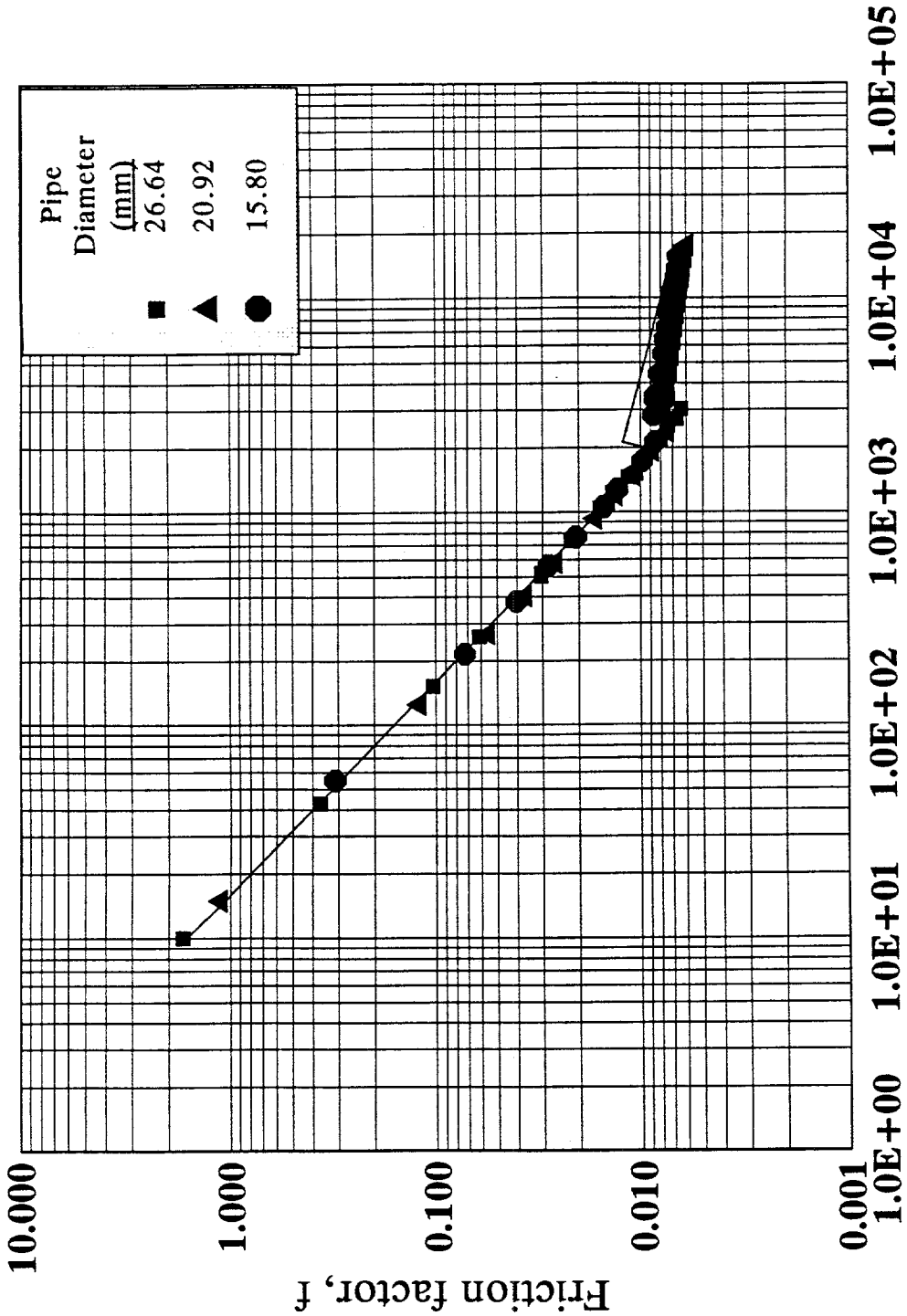

Figure G-4. Friction factor versus Reynolds number for run A-4 (Power Law model).

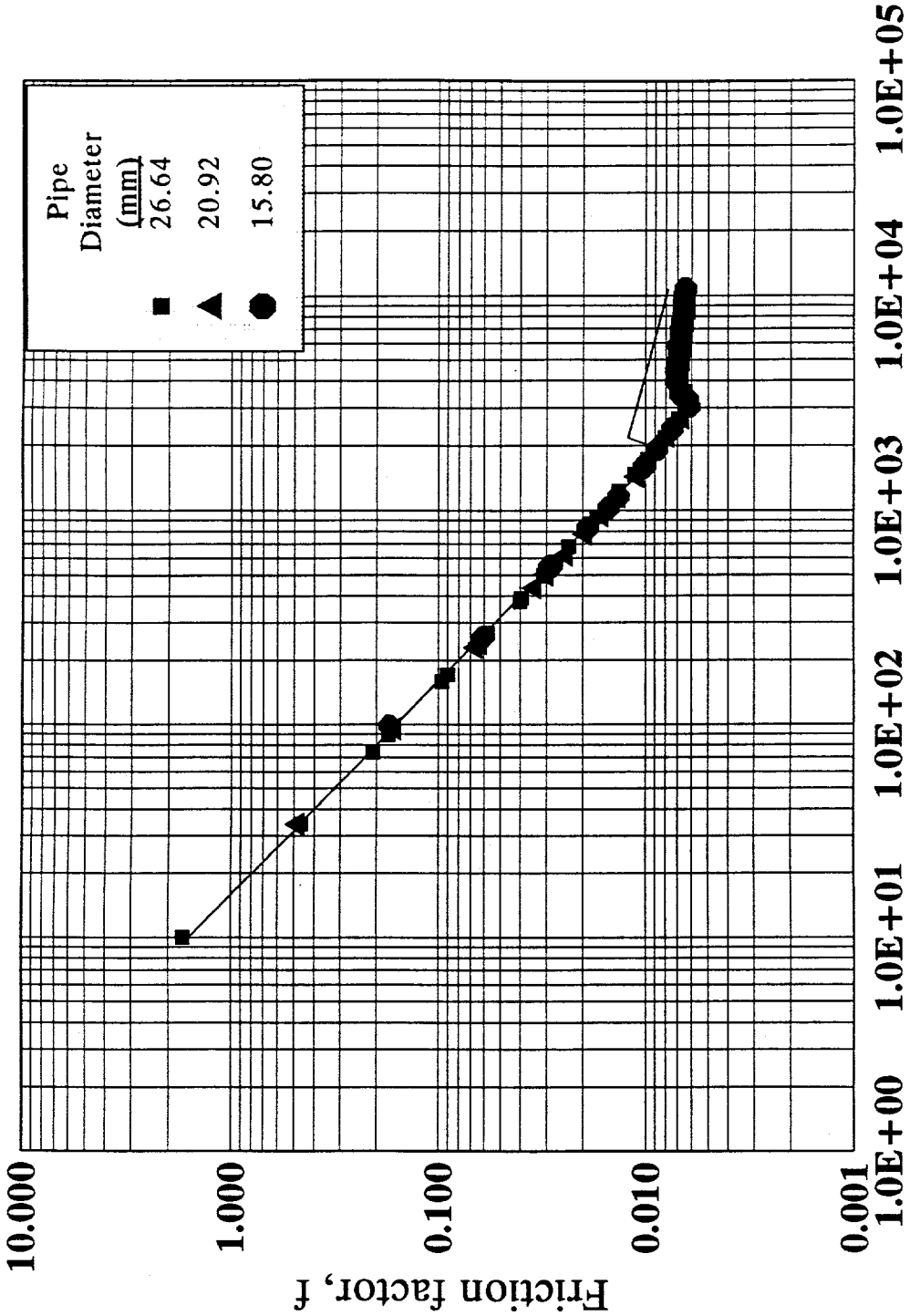

Figure G-5. Friction factor versus Reynolds number for run B-1 (Power Law model).

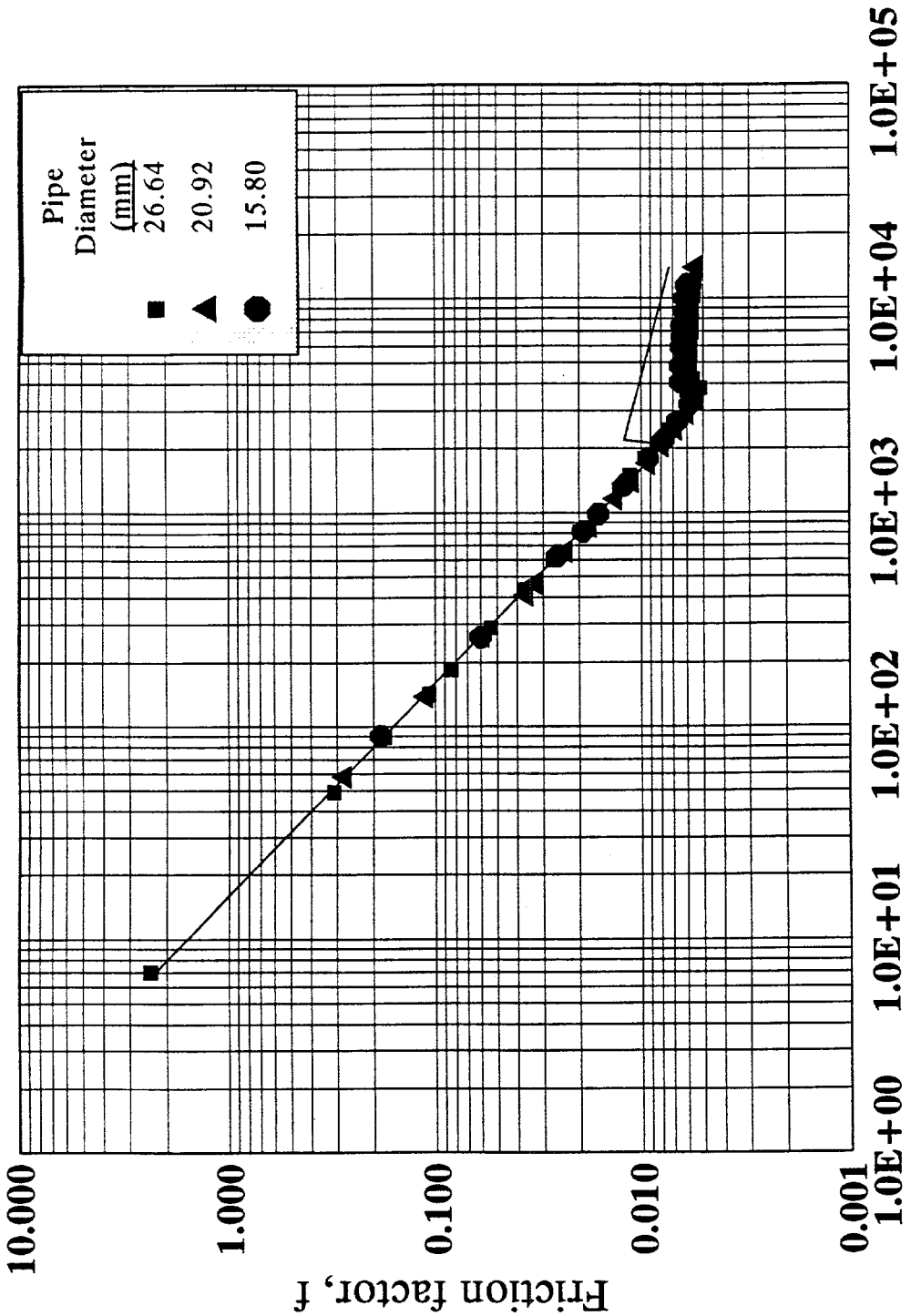

Figure G-6. Friction factor versus Reynolds number for run B-2 (Power Law model).

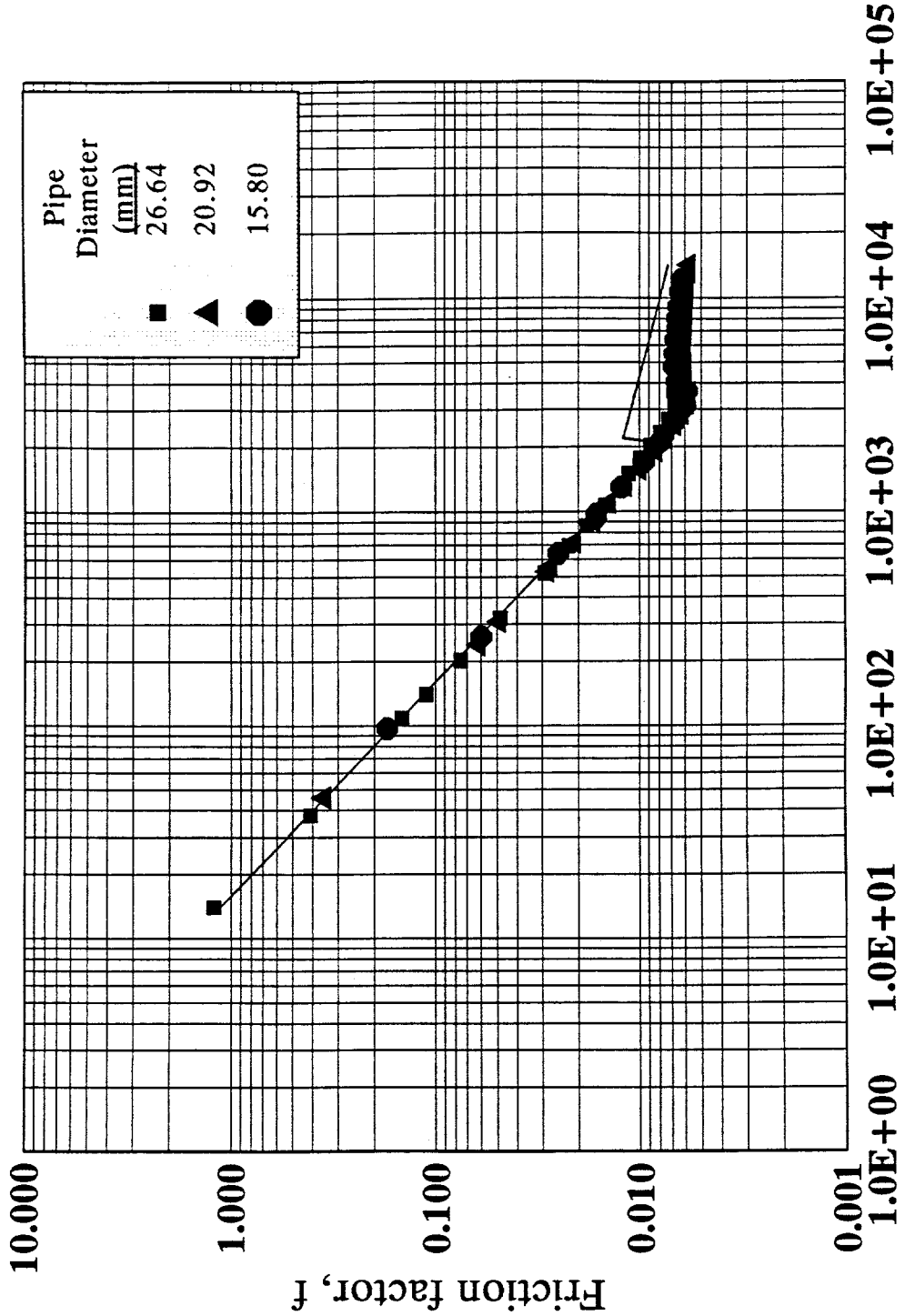

Figure G-7. Friction factor versus Reynolds number for run B-3 (Power Law model).

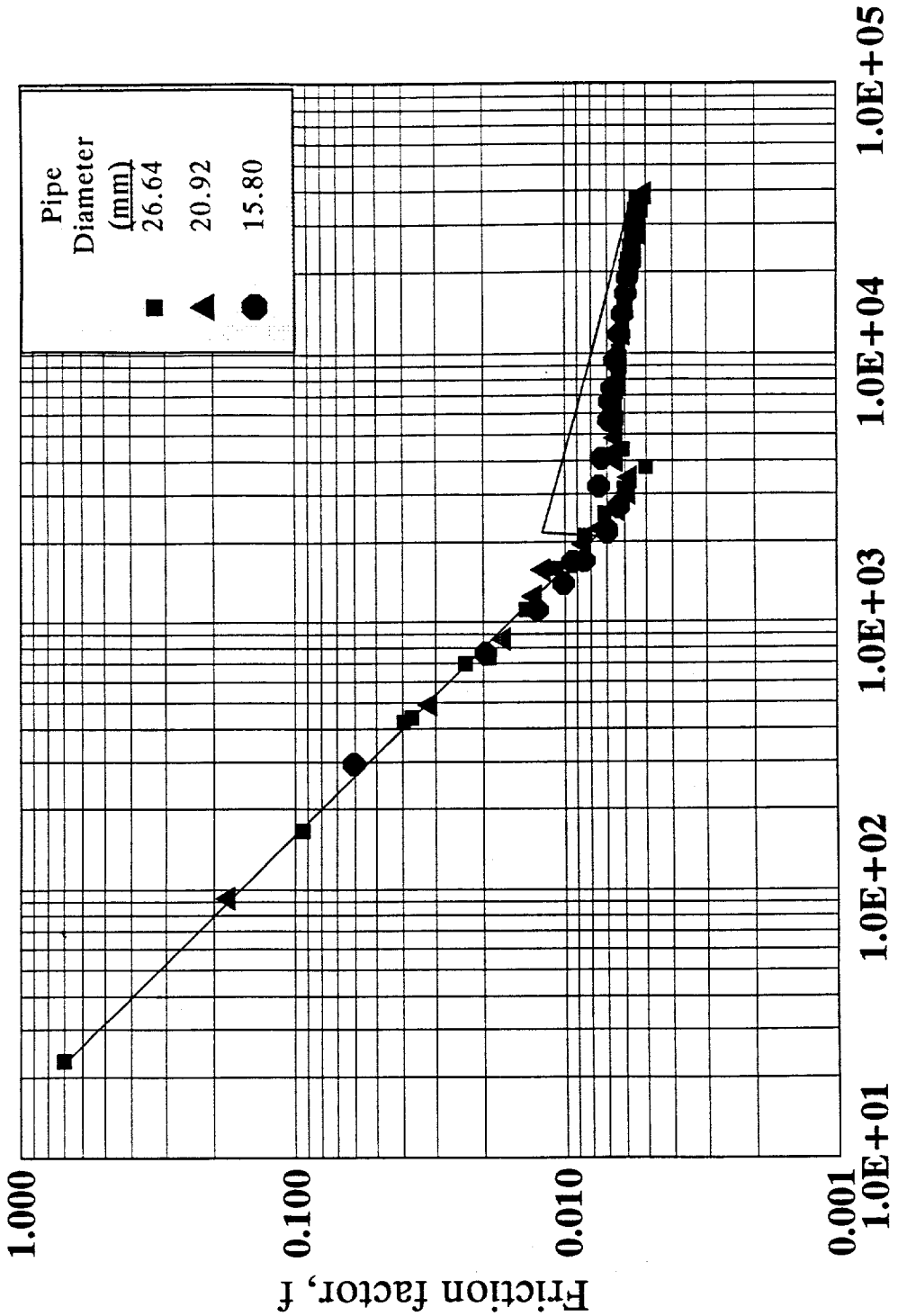

Figure G-8. Friction factor versus Reynolds number for run C-1 (Power Law model).

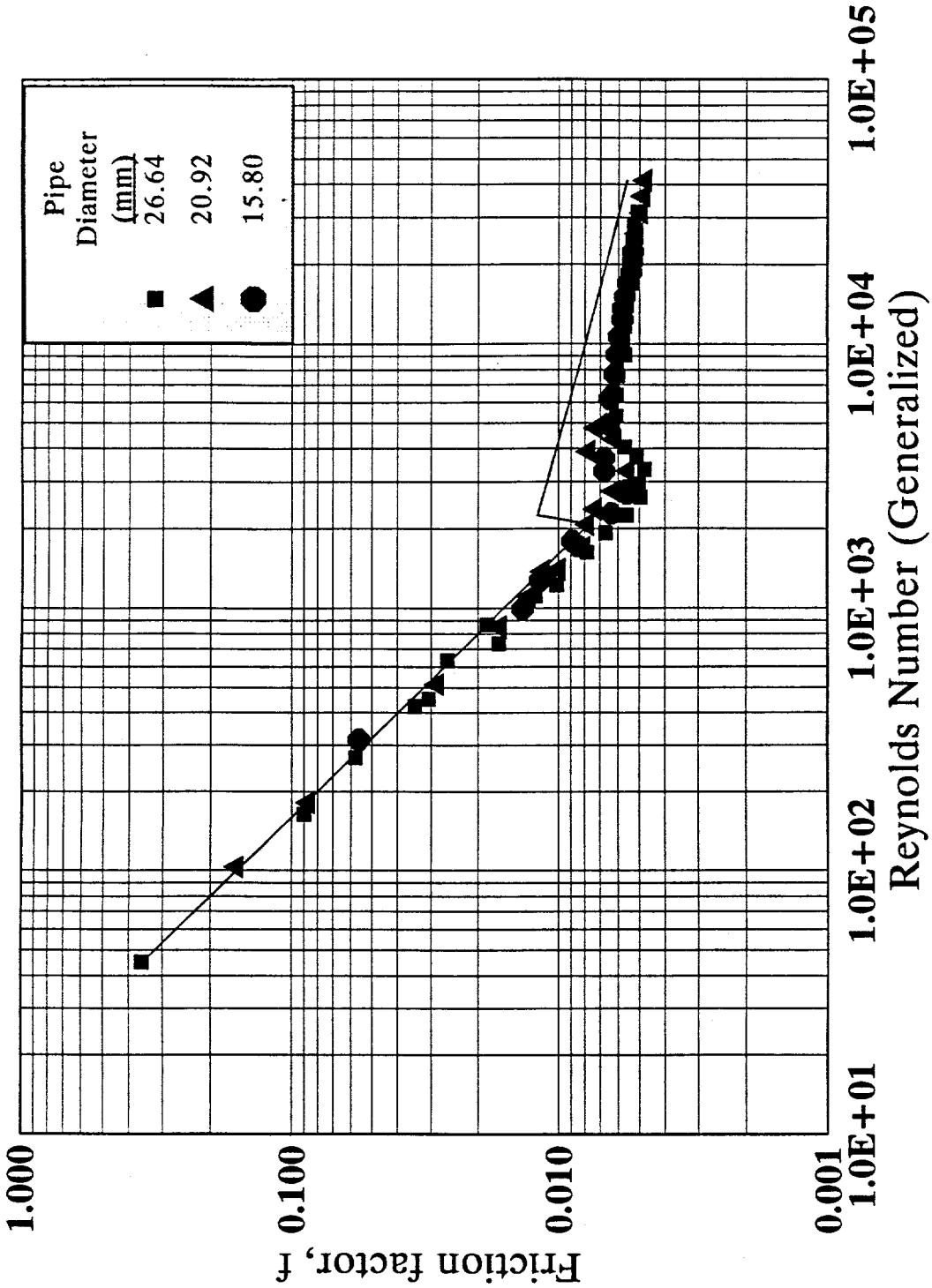

Figure G-9. Friction factor versus Reynolds number for run C-2 (Power Law model).

APPENDIX H

GRAPH OF PARTICLE SIZE VERSUS SOLIDS CONCENTRATION (CUMULATIVE)

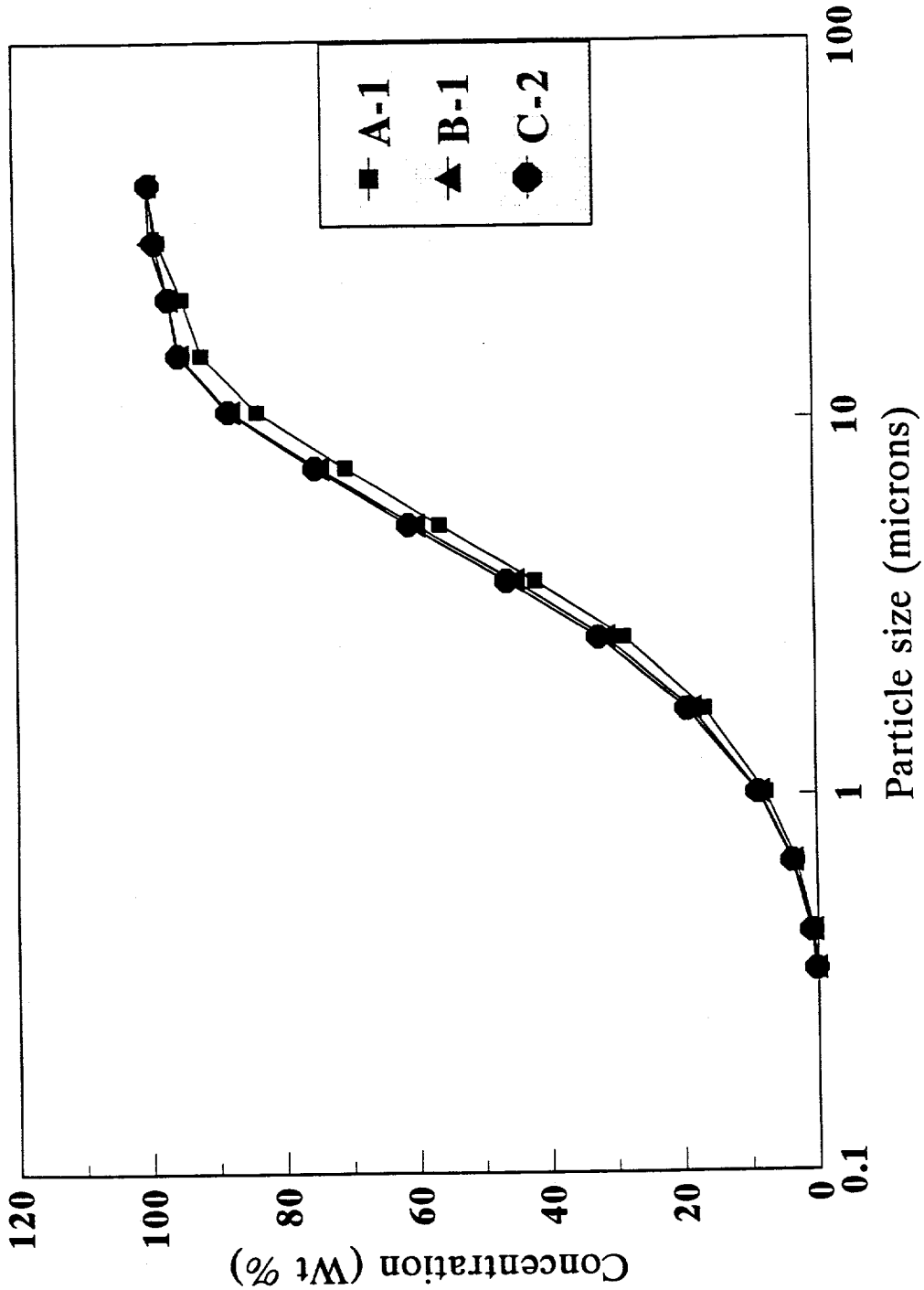

Figure H-1. Particle size versus solids concentration (cumulative).

DISTRIBUTION

1. T. J. Abraham
2. M. R. Ally
3. P. E. Arakawa
4. J. B. Berry
5. M. D. Boring
6. C. H. Brown, Jr.
7. T. B. Conley
8. R. M. Counce
9. A. G. Croff
10-14. R. L. Cummins
15. D. L. Daugherty
16. D. W. DePaoli
17. S. M. DePaoli
18. T. L. Donaldson
19. J. R. Forgy, Jr.
20. V. L. Fowler
21. W. Fulkerson
22. S. B. Garland
23. T. M. Gilliam
24. O. W. Hale
25. J. R. Hightower
26. R. D. Hunt
27-31. T. D. Hylton
32. L. L. Jacobs
33. L. L. Kaiser
34. C. M. Kendrick
35. T. E. Kent
36. A. P. Malinauskas
37. R. C. Mason
38. C. P. McGinnis
39. L. E. McNeese
40. J. W. Moore
41. J. J. Perona
42. J. G. Pruett
43. S. M. Robinson
44. M. K. Savage
45. T. W. Schmidt
46. C. B. Scott
47. J. L. Snyder
48. R. C. Stewart
49. W. T. Thompson
50. D. W. Turner
51. S. D. Van Hoesen
52. M. L. Whitehead
53. C. O. Wiles
54-58. E. L. Youngblood
59. Central Research Library
60. Y-12 Technical Library Document Reference Center
61-62. ORNL Laboratory Records
63. ORNL Laboratory Records - RC
64. ORNL Patent Section

65. Office of Assistant Manager, Energy Research and Development, DOE-ORO, P.O. Box 2008, Oak Ridge, TN 37831-6269
66. George Allen, Sandia National Laboratories, P.O. Box 5800, Dept. 6607, Albuquerque, NM 87185
67. J. A. Bamberger, Pacific Northwest Laboratories, Battelle Boulevard, P.O. Box 999, Richland, WA 99352
68. Sally M. Benson, Earth Sciences Division, Building 50E, Lawrence Berkeley Laboratory, Berkeley, CA 94720
69. James Berger, Office of Technology Integration, Westinghouse Hanford Co., P.O. Box 1970 MS LO-18, Richland, WA 99352
70. Wayne Bliss, Environment, Safety & Health Division, Reynolds Electrical & Engineering Co., P.O. Box 98521, Las Vegas, NV 89193-8521
71. Taz Bramlette, Sandia National Laboratories, P.O. Box 969, Dept. 8240, Livermore, CA 94550

72. Peter Colombo, Brookhaven National Laboratory, Bldg 830, 34 N. Rail Road, P.O. Box 5000, Upton, NY 1197?
73. James Corones, AMES Laboratory, 329 Wilhelm Hall Iowa State University, Ames, IA 50011
74. John Crockett, Oak Ridge Institute for Science and Energy, P.O. Box 117, Oak Ridge, TN 37831
75. Mike Dalmaso, Westinghouse Savannah River Company, Bldg 676-T, Aiken, SC 29808
76. Holmer Dugger, Kaiser Engineers, Hanford Co., Environmental Support Org., P.O. Box 888, MSIN E6-41, Richland, WA 99352
77. Neal S. Egan, Program Development Division, MSE Inc., P.O. Box 3767, Butte, MT 59702
78. M. R. Elmore, Pacific Northwest Laboratories, Battelle Boulevard, P.O. Box 999, Richland, WA 99352
79. Dave Emilia, RUST Geotech., P.O. Box 14000, Grand Junction, CO 81502-2567
80. Bruce Erdal, ET-AET, Los Alamos National Laboratory, MS D446, Los Alamos, NM 87545
81. Roger Gilchrist, Manager, UST-ID, Westinghouse Hanford Company, P.O. Box 1970, MSIN: L5-63, Richland, WA 99352
82. Bimleshwar Gupta, Waste Management Programs, National Renewable Energy Laboratory, 1617 Cole Boulevard, Golden, CO 80401
83. Dr. R. W. Hanks, Slurry Transport Consultant, 495 East 1010 South, Orem, UT 84058
84. Dr. M. G. Hansen, 419 Dougherty Engineering Building, University of Tennessee, Knoxville, TN 37996-2200
85. James E. Helt, Office of Waste Management Programs, 9700 South Cass Avenue, Argonne, IL 60439
86. Dr. H. K. Hepworth, Box 15600, Northern Arizona University, Flagstaff, AZ 86011-1560
87. Ann Cochran Heywood, P.O. Box 808, 7000 East Avenue, MS L-590, Livermore, CA 94550
88. Roger Jacobson, Desert Research Institute, P.O. Box 19040, Las Vegas, NV 89132-0040
89. Dawn Kaback, Colorado Center for Environmental Management, 1536 Cole Blvd, Bldg 4, Suite 180, Golden, CO 80401
90. Ken Koller, Waste Technology Development, EG&G Idaho, Inc., P.O. Box 1625, MS 3930, 2525 Freemont Drive, Idaho Falls, ID 83415-3940
91. Scott Larson, Princeton Plasma Physics Lab, P.O. Box 451, Princeton, NJ 08543
92. Lloyd W. McClure, Westinghouse Idaho Nuclear Co., P.O. Box 4000, Idaho Falls, ID 83415-3402
93. Richard McKay, Battelle Northwest, P.O. Box 999, MSIN P7-19, Richland, WA 99352
94. Katie McWilliam, U.S. Department of Energy, Nevada Operations Office, P.O. Box 98518, Las Vegas, NV 89193-8518
95. Johnny Moore, U.S. Department of Energy, Oak Ridge Operations Office, P.O. Box 2001, Oak Ridge, TN 37831-8620
96. Michael O'Rear, U.S. Department of Energy, Savannah River Operations Office, RFD #1, Bldg. 703A, P.O. Box A, Aiken, SC 29302
97. Jerry L. Peterson, EG&G Rocky Flats, Inc., Technology Development, P.O. Box 464, Golden, CO 80402-0464
98. Paul J. Pettit, FERMCO, P.O. Box 398704 MS-81, Cincinnati, OH 45239-8704

99. Leo Rogers, EG&G Energy Measurements, Inc., P.O. Box 1912, MS RSL-11, Las Vegas, NV 89125
100. Sherri L. Rudolph, U.S. Department of Energy, Rocky Flats Office, DOE Building T124 A, P.O. Box 928, Hwy. 93, Golden, CO 80402-0928
101. Pamela A. Saxman, RDDT&E, U.S. Department of Energy, P.O. Box 5400, Albuquerque, NM 87115
102. Mark Schiffhauer, West Valley Nuclear Services Co., Inc., P.O. Box 191, West Valley, NY 14171-0191.
103. Richard Scott, U.S. Department of Energy, San Francisco Operations Office, 1333 Broadway, Oakland, CA 94612
104. Steven C. Slate, Pacific Northwest Laboratory, MSIN KI-19, P.O. Box 999, Richland, WA 99352
105. Gary E. Staats, U.S. Department of Energy, Pittsburgh Energy Technology Center, P.O. Box 10940, Pittsburgh, PA 15236-0940
106. John Steele, Waste Env. Remediation Programs, Savannah River Site, Building 773-A A208, Aiken, SC 29802
107. Karen Stevenson, U.S. Department of Energy, 376 Hudson Street, New York, NY 10014-3621
108. Ganesan Subbaraman, ETEC, D/030, T038, P.O. Box 1449, Canoga Park, CA 91304
109. Deborah E. Trader, U.S. Department of Energy, Richland Operations Office, P.O. Box 550, Richland, WA 99352
110. Curtis L. Valle, Allied Signal Aerospace, Kansas City Plant, P.O. Box 419159, D/272, FV43, Kansas City, MO 64141-6159
111. Rod Warner, Administrative Building, P.O. Box 398705, Cincinnati, OH 45239-8705
112. Dale Waters, Westinghouse Hanford Company, P.O. Box 1970, MS S4-58, Richland, WA 99352
113. Steve Webster, U.S. Department of Energy, Chicago Operations Office, 9800 South Cass Avenue, Argonne, IL 60439
114. Ted Wheelis, Sandia National Laboratories, Dept. 6623, P.O. Box 5800, Albuquerque, NM 87185
115. Thomas E. Williams, U.S. Department of Energy, Idaho Operations Office, 785 DOE Place, MS-1219, Idaho Falls, ID 83402
116. Charles Zeh, Morgantown Energy Technology Center, 3610 Collins Ferry Road, Morgantown, WV 26507-0880

117-118. Office of Scientific and Technical Information, P.O. Box 62, Oak Ridge, TN 37831